

Direct numerical simulation and two-fluid modeling of multi-phase bubbly flows

By
Souvik Biswas

A dissertation

Submitted to the Faculty

of the

WORCESTER POLYTECHNIC INSTITUTE

in partial fulfillment of the requirements for the

Degree of Doctor of Philosophy

in Mechanical Engineering

March 2007

APPROVED:

Professor Gretar Tryggvason, Chair

Professor David J. Olinger,

Professor Nikolaos A. Gatsonis

Professor Anthony G. Dixon

Professor Michael A. Demetriou, Graduate Committee Representative

ABSTRACT

Results from direct numerical simulations (DNS) of multiphase bubbly flows in vertical and horizontal channels were compared to averaged models of multiphase flows (two-fluid model etc.). The data from the direct numerical simulation were also used to calibrate and improve the averaged models. Steady state laminar flow in a vertical channel was analyzed first. Results from direct numerical simulations are compared with prediction of the steady-state two-fluid model of Antal, Lahey, and Flaherty (1991). The simulations are done assuming a two-dimensional system and the model coefficients are adjusted slightly to match the data for upflow. The model is then tested by comparisons with different values of flow rate and gravity, as well as down flow. Results agree reasonably in the middle of the channel. However, for upflow, model performs poorly near the no-slip wall. To better understand the flow with rising bubbles hugging the no-slip wall, detailed direct numerical simulations of the problem were performed in three dimensions. Deformability of the bubbles was found to play a significant role in the flow structure and averaged flow rate. Finally, the transient buoyancy driven motion of two-dimensional bubbles across a domain bounded by two horizontal walls is studied by. The bubbles are initially released next to the lower wall and as they rise, they disperse. Eventually all the bubbles collect at the top wall. The goal of the study is to examine how a simple one-dimensional model for the averaged void fraction captures the unsteady bubble motion. By using void fraction dependent velocities, where the exact dependency is obtained from simulations of homogeneous bubbly flows, the overall dispersion of the bubbles is predicted. Significant differences remain, however. Results suggest that bubble dispersion by the bubble induced liquid velocity must be included, and by using a simple model for the bubble dispersion improved agreement is found.

ACKNOWLEDGEMENTS

I would like to thank Professor Gretar Tryggvason for advising this research and for constantly providing ideas and support. Special thanks are also due to Professors Ashgar Esmaeeli, Damir Juric, Saeed Mortazavi and Dr. Jiakai Lu for their help on the computations. I would also like to thank Mr. Sia Najafi for his help in carrying out the numerical simulations. I would like to thank my colleagues and friends who have made my stay at the Worcester Polytechnic Institute a pleasant experience: Siju Thomas, Ravi K. Vuta, Lydia Shii, Rahul Terdalkar, Virendra Warke, Jayant Khambekar, Murali Murugavel and Praveen Kulkarni. I have grown a lot as a person from interacting with them.

I am also very much in debt to many excellent teachers whom I was fortunate to have and cannot list here. I am thankful for the financial support of the Department of Energy under grant DE-FG02-03ER46083 and of the Worcester Polytechnic Institute for a teaching assistantship.

TABLE OF CONTENTS

ABSTRACT	ii
ACKNOWLEDGEMENTS	iii
LIST OF FIGURES.....	vii
LIST OF TABLES	xii
CHAPTER I	1
Introduction.....	1
1.1 Motivation.....	1
1.2 Objective and scope of present work	7
CHAPTER II.....	10
Formulation and numerical method	10
2.1 Governing equation.....	10
2.2 Numerical method and front-tracking.....	11
2.3 Convergence tests.....	14
CHAPTER III.....	18
Statistically steady-state motion of bubbles in a vertical two-dimensional channel.....	18
3.1 Introduction	18
3.2 Nearly spherical bubbles: DNS results and two-fluid modeling.....	19
3.2.1 Problem setup.....	19
3.2.2 The two-fluid model.....	20
3.2.3 Results	22
3.3 Effects of deformability	29
3.4 Summary	30

CHAPTER IV	45
Bubbly wall-layers in a vertical channel.....	45
4.1 Introduction.....	45
4.2 Upward bubbly flow near a no-slip wall and averaged equations.	48
4.3 Results.....	50
4.3.1 Effect of void fraction	53
4.3.2 Effect of non-dimensional pressure gradient	54
4.3.3 Effect of Eötvös number	54
4.3.4 Effect of Morton number.....	55
4.3.5 Effect of bubble interactions	56
4.3.6 Comparison with full channel simulation	57
4.4 Summary	57
CHAPTER V.....	76
Transient buoyancy driven motion of bubbles across a two-dimensional domain	76
5.1 Introduction.....	76
5.2 Mono-dispersed bubbles	76
5.2.1 Problem setup.....	76
5.2.2 The two-fluid model.....	77
5.2.3 Results.....	78
5.3 Effect of imposed shear.....	86
5.3.1 Problem setup.....	86
5.3.2 Results.....	86
5.4 Effect of poly-disperse bubbles.....	88
5.5 Summary	90

CHAPTER VI	113
Conclusions	113
6.1 Conclusions	113
6.2 Future Work	114
BIBLIOGRAPHY	116

LIST OF FIGURES

Figure 2.1 The bubbles and the streamlines in a stationary frame of reference are shown at a late time after the flow has reached a statistically steady-state. (a) Intermediate resolution, $n_d=25.6$. (b) Fine resolution, $n_d=51.2$ 16

Figure 2.2 Convergence study for two bubbles with $E_o = 0.5$, $M = 1.25 \times 10^{-5}$, $\alpha = 16.1\%$. Bubbles Reynold's Number is shown vs. time. 16

Figure 3.1 The problem setup. The flow is fully developed and at steady-state. The width of the channel is H , the average velocity in the absence of bubbles is U , gravity acts in the negative y direction and the pressure gradient is selected to generate either up or down flow. 32

Figure 3.2 Two simulations of the rise of bubbles in upflow in a vertical channel (left frame) and downflow (right frame). The bubbles and the streamlines in a stationary frame of reference are shown at a late time after the flow has reached a statistically steady-state. 33

Figure 3.3 Two simulations of the rise of bubbles in upflow in a vertical channel (left frame) and downflow (right frame). The bubbles and the vorticity contours in a stationary frame of reference are shown at a late time after the flow has reached a statistically steady-state. 34

Figure 3.4 Two simulations of the rise of bubbles in upflow in a vertical channel (left frame) and downflow (right frame). The bubbles and the velocity field in a stationary frame of reference are shown at a late time after the flow has reached a statistically steady-state. 35

Figure 3.5 Two simulations of the rise of bubbles in upflow in a vertical channel (left frame) and downflow (right frame). The path of the bubbles are shown after the flow has reached a statistically steady-state. 36

Figure 3.6 The average bubble rise Reynolds number (a), the through flow normalized by the channel flow without bubbles (b) and the root-mean-squared distance of the bubbles from the centerline of the channel, normalized by half the channel width (c). 37

Figure 3.7 The averaged void fraction profile from the simulations and as predicted by the two fluid model, using the original values for the model coefficients. Results for upflow are shown on the left and for down flow on the right. 38

Figure 3.8 The averaged velocity profile from the simulations and as predicted by the two fluid model, using the original values for the model coefficients. Results for upflow are shown on the left and for down flow on the right. 38

Figure 3.9 The effect of adjusting the model coefficients for the upflow case. The result from the full simulations, along with three profiles obtained by the two-fluid model are shown. The averaged fluid Reynolds number is on the left and the void fraction is on the right. The values of the leading numerical coefficient in equation (3.5) are 24, 18.3, 18.3 and the lift coefficient is 0.05, 0.10, 0.14, for the three different model profile shown.....	39
Figure 3.10 Total flow rate for different values of gravity as predicted by the full simulations and a two-fluid model with two sets of model parameters.....	40
Figure 3.11 Total flow rate for different values of the void fraction, changed by changing the number of bubbles, as predicted by the full simulations and a two-fluid model with two sets of model parameters.....	40
Figure 3.12 Total flow rate for different bubbles sizes, but the same void fraction as predicted by the full simulations and a two-fluid model with two sets of model parameters.....	41
Figure 3.13 A simulation of the rise of deformable bubbles in upflow in a vertical channel. The bubbles are shown with the streamlines (left), vorticity contours (middle), and velocity field (right) in a stationary frame of reference are shown at a late time after the flow has reached a statistically steady-state.....	42
Figure 3.14 Paths of the rise of deformable bubbles in upflow in a vertical channel is shown at a late time after the flow has reached a statistically steady-state.....	43
Figure 3.15 The averaged (a) void fraction and (b) velocity profile from the simulations for non-deformable and deformable bubbles.....	44
Figure 4.1. (a)The problem setup. Rise of a single bubble near the wall. The width of the channel is $2D$, where D is the bubble diameter. Gravity acts in the negative z direction and the pressure gradient is acts in the positive z direction. The wall is no slip at $x=0$ and full slip at $x=2D$. In the region $x > D$ a body force is added to make the flow hydrostatically balanced. (b) Averaging volume for average equations.....	61
Figure 4.2. Three-dimensional direct simulation of the rise of a single bubble in upflow near the no-slip wall in a vertical channel. The bubble and the iso-contours of vertical velocity in a x - z plane are in a stationary frame of reference at a late time after the flow has reached a steady state.....	62
Figure 4.3. Three-dimensional direct numerical simulation of the rise of a single bubble in upflow in a vertical channel. Path of the bubble is shown in a stationary frame of reference.....	63
Figure 4.4 (a) The average velocity of bubbles and (b) the through flow normalized by the channel flow without bubbles.....	64

Figure 4.5. Results of the convergence study. The average velocity of bubbles. The density and viscosity ratio is chosen as 1/10 in this case.	65
Figure 4.6. The distribution of the Reynolds stresses in x direction.	65
Figure 4.7. Local surface tension force along x direction.	66
Figure 4.8. Comparison between liquid velocity profile in the wall layer obtained by two fluid model and direct numerical simulation.	66
Figure 4.9. Effect of changing the void fraction (α) on the (a) shape of the bubble, (b) local surface tension force, (c) slip Reynolds number.	67
Figure 4.10. Effect of changing the pressure gradient ($\frac{\beta}{\rho g}$) on the (a) shape of the bubble, (b) local surface tension force, (c) slip Reynolds number.	68
Figure 4.11. Effect of changing the Eötvös No. (Eo) on the (a) shape of the bubble, (b) local surface tension force, (c) slip Reynolds number.	69
Figure 4.12. Effect of changing the Morton No. (M) on the (a) shape of the bubble, (b) local surface tension force, (c) slip Reynolds number.	70
Figure 4.13. Three-dimensional direct simulation of the rise of (a) 4 bubbles and (b) 16 bubbles in upflow near the no-slip wall in a vertical channel. The bubbles and the iso-contours of the vertical velocity in a plane are shown in a stationary frame of reference at a late time after the flow has reached a steady state.	71
Figure 4.14. Three-dimensional direct simulation of the rise of (a) four bubbles and (b) sixteen bubbles in upflow in a vertical channel. Path of the bubbles are shown in a stationary frame of reference at a late time after the flow has reached a steady state.	72
Figure 4.15. Comparison between Single, Four, Sixteen bubble Simulations (a) The average velocity of bubbles and (b) the through flow normalized by the channel flow without bubbles.	73
Figure 4.16. Effect of number of bubbles on the slip velocity.	74
Figure 4.17. Comparison of liquid velocity profile in the wall layer with full wall simulation of J. Lu, S. Biswas, and G. Tryggvason. The simulation in wall layer is done unto two bubble diameters only.	74
Figure 5.1. The problem setup. The horizontal channel is bounded by walls in the y-direction and is periodic in the x-direction. The height of the channel is H and gravity acts in the negative y direction. The bubbles are released from near the bottom of the channel and rises upwards until they hit the top wall.	92

Figure 5.2. The steady-state slip Reynolds number for bubbles in homogeneous flow versus the void fraction. The results are obtained by numerical simulations of the motion of 25 bubbles in a fully periodic domain. One frame, showing the bubble distribution at one time is inserted. 93

Figure 5.3. Simulations of the rise of bubbles in a horizontal channel. The bubbles and the streamlines in a stationary frame of reference are shown at four different times, starting with the initial conditions. In the last frame, some of the bubbles have hit the top wall..... 94

Figure 5.4. Simulations of the rise of bubbles in a horizontal channel. The bubbles and the vorticity contours in a stationary frame of reference are shown at four different times, starting with the initial conditions. In the last frame, some of the bubbles have hit the top wall..... 95

Figure 5.5. Simulations of the rise of bubbles in a horizontal channel. The bubbles and the velocity field in a stationary frame of reference are shown at four different times, starting with the initial conditions. In the last frame, some of the bubbles have hit the top wall..... 96

Figure 5.6. (a)The average bubble rise Reynolds number versus time for five different initial conditions. Initially the bubble velocity increases as the bubbles spread out and the void fraction decreases. After about time 4, some of the bubbles have hit the top wall and the average velocity decreases. (b) Path of the bubbles for a single case. 97

Figure 5.7. The averaged void fraction profile at four different times. The solid line is the simulation results, averaged over five cases. The dashed line is the prediction of the two-fluid model..... 98

Figure 5.8. (a) The average turbulent kinetic energy profile for one case, shown at seven times. (b) The void fraction and the turbulent kinetic energy versus y at $t/\tau=3.0$ 99

Figure 5.9. The correlation coefficient (as defined in the text) between the turbulent kinetic energy and the void fraction versus time, for one case. 100

Figure 5.10. The mean turbulent kinetic energy for one case versus time..... 100

Figure 5.11. (a) The dissipation and the turbulent kinetic energy versus y at $t/\tau=3.0$. (b)The correlation coefficient (as defined in the text) between the dissipation and the turbulent kinetic energy for one case. 101

Figure 5.12. The averaged void fraction profile from the simulations and as predicted by the two fluid model at different times. Here $C=2.0$ (see Equation 5.6). 102

Figure 5.13. The effect of the dispersion coefficient on the predicted void fraction profile at time $t/\tau=4.0$. The average profile from the simulations is also plotted. 103

Figure 5.15. Simulations of the rise of bubbles in a horizontal channel. The bubbles and the streamlines in a stationary frame of reference are shown at a single time ($t/\tau=3.0$). (a) Streamlines are computed from total velocity. (b) Streamlines are computed from perturbation velocity. 105

Figure 5.16. (a) The void fraction distribution for different shear rates versus y at $t/\tau=3.0$. (b)The correlation coefficient (as defined in the text) between the void fraction distributions with no shear and with shear. 106

Figure 5.17. (a) The turbulent kinetic energy distribution for different shear rates versus y at $t/\tau=3.0$. (b)The correlation coefficient (as defined in the text) between the turbulent kinetic energy distributions with no shear and with shear. 107

Figure 5.18. (a) The dissipation distribution for different shear rates versus y at $t/\tau=3.0$. (b)The correlation coefficient (as defined in the text) between the dissipation distributions with no shear and with shear. 108

Figure 5.19. Simulations of the rise of poly-dispersed bubbles in a horizontal channel. The bubbles and the streamlines in a stationary frame of reference are shown at four different times, starting with the initial conditions. In the last frame, most of the larger bubbles have hit the top wall. 109

Figure 5.20. The average slip velocity for different bubble sizes with time. The large bubbles ($d=0.16$) rise faster than other bubbles until they start hitting the top wall and slow down. 110

Figure 5.21. % number density of similar sized bubbles are shown at four different times. The data is plotted at 8 equally spaced bins along the vertical direction. 111

LIST OF TABLES

Table 2.1. Convergence study for one bubble in a regular array in a two-dimensional square domain with resolution $n_x = n_y$ and n_d grid points per bubble diameter: steady state drift Reynolds number of the bubble Re_d	17
Table 4.1. Parameters for baseline case and convergence study.....	75
Table 5.2. Parameters for migration poly-disperse bubbles.....	112

CHAPTER I

Introduction

1.1 Motivation

Bubbly liquids are found in an extraordinary number of natural and industrial processes. Natural occurrences of such flows can be found in explosive volcanic eruptions and the mass transfer between the oceans and the atmosphere. Such flows are also found in industrial processes like boiling heat transfer, cloud cavitation in hydraulic systems, aeration in water purification, bubble columns and centrifuges in the petrochemical industry, cooling devices in nuclear industry, scavenging of dissolved gases in separation processes suspensions of cells in bioreactors. The need to understand the behavior of such systems has therefore motivated a number of studies.

Traditionally engineering predictions of bubbly flows were based on correlations of the bulk properties like mean pressure drop, mean flow rate, mean wall shear stress etc. These correlations were obtained from simple scaling arguments and experimental measurements (Hetsroni, 1982). While knowledge of such mean parameters are enough for simple pipe flows, a more detailed knowledge of the flow field is needed for designing more sophisticated devices e.g. bubble columns, centrifuges etc.

To predict this kind of detailed flow fields, flow equations that describe the average behavior of multiphase systems are often numerically solved. These equations can take several forms. The simplest assumption is that the multiphase flow is a mixture whose properties depend on the void fraction. In the mixture approximation there is a single average velocity, but in most cases the bubbles and the liquid move with different

velocities and the behavior of the flow depends strongly on the slip velocity between the bubbles and the liquid. Today it is therefore most common to work with “two-fluid models” where separate mass and momentum (and energy where appropriate) equations are written for the different fluids. The liquid motion is almost always computed by continuum equations resembling the Navier-Stokes equations but containing additional terms accounting for the presence of the bubbly phase. The equations for the averaged motion of the liquid contain extra terms that represent the effect of the bubbles. One is the force that the bubbles exert on the liquid. Another is the velocity fluctuations generated by the motion of the bubbles. Non-uniform bubble motion can also lead to buoyancy driven currents and in turbulent bubbly flow the bubbles can modify the turbulence and thus the evolution of the flow. The motion of the bubbles can be computed by a similar continuum equation. These effects also give rise to additional terms in the liquid continuum equation. Antal, Lahey and Flaherty (1991) and Azpitarte and Buscaglia (2003) developed a two fluid model for laminar flow in a vertical channel. Later, Lopez De Bertodano, Lahey, and Jones (1987, 1994), Kuo, Pan, and Chieng (1997), Guet, Ooms and Oliemans (2005), Politano, Carrica, and Converti (2003) and Celik and Gel (2004) extended this approach to model turbulent regimes. The main difficulty of using such models is the constitutive relations used for representing the force exerted on the bubble is limited by the parameter range of the flow and is rarely universal. Additionally, there is very limited understanding of bubble-bubble interactions and the effect of the bubbles on the liquid (two-way coupling). Hence such approaches are currently limited to flows with very low void fraction and very small particles, where it is possible to ignore the effect of the bubbles on the liquid (one-way coupling).

Experimental investigations of multiphase flow are traditionally limited to measurements of either local or time averaged quantities. Notable investigations of bubbly flows include Serizawa, Kataoka and Michiyoshi (1975), Wang, Lee, Jones and Lahey (1987), Liu and Bankoff (1993), Nakoryakov and Kashinsky (1981, 1996), Liu (1997), Kashinsky, Randin, and Timkin (1999), Song, Luo, Yang, and Wang (2001) So, Morikita, Takagi, and Matsumoto, (2002), Luo, Pan, and Yang (2003), Guet, Ooms and Oliemans (2005), and Mudde and Saito (2005), and Matos, Rosa and Franca (2004). Unsteady flow-field measurements of fully three-dimensional multi-phase flow are much more recent (Schlüter and Rabiger, 1998, Brucker, 1996 and Stewart, 1995) and are made possible due to advent of advanced methods like particle image velocimetry (PIV). While these methods are promising they are also limited to low void fraction cases.

As in turbulent flow of a single-phase fluid, multiphase flows generally possess a large range of scales, ranging from the sub-millimeter size of a small bubble or an eddy to the size of the system under investigation. For an industrial bubble column or the flow around a ship, the ratio of the smallest to the largest scale is easily tens or hundreds of thousands. Assume, somewhat arbitrarily, that grid points of the order of ten are needed per smallest scale, that the smallest bubble or eddy is about a millimeter, and the dimensions of the system which needed to be simulated are measured in meters. For this relatively modest system over 10^{12} grid points would be needed. While direct numerical simulations (where all flow scales are resolved) of such systems is likely to be possible within ten to twenty years, particularly if adaptive gridding can be used to reduce the actual number of grid points used, it is unlikely that it will be practical to use such huge simulations for routine engineering predictions. Furthermore, it is likely that this will not

be necessary, except in a few special cases. Thus, it is likely that models of multiphase flows, where the average motion is computed, but the influence of small, unresolved scales is accounted for by closure models, will be in use for the foreseeable future. Providing accurate closure models will therefore continue to be at the center of multiphase flow research.

Still, direct numerical simulations (DNS) of disperse bubbly multiphase flows, where every continuum length and time scale is fully resolved, can satisfy two main objectives. First, such simulations can generate insight and understanding of the basic behavior of the flow at the smallest scales. These include the forces on the bubbles, how the bubbles affect the flow, and how many bubbles interact in dense disperse flows. Secondly, the vast data generated by direct numerical simulations can be used in the construction of closure models for engineering simulations of the averaged flow field. This is due to the fact, that, multiphase flows, like single-phase turbulent flows, exhibit a great deal of universality at the smallest scales and it is almost certain that re-computing small-scale behavior that is already understood is not necessary.

During the last two decades, great advances have been made in direct numerical simulations of multiphase flow. Ryskin and Leal (1984) simulated steady-state shape of a single clean axisymmetric bubble. Jan (1994) and McLaughlin (1996) extended it to bubbles with surfactants. Takagi and Matsumoto (1994), Miyata (1994), and Oka and Ishii (1999) performed unsteady three-dimensional simulations of the motion of a deformable bubble. At present, for fluid particles, like bubbles and drops, it is customary to use a one field formulation, where a single Navier-Stokes equation is solved in the entire flow field on a fixed grid. The interface between the fluids is either tracked (front

tracking method, Unverdi and Tryggvason, 1991) or recaptured (volume of fluid method, Lafaurie et al. 1994 and level set method, Sussman and Smereka, 1997).

Studies on the simulation of multiple bubbles were far more difficult because of increased computational complexity. Initially, some progress was achieved by the use of simplified assumptions. Moore (1965) observed that except in boundary layer and wake the flow around a bubble is inviscid in high Reynolds number regimes. Using this Smereka (1993), Sangani and Didwania (1993), and Yurkovetsky and Brady (1996) developed methods for simulating the motion of large numbers of spherical bubbles in the inviscid limit for low void fraction cases. Results from these simulations show that velocity of bubbles become equal over time and form horizontal rafts, a discrepancy with experimental results. This lack of agreement with experimental results is later attributed to the absence of wakes in the simulations, which led researchers to question its appropriateness. Another popular method is to represent the bubbles as point particles and assume that the bubbles are smaller than the smallest eddies of the continuous phase. Then the bubbles can be advected using Newton's second law if constitutive models of all the forces acting on the bubbles are available (Spelt and Biesheuvel 1997). Although all scales of motion in the liquid are resolved in this approach, it suffers from a number of shortcomings too. The relations prescribed for the forces exerted by the liquid on the bubbles are only applicable in a limited region of the parameter space. In addition, direct bubble/bubble interactions are not accounted for, so that the simulations are restricted to low void fractions.

Direct numerical simulations (DNS) of multiple bubbles were not attempted until very recently when the increase in computing power made such studies possible. Esmaeeli and

Tryggvason (1996) performed two-dimensional simulations of homogeneous bubbly flows in periodic cells using up to 324 bubbles and found that the work done by the bubbles increases the energy of much larger flow structures. This result is similar to what has been found for forced two-dimensional turbulence. Esmaeeli and Tryggvason (1998, 1999) followed the motion of multiple bubbles in periodic cells in two and three dimensions. They have found, for both two and three-dimensions, that the regular structure of the bubble breaks up as they evolve. For low Reynolds number the rise velocity of freely evolving array is higher than regular array. For moderate Reynolds number the effect is opposite and rise velocity of regular array is higher than freely evolving array. Velocity fluctuations were found to be larger in the two-dimensional simulations than three-dimensional cases. Pair formation of three-dimensional bubbles was also observed at high Reynolds number. Bunner and Tryggvason (2002) simulated motion of up to 216 three-dimensional bubbles by direct numerical simulation. They have found two bubbles that are aligned vertically attract each other due to the wake effect, rotate around each other, and then repel when they are aligned horizontally. This mechanism is famously named as ‘drafting, kissing and tumbling’. At higher void fraction periodic formation of horizontal rafts of bubbles is also observed. The velocity fluctuation of the bubbles and liquid is found to be anisotropic with vertical fluctuation velocities of both the bubbles and the liquid being larger than the horizontal fluctuation velocities. Bunner and Tryggvason (2003) followed the motion of 27 deformable bubbles with Reynolds number close to 25. Results show, that the bubbles eventually form vertical streams and accelerate. Esmaeeli and Tryggvason (2005) studied rise of 3-dimensional buoyant bubbles at $O(100)$ Reynolds number. They found flow with deformable bubbles is more dissipative than the flow with spherical bubbles at

comparable Reynolds number. They also found absence of any streaming instability found by Bunner and Tryggvason (2003) at this Reynolds number.

1.2 Objective and scope of present work

As discussed, in the previous section, great advances have recently been made in direct numerical simulation of homogeneous bubbly multiphase flows. In the last five years a lot of studies have been made in simulating large number of bubbles in both two and three dimensions. But few studies have been done to investigate more complex practical multiphase flows using direct numerical simulation. In most practical multiphase flows presence of wall boundaries are likely. However, interactions of bubbles with no-slip walls are not completely understood yet. Present models (Antal et. al. 1991) of wall-bubble interactions are heavily sensitive on model coefficients which in turn are significantly dependent on bubble size and other physical parameters governing the flow. A more complete understanding of the interactions between bubbles and wall requires a description of detailed flow structure around the bubbles near the wall. This is also an prerequisite for improving the current wall models for engineering simulations of the averaged flow field. The present study tries to address these problems by using direct numerical simulations to solve the complete flow field around the bubbles near the wall. Another important aspect that is not addressed in past studies pertains to the universality of small scale behavior of bubbly flows. For example, does the small scale behavior that is observed in simulations of homogenous bubbly flows applies to more complex transient flows? The present study tries to address this question by developing an averaged model of transient migration of bubbles in a horizontal channel based on small scale behavior observed in homogenous simulations. Comparison between this model and

actual simulation results can help in addressing this important question. In Chapter 3 the results from direct numerical simulations of laminar bubbly flow in a vertical channel are compared with prediction of the steady-state two-fluid model of Antal, Lahey, and Flaherty (1991). The simulations are done assuming a two-dimensional system and the model coefficients are adjusted slightly to match the data for upflow. The model is then tested by comparisons with different values of flow rate and gravity, as well as down flow. In all cases the results agree reasonably well, even though the simulated void fraction is considerably higher than what is assumed in the derivation of the model. The results do, however, suggest a need to understand the lift and the wall repulsion force on bubbles better, particularly in dense flows. In Chapter 4 a model problem where the bubbles near a no-slip wall rise is studied. A parametric study on the velocity increase across the layer is also performed. The study is done using direct numerical simulations where the flow around the bubbles is fully resolved and the uniform flow outside the wall layer is generated by a properly adjusted body force. The behavior of the flow is studied for a range of parameters using a regular periodic array and the results then compared with results from simulations of freely evolving and interacting bubbles for one case, as well as with results of simulations of the full channel. The average properties of the flow in the wall layer are examined and compared with a simple drift-flux model. In Chapter 5, transient buoyancy driven motion of two-dimensional bubbles across a domain bounded by two horizontal walls is studied by direct numerical simulations. The bubbles are initially released next to the lower wall and as they rise, they disperse. Eventually all the bubbles collect at the top wall. The goal of the study is to examine how a simple one-dimensional model for the averaged void fraction captures the unsteady bubble motion. Significant differences remain, however. It is suggested that bubble dispersion must be

included, and by using a simple model that relates the bubble dispersion to the bubble induced liquid velocity improved agreement is shown.

CHAPTER II

Formulation and numerical method

Main challenges of simulating interfaces between different fluids are to maintain a sharp front and to compute the surface tension accurately. The front tracking method was originally developed by Unverdi & Tryggvason (1992) and improved by Esmaeeli & Tryggvason (1998) allows us to achieve this objective. The main features of the method are presented briefly; a complete description is available in Tryggvason et al. (2001). One set of equations is used for the whole domain, including both the bubbles and the carrying liquid on a two/three-dimensional fixed grid. In addition to the two/three-dimensional fixed grid on which the Navier-Stokes equation is solved, a moving, deformable, two-dimensional mesh is used to track the boundary between the bubble and the ambient fluid. This mesh consists of marker points connected by linear elements for two-dimensional cases and triangular elements for three-dimensional cases. This mesh is eventually used to update the density and viscosity at each grid point and to find the surface tension. The code originally developed by Esmaeeli & Tryggvason (1998) is used in this study after some slight modifications.

2.1 Governing equation

The fluid motion is assumed to be governed by the Navier-Stokes equation:

$$\frac{\partial \rho \mathbf{u}}{\partial t} + \nabla \cdot \rho \mathbf{u} \mathbf{u} = -\nabla P + \rho \mathbf{f} + \nabla \cdot \mu (\nabla \mathbf{u} + \nabla^T \mathbf{u}) + \int \sigma \kappa' \mathbf{n}' \delta^\beta (\mathbf{x} - \mathbf{x}') ds' \quad (2.1)$$

This equation is valid for the whole flow field but the density field and viscosity field change discontinuously at the interface of two fluids. Here \mathbf{u} is the velocity, P is the pressure and \mathbf{f} is a body force. Surface tension term is added at the interface. The term

δ^β is a two or three dimensional delta function constructed by repeated multiplication of one dimensional delta functions. σ is the coefficient of surface tension, κ' is the curvature for two dimensional flow and twice the mean curvature for three dimensional flow. \mathbf{n}' is the unit vector normal to the front.

The mass conservation equation is given by

$$\frac{\partial \rho}{\partial t} + \nabla \cdot \rho \mathbf{u} = 0 \quad (2.2)$$

In all our cases the fluids are taken to be incompressible and viscosity of each fluid is constant i.e.,

$$\frac{D\rho}{Dt} = 0, \quad \frac{D\mu}{Dt} = 0 \quad (2.3)$$

Combining equation 2.2 and 2.3,

$$\nabla \cdot \mathbf{u} = 0 \quad (2.4)$$

2.2 Numerical method and front-tracking

The main challenge of multiphase flow, using one fluid formulation is, to maintain a sharp front during advection of density and viscosity and to compute the surface tension accurately. In the front-tracking method, besides the fixed grid, where, velocity and pressure fields are computed, there is another grid which is used to represent the interface between two fluids. This is a unstructured grid and the main purpose of it is to sharply demarcate the interface between two fluids. This helps in maintaining a sharp front during advection of density and viscosity and to compute the surface tension. Hereafter, this grid is referred as the front grid. In this study, instead of advecting the density directly, an indicator function (I) is advected. The value of the indicator function is always assumed to be 0 inside the liquid and 1 inside the bubbles. The advection of the indicator function on the fixed grid between time steps n and $n + 1$ is accomplished by

first moving the front grid and then constructing a grid-indicator function field to match the location of the front. The velocity of each front marker point is interpolated from the fluid velocities at the four grid nodes surrounding the front point in each direction using the same weighting functions proposed by Peskin (1977). After all points have been advected, a discrete version of the indicator function gradient across each front element, written symbolically as, $\nabla_h I = \int \delta_h \mathbf{n} dA'$ is calculated on the front and distributed onto the grid. δ_h is a discrete delta function and is defined on 4^3 grid points with the same weighting functions suggested by Peskin. A smooth indicator function field is then obtained by solving the following Poisson equation.

$$\nabla_h^2 I = \nabla_h \cdot \nabla_h I \quad (2.5)$$

The density and viscosity field is then calculated as following,

$$\rho = (\rho_g - \rho_l)I, \quad \mu = (\mu_g - \mu_l)I \quad (2.6)$$

where $\rho_g, \rho_l, \mu_g, \mu_l$ are density of bubbles, density of liquid, viscosity of bubbles and viscosity of liquid respectively.

An accurate computation of the surface tension force in a conservative way is also very important for the accuracy of the simulation. Otherwise an artificial force is introduced in the simulation and the results are no longer valid.

In two-dimension the surface tension term on a front element can be written as,

$$\delta \mathbf{F}_\sigma = \int_{\Delta s} \sigma \kappa' \mathbf{n}' ds = \int_{\Delta s} \frac{\partial(\sigma \mathbf{s})}{\partial s} ds = (\sigma \mathbf{s})_2 - (\sigma \mathbf{s})_1 \quad (2.7)$$

This ensures the net force on any closed interface is zero. Here, \mathbf{s} is the tangent vector at the end points of the front element

In three-dimension the surface tension term on a front element is calculated as,

$$\delta \mathbf{F}_\sigma = \int_{\Delta s} \sigma \kappa \mathbf{n} ds = \int_{\Delta s} \sigma (\mathbf{n} \times \nabla) \times \mathbf{n} ds = \int_{\Delta s} \sigma \mathbf{t} \times \mathbf{n} ds \quad (2.8)$$

In both two and three dimensions, the tangents are calculated by fitting a polynomial curve through the points of the front element and neighboring elements.

Once the density field, viscosity field and surface tension term is computed; standard methods (pressure projection method in this case) of integrating Navier-Stokes equation in time can be used. In most of our studies a second order in time scheme is used, but here a first order scheme is described.

Equation 2.1 and 2.2 are discretized in a fixed staggered grid in the following way

$$\frac{\rho^{n+1} \mathbf{u}^{n+1} - \rho^n \mathbf{u}^n}{\Delta t} = \mathbf{A}^n - \nabla P \quad (2.9)$$

$$\nabla \cdot \mathbf{u}^{n+1} = 0 \quad (2.10)$$

where \mathbf{A} is the advective, diffusive and force terms in equation 2.1. Further equation 2.9 can be written as,

$$\frac{\rho^{n+1} \mathbf{u}^* - \rho^n \mathbf{u}^n}{\Delta t} = \mathbf{A}^n \quad (2.11)$$

$$\frac{\rho^{n+1} \mathbf{u}^{n+1} - \rho^{n+1} \mathbf{u}^*}{\Delta t} = -\nabla P \quad (2.12)$$

Next by taking the divergence of equation 2.12 and using 2.10, an elliptic equation for pressure is obtained

$$\nabla \cdot \frac{1}{\rho^{n+1}} \nabla P = -\frac{\nabla \cdot \mathbf{u}^*}{\Delta t} \quad (2.13)$$

This non-separable elliptic equation is solved using the multigrid package, MUDPACK, developed by John Adams (1989). The final velocity is then calculated as,

$$\mathbf{u}^{n+1} = \mathbf{u}^* - \frac{\Delta t}{\rho^{n+1}} \nabla P \quad (2.14)$$

2.3 Convergence tests

A number of validation tests of the above method are reported in Tryggvason et al. (1998), Esmaeeli & Tryggvason (1998). For example, Jan (1994) implemented the method in axisymmetric coordinates and compared the results for the rise of a single bubble at $Re = 20$ and $We = 12$ with those of Ryskin & Leal (1984). Using a large domain and about 25 grid points per bubble radius, Jan (1994) found that the difference in the steady-state rise velocities was less than 1%, and that the bubble shape, streamlines, and recirculation behind the bubble were almost identical. In this study the goal is to study the motion and interaction of bubbles in vertical and horizontal channels with no-slip walls. It is therefore important to study the convergence of the method in such cases. However, the high cost of DNS computations imposes a constraint on the resolution that can be used for a large simulation. Therefore it is customary to establish the validity of the method by performing the convergence study on a similar but smaller model problem

In this study, a grid independence study was conducted in a two dimensional vertical channel with two bubbles and a pressure gradient and gravity acting downwards. The rise of the bubbles was simulated at $Eo = 0.5$, $M = 1.25 \times 10^{-5}$ and void fraction of 16.1%. Three different resolutions were used for the study, with about 12.8, 25.6, and 51.2 points per diameter. Figure 2.2 shows the bubble Reynolds number of the bubbles with time. The results from table 2.1 shows that the relative error between the intermediate and fine resolution is at most 2% for the steady state drift Reynolds number of the bubble, Re_b . The results from figure 2.2 and table 2.1 show that for a resolution of about 25 points per bubble diameter the solution is almost grid independent. Resolutions between 20 and 27

grid points per bubble diameter were used in the present simulations, depending on the size of the simulation.

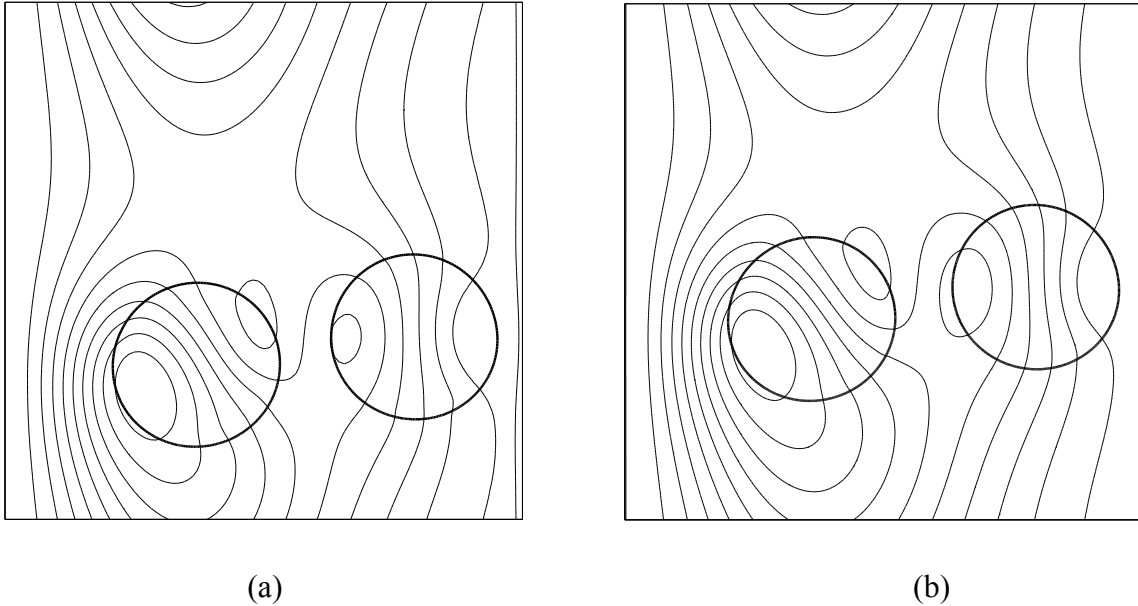


Figure 2.1 The bubbles and the streamlines in a stationary frame of reference are shown at a late time after the flow has reached a statistically steady-state. (a) Intermediate resolution, $n_d=25.6$. (b) Fine resolution, $n_d=51.2$.

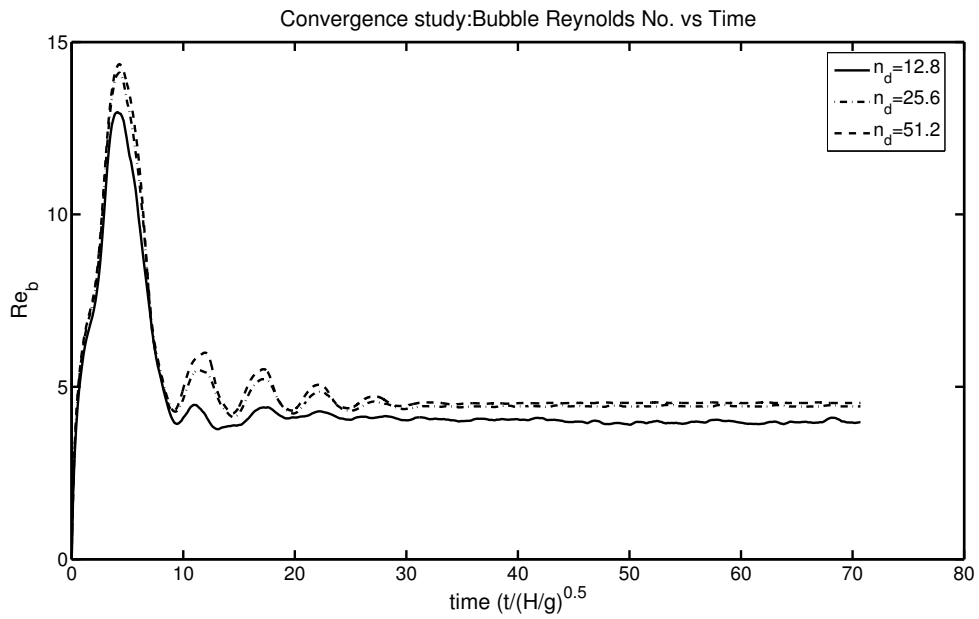


Figure 2.2 Convergence study for two bubbles with $Eo = 0.5$, $M = 1.25 \times 10^{-5}$, $\alpha = 16.1\%$. Bubbles Reynolds' Number is shown vs. time.

Table 2.1. Convergence study for one bubble in a regular array in a two-dimensional square domain with resolution $n_x = n_y$ and n_d grid points per bubble diameter: steady state drift Reynolds number of the bubble Re_d .

$n_x=n_y$	n_d	Re_d
40	12.8	3.99
80	25.6	4.44
160	51.2	4.53

CHAPTER III

Statistically steady-state motion of bubbles in a vertical two-dimensional channel

3.1 Introduction

Ervin and Tryggvason (1997) showed that the lift force on a clean non-deformable bubble rising in a vertical shear flow is directed toward the side where the fluid moves faster past the bubble, i.e. the lift co-efficient is positive. Therefore, in vertical channels, where the fluid velocity is zero at the walls, the bubbles will therefore move laterally toward the walls for upflow (where pressure gradient drives the flow upwards) and away from the walls in downflow (where pressure gradient drives the flow downwards). Lu, Biswas and Tryggvason (2006) used direct numerical simulations to examine the motion of equal-sized non-deformable bubbles in a vertical channel. They found, the average mixture density changes due to this lateral motion. For upflow as bubbles are driven to the walls, from the middle of the channel, eventually the mixture density increases to a point where the weight of the mixture is balanced by the pressure gradient. The shear therefore becomes zero and the lateral migration of the bubbles stops. Similarly, for downflow, as the bubbles are driven away from the walls the mixture density in the middle of the channel decreases until the mixture is buoyant enough to match the pressure gradient and the shear in the middle becomes zero. Thus, for both upflow and downflow lateral migration of the bubbles changes the mixture density in the middle of the channel in such a way, that, the shear becomes zero and further lateral migration of the bubbles is stopped. For upflow the result is a bubble rich layer near the walls but for downflow the wall-layer is depleted of bubbles. Though they have proposed a simple

analytical model for the flow, which agrees excellently with the DNS results, the model itself is limited to the particular situation and cannot be applied generally. Also the model cannot predict velocity and the flow rate in the upflow case.

In this study, the applicability of more general two-fluid models to bubbly flows in a vertical channel that can be simulated by direct numerical simulations relatively easily is examined. To reduce the computational cost, only a two-dimensional system is considered. This allows for more than one simulation to be performed and hence allows for parametric studies to be conducted relatively easily. The results are then compared with predictions obtained using the two-fluid model of Antal, Flaherty and Lahey, 1991. The key questions are how well the model, derived using small bubbles and a dilute flow, performs in situations that are easily simulated (large bubbles and dense flow), and how large a system needs to be and for how long the evolution must be simulated to reach an approximate steady state that can be compared with the two-fluid model?. Finally, the effect of deformability of the bubbles on the system is examined.

3.2 Nearly spherical bubbles: DNS results and two-fluid modeling

3.2.1 Problem setup

In this study, the steady state flow of bubbles in a vertical channel is examined, with gravity acting downward parallel to the walls, for both up and down flow. See figure 3.1, where the vertical coordinate is defined as y and x is defined as the cross-channel coordinate. The flow is driven by a pressure gradient in the y direction, but on the average the flow is assumed to be homogeneous in that direction. Therefore $\partial/\partial y = 0$ (except that $dp/dy = \text{constant}$). The flow in the channel is characterized by the Reynolds number

without bubbles. In this study, investigations are limited to systems with bubbles of only one size, so the bubble motion is determined by the Morton number, M , and the Eötvös number, Eo . In addition, either the number of bubbles n_b or the void fraction α needs to be specified. The governing non-dimensional numbers therefore are:

$$\text{Re}_{ch} = \frac{\rho_l H U}{\mu_l}; Eo = \frac{\rho_l d_b^2 g}{\sigma}; M = \frac{g \mu_l^4}{\rho_l \sigma^3}; \alpha = n_b \pi \frac{d_b^2}{4}$$

Here H is the width of the channel, U is the average velocity in the channel before the bubbles are added, ρ_l and μ_l , are the liquid density and viscosity, respectively, σ is the surface tension, g is the gravity acceleration, and d_b is diameter of the (non-deformed) bubbles.

3.2.2 The two-fluid model

The two-fluid model that is examined here is based on writing separate conservation equations for each phase. By assuming a fully developed, steady-state flow, and that the density of the bubble phase can be neglected, Antal, Lahey, and Flaherty (1991), derived a model for laminar bubbly flow in a circular pipe. For the two-dimensional flow in figure 3.1, the corresponding equations are

$$\alpha \frac{dp_g}{dy} + \alpha \rho_g g_y = -\frac{3}{8} \frac{\alpha}{R_b} C_D \rho_l U_r |U_r| \quad (3.1)$$

$$(1 - \alpha) \frac{dp_l}{dy} + (1 - \alpha) \rho_l g_y = (1 - \alpha) \mu_l \frac{\partial^2 u_l}{\partial x^2} + \frac{3}{8} \frac{\alpha}{R_b} C_D \rho_l U_r |U_r| \quad (3.2)$$

$$\alpha \frac{\partial \alpha}{\partial x} \frac{|U_r|^2}{5} (1 - \alpha) = -\alpha C_l U_r \frac{\partial u_l}{\partial x} - \alpha \left(C_{w1} + C_{w2} \frac{R_b}{s} \right) \frac{U_r^2}{R_b} \quad (3.3)$$

Here, $\alpha = \alpha_g = 1 - \alpha_l$ is the void fraction of the air, U_r is the relative velocity of the bubbles with respect to the liquid, and u_l is the liquid velocity in the vertical direction.

The density and viscosity of the liquid are ρ_l and μ_l , respectively, and g_y is the gravity acceleration. The drag coefficient in (3.1) is given by

$$C_D = \frac{A}{\text{Re}} \left(1 + 0.1 \text{Re}^{0.75}\right), A = 24 \quad (3.4)$$

where the Reynolds number and the effective viscosity are given by

$$\text{Re} = \frac{2R_b \rho_l |U_r|}{\mu_m}, \quad \mu_m = \frac{\mu_l}{1 - \alpha} \quad (3.5)$$

The pressure gradients in the gas and the liquid are taken to be equal and given and the average void fraction is used when computing the Reynolds number in (3.5). The first equation is the momentum conservation equation for the gas phase in the vertical direction (y), where the vertical pressure gradient and the weight of the liquid are balanced by the drag force due to the bubbles. The second equation is the vertical momentum equation for the liquid phase showing that the vertical pressure gradient and the weight of the liquid on the left hand side are balanced by the liquid shear and drag force on the right hand side. The third equation is the gas momentum equation in the horizontal direction (x), where the bubble advection (left hand side) is balanced by the lift force (first term on the right) and the wall repulsion force. The wall repulsion (last term on the right) is given by the model of Antal, Lahey and Flaherty (1991). Here s is the distance to the closest wall and the wall repulsion force, which is always away from the wall, is set to zero for s large enough to yield a force toward the wall. The coefficients used here are taken from Azpitarte and Buscaglia (2003) who used: $C_{w1} = -0.106$, $C_{w2} = 0.147$ and $C_L = 0.05$.

To solve these equations the domain is discretized using 501 grid points, which is more than enough to give fully converged results for the parameters examined here. Initially, it is assumed that the void fraction is constant and the liquid velocity is zero. Initially,

equation (3.1) is solved for U_r . Then equation (3.2) is solved implicitly using a tri-diagonal solver to find $u_l(x)$ and finally equation (3.3) gives $\alpha(x)$ by marching from one wall to the other. The new α is then used to solve (3.2) again for the liquid velocity, (3.3) gives a new void fraction and so on, iteratively until the solution has converged. For the solution of (3.2) the boundary conditions $u_l(0) = u_l(H) = 0$ are used. After the solution has converged, $\alpha(x)$ is corrected to conserve α , i.e.

$$\alpha^{new}(x) = \alpha(x) + \alpha_o - \frac{1}{H} \int_0^H \alpha(x) dx \quad (3.6)$$

where α_o is the specified average void fraction. This generally results in negative values for the void fraction near the walls. In the plots of $\alpha(x)$ the negative values are replaced by zeroes.

3.2.3 Results

To study the system sketched in figure 3.1, the motion of 72 bubbles is followed as they rise in a vertical channel for both upflow and downflow. For the upflow the liquid velocity increases the rise of the bubbles and for the down flow the liquid flow slows them down, relative to a stationary observer. The fluid shear near the walls has different sign for the different flow directions. Here $Eo = 0.5$, $M = 1.25 \times 10^{-5}$, and $\alpha_o = 0.1206$. The channel Reynolds number without bubbles is $Re=823.51$. The length of the computational domain is three channel widths and periodic boundary conditions are imposed in the streamwise direction. The domain is resolved by a 256 by 769 grid, except for the two cases with smaller bubbles (discussed later) where a 384 x 1152 grid is used. Grid refinement studies have shown that this resolution results in essentially fully converged solution. The simulation for the upflow took around 4 days and 22½ hours to

run up to 35381 steps and time=75.0. The computations are done on a dedicated Intel(R) Xeon 2.40GHz processor node. Other runs also took comparable times. For computational convenience the bubble density and viscosity are taken to be one twentieth of the liquid. As discussed by Esmaeeli and Tryggvason (1999), reducing the density and viscosity of the bubbles has essentially no impact on the results. The flow is initially started using the velocity profile predicted by the two-fluid model for these parameters, but the bubbles are uniformly distributed across the channel. Since gravity acceleration points downward, the bubbles rise upward, relative to the liquid, in both cases.

Figure 3.2 shows the bubble distribution and the streamlines at a late time for two simulations (upflow and downflow). In figure 3.3 and figure 3.4 the vorticity contours and velocity field is shown with the bubble distribution for the same simulations. In the frames on the left of figures 3.2-4 the pressure gradient is set to generate upflow and for the right frames the pressure gradient is reversed, resulting in down flow.

As expected, the bubbles remain essentially cylindrical, even in the high shear region near the walls and the lift of a bubble rising relative to the fluid is toward the slow moving fluid. Thus, the lift force pushes a bubble toward the wall for upflow and toward the middle of the channel for down flow. In most of the channel, however, the void fraction and the velocity are relatively uniform. Indeed, the distribution of the bubbles in figure 3.2-4 do not look fundamentally different, although it can be seen that there is, on the average, a larger number of bubbles near the wall for the upflow than for the down flow. For the down flow, in particular, bubbles do not hug the wall for long periods of time unlike the upflow. Since the bubble distribution in figure 3.2-4 is at only one time step, it needs to be verified whether this is true at other times as well. In figure 3.5 the

path of the bubbles over a length of time is plotted after the system has reached statistical steady-state. The left frame shows the path of bubbles for upflow whereas the right frame shows the same for down flow. It is clear that for upflow some of the bubbles hug the wall for most of the time, whereas for downflow no bubble comes near the wall at any time. In the middle of the channel the nature of the rise of bubbles with time seems very different between upflow and downflow. In the upflow case the bubbles rise without much interaction. For downflow however bubble-bubble interactions seems much stronger. The reason for this is, for upflow the slip velocity of bubbles in vertical direction is in same direction of the liquid velocity. For downflow the slip velocity of bubbles in vertical direction is in opposite direction of the liquid velocity. Therefore the magnitude of absolute vertical velocity of bubbles is much larger for upflow than downflow. Hence the path of bubbles for downflow seems extremely irregular whereas in upflow, the path of the bubbles looks relatively straightforward.

To quantify the evolution of the flow, and to assess whether the flow is at steady-state, in figure 3.6 the average rise Reynolds number of the bubbles (a), the average through flow (b), and the average root mean squared (rms) distance of the bubbles from the centerline of the channel (c) is plotted with time. In both cases the flow has reached a relatively well-defined steady-state, but the upflow case shows a significantly longer transient and may be undergoing small long-time oscillations. Since the number of bubbles is relatively small, the average bubble velocity shows higher frequency fluctuations than the through flow, which is found by integrating over the whole domain. The relatively uniform distribution of the bubbles is clear in the root mean square distance of bubbles from the

centerline (c), where it can be seen that although the bubbles in upflow are closer to the walls, the difference is relatively small.

Once the flow reaches an approximately steady state, well-defined average void fraction and liquid velocity profiles can be calculated. In figure 3.7, the average void fraction, computed by averaging over the y direction and over several times is plotted after the flow reaches an approximately steady-state, as a function of x . Frame (a) corresponds to the upflow in the left frame of figure 3.2 and frame (b) to the down flow in the right hand side of figure 3.2. In addition to the profiles computed from the results of the simulations, two-fluid model predictions for the void fraction profile, obtained by solving equations (3.1) – (3.3) is also plotted. At the center of the channel, agreement between theory and simulation is quite good. Like Lu, Biswas, Tryggvason (2006), it is also found, that the average mixture density at the center of the channel is such that, the mixture is in hydrostatic balance for both upflow and downflow. For the upflow, both the model and the simulation show a peak in the void fraction near the wall. The theoretical peak is, however sharper and closer to walls.

The average velocity profile, computed by averaging over the y direction and over several times after the flow reaches an approximately steady state is plotted versus x in figure 3.8 for both cases, again with the theoretically predicted velocity profile superimposed. Since the bubbles “homogenize” the flow, resulting in steep gradients in the liquid velocity near the walls, the average flow rate is significantly lower than for the original laminar flow without bubbles. For the domain simulated here the profiles are relatively symmetric, but it is important to note that preliminary simulations using a shorter channel (with the length equal to the width) frequently resulted in significant asymmetry in the velocity

profile, that lasted for a long time. For the upflow the model, using the original coefficients, overpredicts the velocity significantly but for the downflow the average values are closer.

The profiles predicted by the two-fluid model depend strongly on the various model parameters, such as the drag and the lift coefficient. In figures 3.7 and 3.8, The values for the various coefficients in equations (3.1) – (3.3) are taken from Azpitarte and Buscaglia (2003). These values are, however, derived for fully three-dimensional flows and there is no particular reason to expect the agreement with the present results to be very good. In the limit of zero Reynolds number, equation (3.4) is the drag for a solid sphere, not a bubble (since real bubbles are usually contaminated) and the drag of a two-dimensional cylinder is generally different than on a sphere with the same diameter. Furthermore, the drag in dense flows is generally higher than in dilute flows. To adjust the model coefficients it is natural to start by adjusting the drag. The average relative bubble Reynolds number (based on the channel width and the liquid properties) for the upflow case is $Re_r = 133.3$, which is very close to the relative bubbles Reynolds number found for bubbles rising in fully periodic domains with initially quiescent fluid ($Re_r = 124.9$). For the down flow, however, a slightly lower value, $Re_r = 92.1$ is found. The reason that the relative velocity is slightly lower for the down flow case is presumably that since the bubbles are pushed away from the walls, the effective void fraction in the center of the channel is slightly higher than for the upflow and the periodic case (see figure 3.4). Using the relative velocity for the upflow case, and equations (3.1), (3.4), and (3.5), it is found that the relative velocity can be matched by changing the coefficient in equation (3.4) from 24 to 18.3. This adjustment is well within the range of what can be expected. The

original coefficient is for a solid sphere and for a bubble it should be replaced by 16, but the finite void fraction and the two-dimensionality result in a slightly higher drag than for an isolated, clean, spherical bubble. However, even if the relative velocity is matched, the liquid velocity profile is sensitively dependent on the lift coefficient (and the wall repulsion model) and it is difficult to adjust the model in such a way that the peaks in the void fraction distribution are at the correct location. The difficulty is that equation (3.2) for the velocity has no free parameters, so once the void fraction is determined the velocity is in effect also given. In figure 3.9 the numerically obtained velocity and void fraction profiles for the upflow is plotted, along with several theoretical profiles obtained by adjusting the lift coefficient. Like Lu, Biswas, Tryggvason (2006), it can be seen that the velocity profile of the liquid is flat at the center of the channel. For $C_L=0.11$, the average velocity matches the simulation results. However, the main effect, of increasing the lift coefficient on the void fraction profile for upflow, is that the wall peaks of void fraction move significantly closer to the wall. This does not agree with the simulation results. It should also be noted that, the wall peak predicted by Antal et al. was also closer to the wall than the wall peak in the experimental data, they used for upflow. Although, the liquid velocity profile always remains flat at the center of the channel, for upflow it changes drastically in the region closer to wall, with the lift co-efficient. Surprisingly, the downflow results are found to be very insensitive to changing of the lift-coefficient. Due to these difficulties in adjusting the model to exactly match both the void fraction peak and velocity profile for upflow a detailed investigation to examine the flow structure around a bubble rising vertically near a no-slip wall is carried out in chapter 3.

It is very difficult to match both the void fraction and the velocity profiles from the simulation and the two-fluid model perfectly. However, the performance of the model is examined, both with the original and the “best” values from figure 3.9, for a number of other cases. In figure 3.10 effect of reducing the gravity by a factor of two for both the upflow and the down flow is shown by plotting the total through flow versus gravity. In addition to the results from the DNS (solid line), model predictions for the original parameters used in figures 3.6 and 3.7 (“model 1”) as well as for the “best” set from figure 3.6 (“model 2”) is also shown. For the downflow the effect of varying the parameters is very small, but for the upflow the model predictions is significantly improved by using the new values.

A similar test for the effect of the void fraction, changed by changing the number of bubbles in the channel is shown in figure 3.11. Here again the down flow shows good agreement between the DNS results and the predictions of the two-fluid model, for both sets of modeling parameters. For the upflow case the model with the adjusted parameters captures the DNS results nearly perfectly.

Finally, bubbles of different sizes are used, keeping the void fraction the same by changing the number of bubbles. The results are plotted in figure 3.12. Here again the down flow results are all relatively close, and the adjusted model parameters bring the two-fluid predictions in closer agreement with the DNS results. The agreement is, however, not quite as good as in figures 3.7 and 3.8, suggesting that either the simple adjustment that is made in the drag law (equation 3.4), may not capture the size effect well, or that the lift coefficient may need to be readjusted again.

3.3 Effects of deformability

In the previous section the behavior of circular non-deformable bubbles were investigated. It is found that the lift force plays a primary role in void fraction distribution. Ervin and Tryggvason (1997) showed that the direction of lift force on a deformable bubble rising in a vertical shear flow is directed toward the side where the fluid move slower past the bubble, i.e. the lift co-efficient is negative. Therefore, in channels, where the fluid velocity is zero at the walls, the bubbles will move away from the walls in upflow. This is completely opposite to what has been found for non-deformable bubbles.

To study the effect of deformability on the system a simulation of a upflow case is performed where the motion of 72 deformable bubbles is followed. The Eötvös number, E_o is chosen to be 4.0 but all other parameters (Morton Number, M ; Void fraction, α ; Number of the bubbles) are kept identical with the simulation of non-deformable bubbles.

Figure 3.13 shows the streamlines (left frame), vorticity contours (middle frame) and velocity distribution (right frame) with the bubble distribution. Figure 3.14 shows the path of the bubbles over a length of time after the system has reached statistical steady-state. The flow is initially started using a parabolic velocity profile. Since the acceleration due to gravity points downward, the bubbles rise upward, relative to the liquid. Since the bubbles deforms into ellipsoidal shape, the lift of a bubble rising relative to the fluid is away from the wall and towards the middle of the channel. Indeed, it is clear from figure 3.13 that not a single bubble is near the wall. However, the void fraction is relatively uniform in the middle of the channel. It is also from figure 3.14 that no bubble comes near the wall at any time. Figure 3.15 shows the numerically obtained void fraction and

velocity profiles for the upflow, for both deformable and non-deformable bubbles. It can be seen that unlike the non-deformable bubbles, the deformable bubbles is concentrated at the center of the channel and there is no wall peak. Also the velocity profile is not flat in the middle of the channel for deformable bubbles. This is expected, because, as the bubbles move towards the middle of the channel, the mixture in the middle of the channel becomes less heavy and hence, under an applied upward pressure gradient, the velocity profile has a non-zero gradient.

3.4 Summary

The study reported here is obviously only a modest first step in bridging the gap between direct numerical simulations of multiphase flows and two-fluid models. Bubbly flow in a very simple geometry is chosen as the model problem, since this flow has been studied extensively experimentally and two-fluid modeling of this setup has been relatively easy. Although the two-fluid model clearly had some inadequacy for upflow, especially, near the wall, overall, reasonable agreement with the simulation results is achieved. While only two-dimensional flows are studied here, the reasonably good agreement obtained (with relatively minor adjustment of the model to account for the two-dimensionality) confirms that it is possible to simulate multi-bubble systems that are sufficiently large so they are well described by two-fluid models. While this is perhaps not too surprising, it is nevertheless not a completely trivial issue either. Normally it cannot be expected that a system of two or three bubbles, for example, to be accurately modeled by averaged models. And, indeed, it is found that simulations using shorter channels (with the length equal to the width) resulted in large asymmetries. Two-fluid models are usually derived under the assumption that the system under consideration is either “infinitely large” or,

more properly, that the model describes the behavior of an ensemble of infinitely many realizations. Thus, the question is, how large of a system is large enough? As direct numerical simulations are generally limited to relatively small systems, finding that the domain of validity extends to those systems that can be computed easily, allows us to use the simulations results for calibration of the models. And as our results showed, adjusting the model parameters for one case, leads to a relatively good predictions when the governing parameters are changed—at least within the range of parameters examined here. Finally the effects of deformability of the bubbles on the system are also studied. It is found that the behavior of the system with deformable bubbles is remarkably different from the system with non-deformable bubbles.

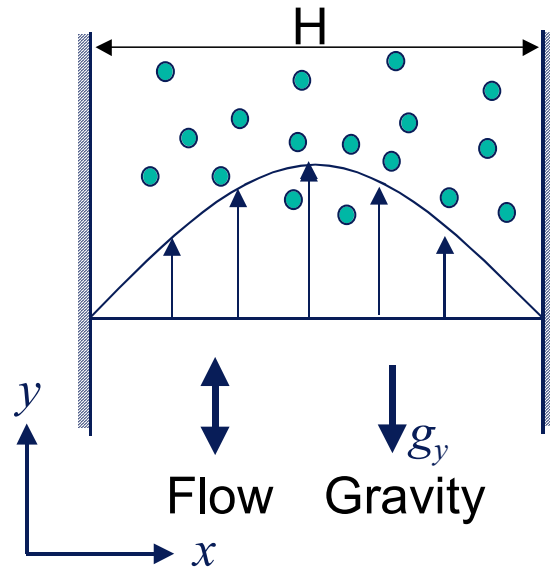


Figure 3.1 The problem setup. The flow is fully developed and at steady-state. The width of the channel is H , the average velocity in the absence of bubbles is U , gravity acts in the negative y direction and the pressure gradient is selected to generate either up or down flow.

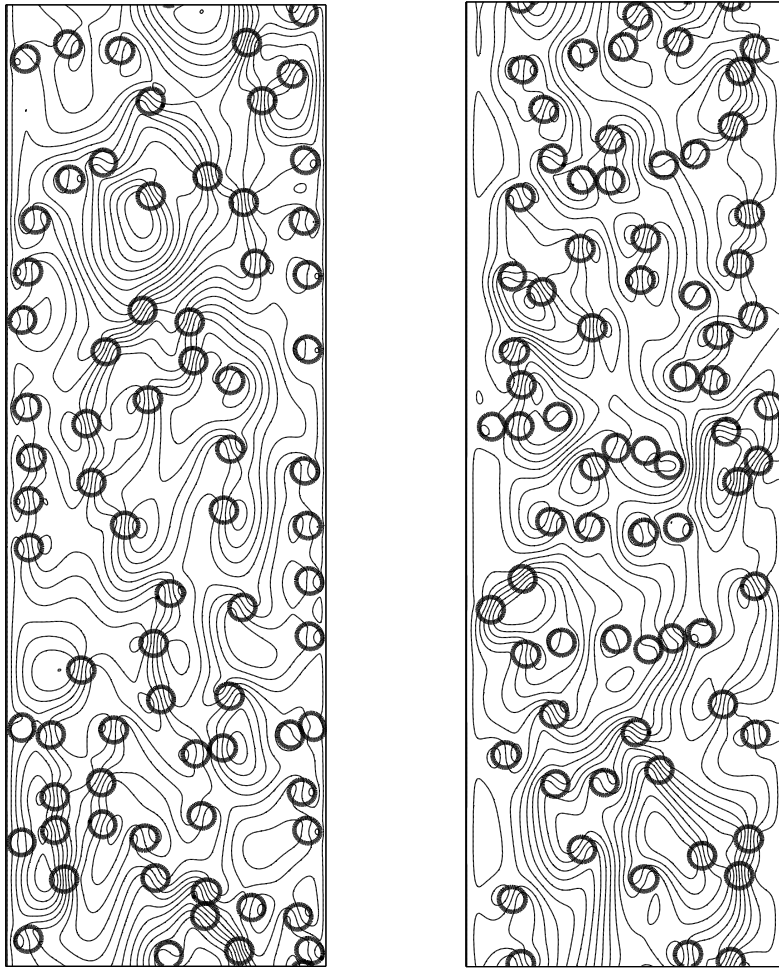


Figure 3.2 Two simulations of the rise of bubbles in upflow in a vertical channel (left frame) and downflow (right frame). The bubbles and the streamlines in a stationary frame of reference are shown at a late time after the flow has reached a statistically steady-state.

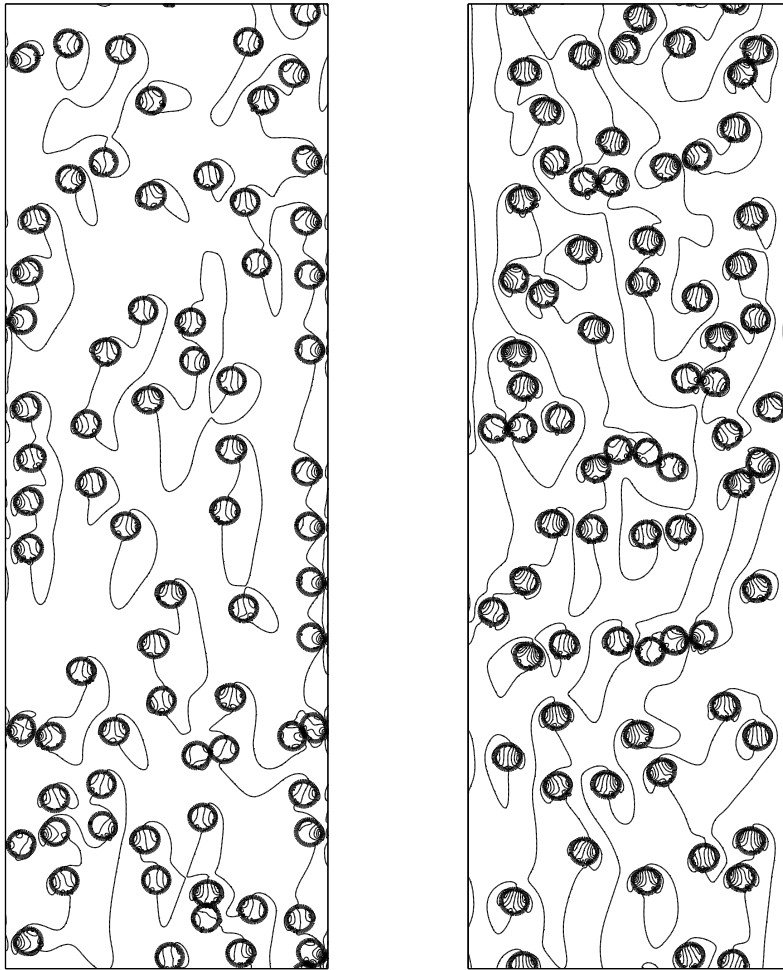


Figure 3.3 Two simulations of the rise of bubbles in upflow in a vertical channel (left frame) and downflow (right frame). The bubbles and the vorticity contours in a stationary frame of reference are shown at a late time after the flow has reached a statistically steady-state.

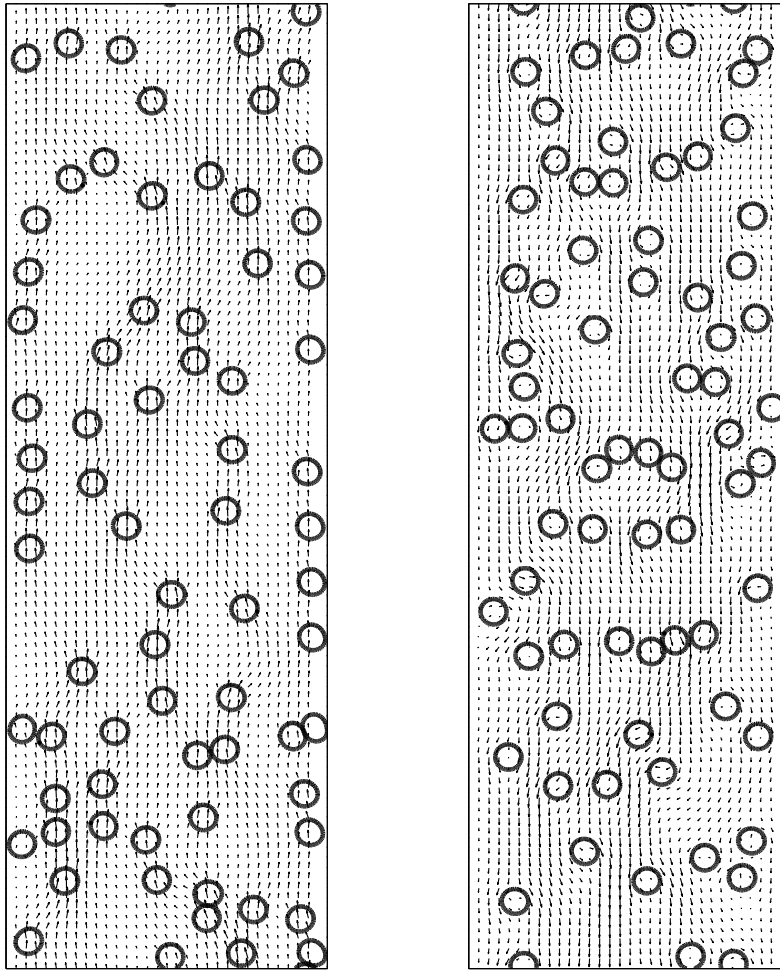


Figure 3.4 Two simulations of the rise of bubbles in upflow in a vertical channel (left frame) and downflow (right frame). The bubbles and the velocity field in a stationary frame of reference are shown at a late time after the flow has reached a statistically steady-state.

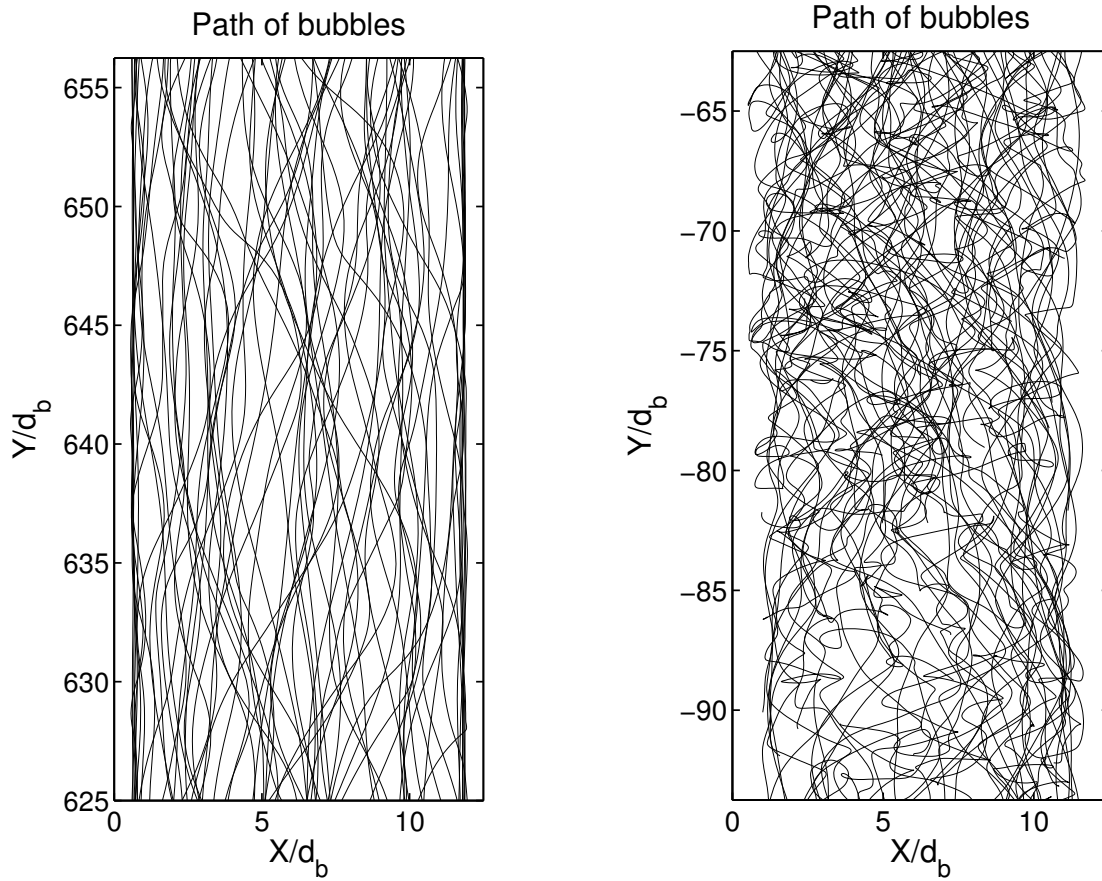
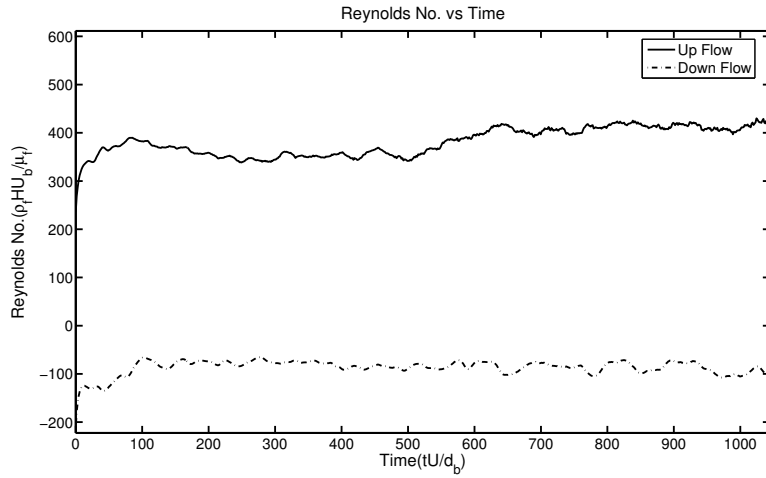
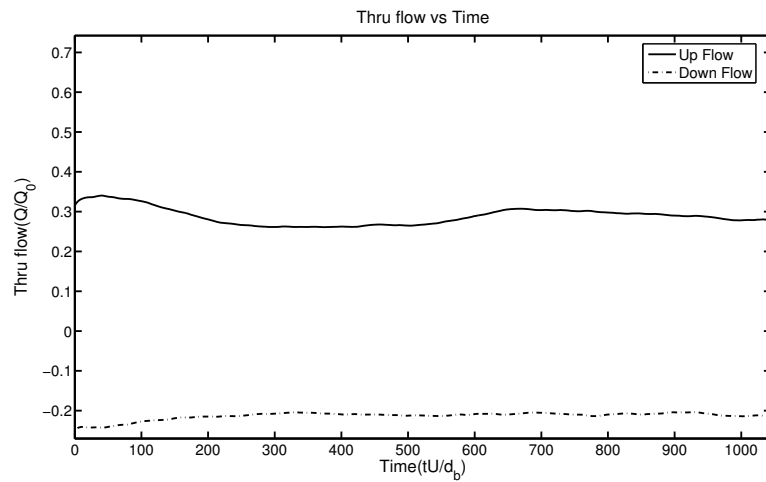


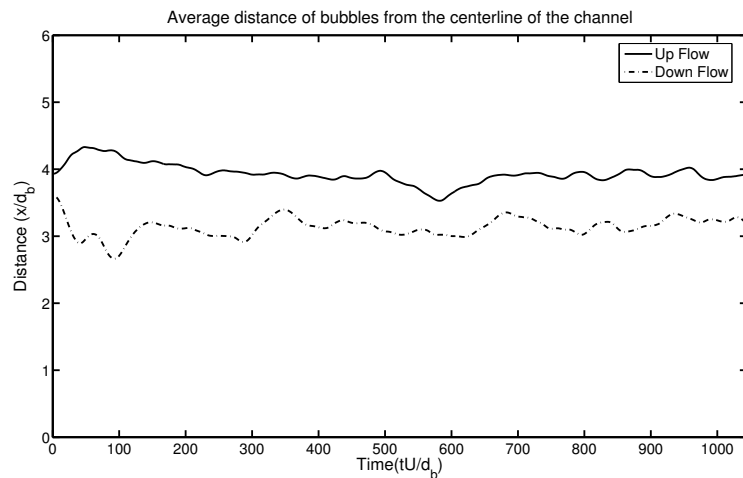
Figure 3.5 Two simulations of the rise of bubbles in upflow in a vertical channel (left frame) and downflow (right frame). The path of the bubbles are shown after the flow has reached a statistically steady-state.



(a)



(b)



(c)

Figure 3.6 The average bubble rise Reynolds number (a), the through flow normalized by the channel flow without bubbles (b) and the root-mean-squared distance of the bubbles from the centerline of the channel, normalized by half the channel width (c).

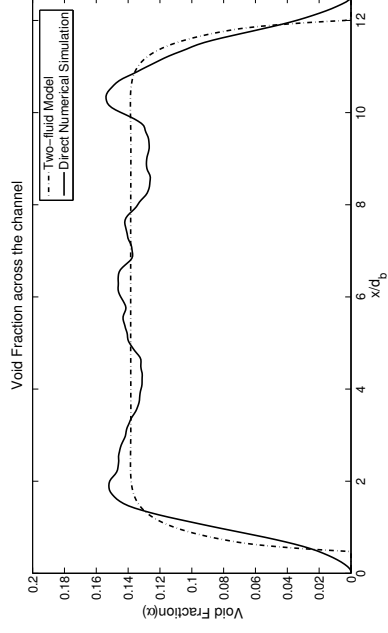
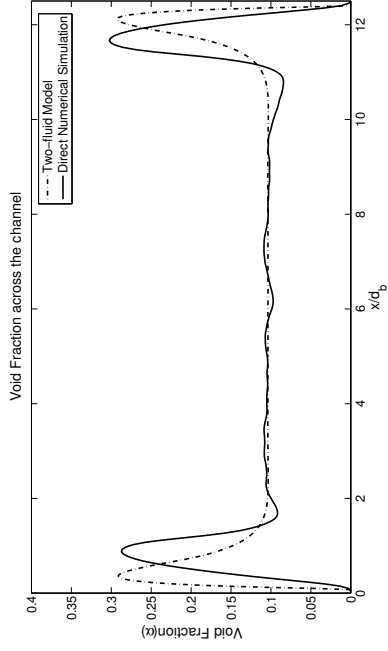


Figure 3.7 The averaged void fraction profile from the simulations and as predicted by the two fluid model, using the original values for the model coefficients. Results for upflow are shown on the left and for down flow on the right.

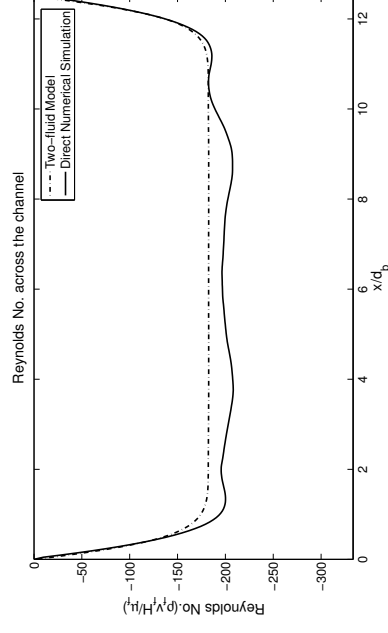
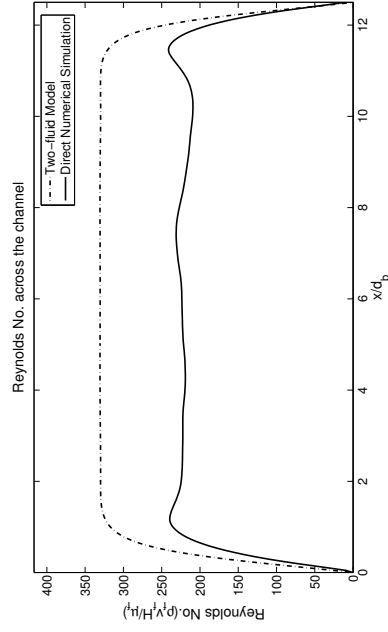


Figure 3.8 The averaged velocity profile from the simulations and as predicted by the two fluid model, using the original values for the model coefficients. Results for upflow are shown on the left and for down flow on the right.

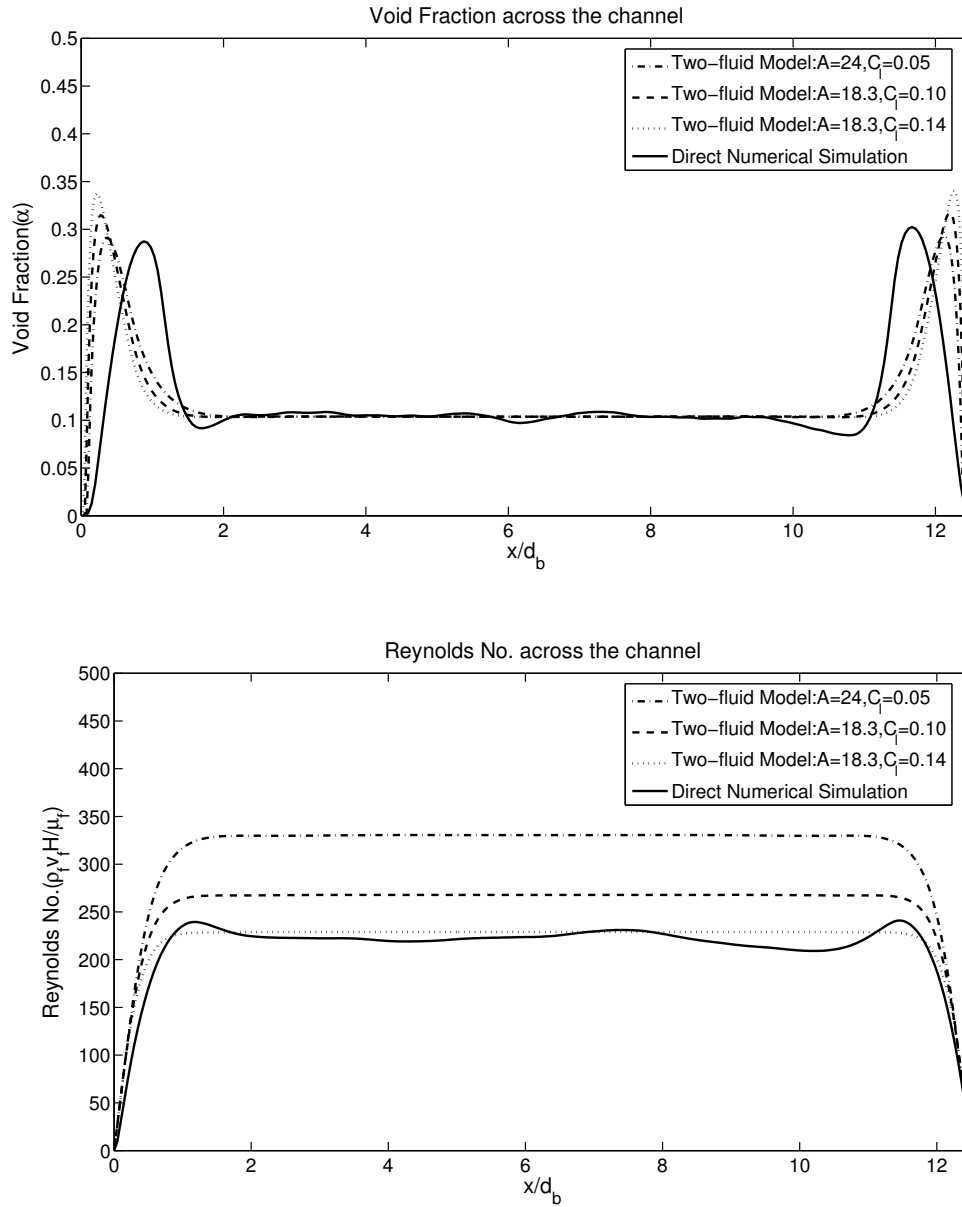


Figure 3.9 The effect of adjusting the model coefficients for the upflow case. The result from the full simulations, along with three profiles obtained by the two-fluid model are shown. The averaged fluid Reynolds number is on the left and the void fraction is on the right. The values of the leading numerical coefficient in equation (3.5) are 24, 18.3, 18.3 and the lift coefficient is 0.05, 0.10, 0.14, for the three different model profile shown.

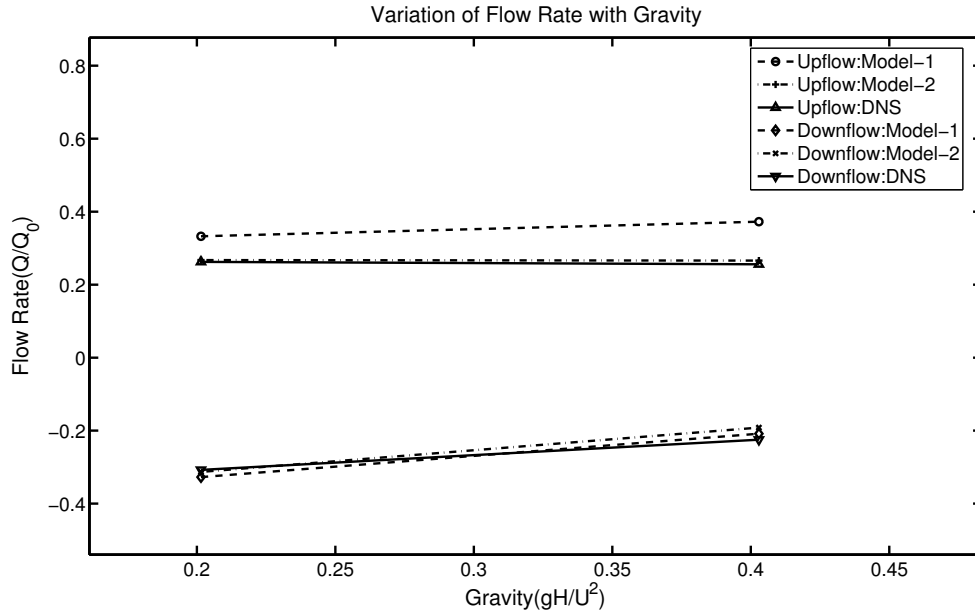


Figure 3.10 Total flow rate for different values of gravity as predicted by the full simulations and a two-fluid model with two sets of model parameters.

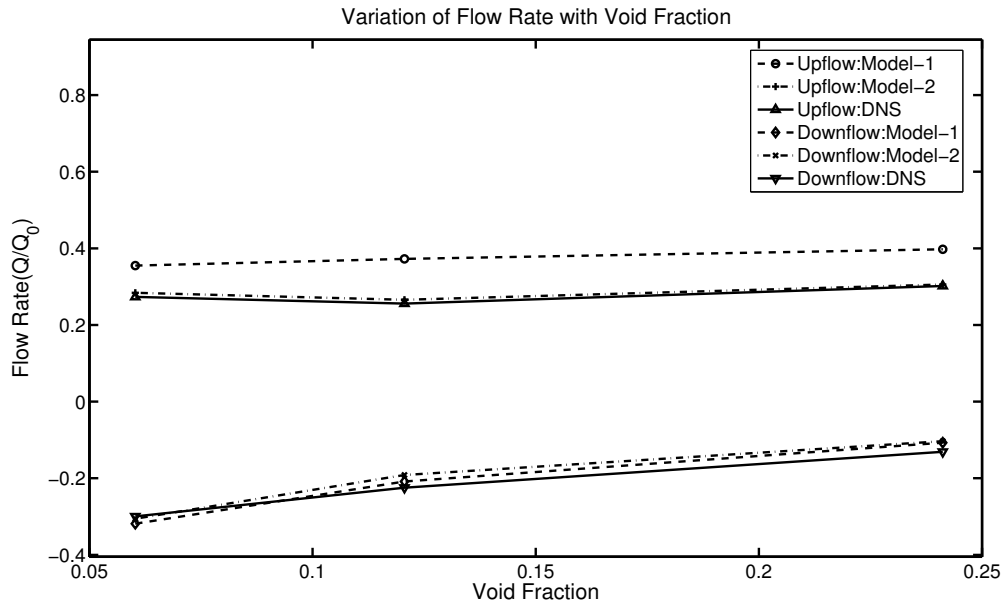


Figure 3.11 Total flow rate for different values of the void fraction, changed by changing the number of bubbles, as predicted by the full simulations and a two-fluid model with two sets of model parameters.

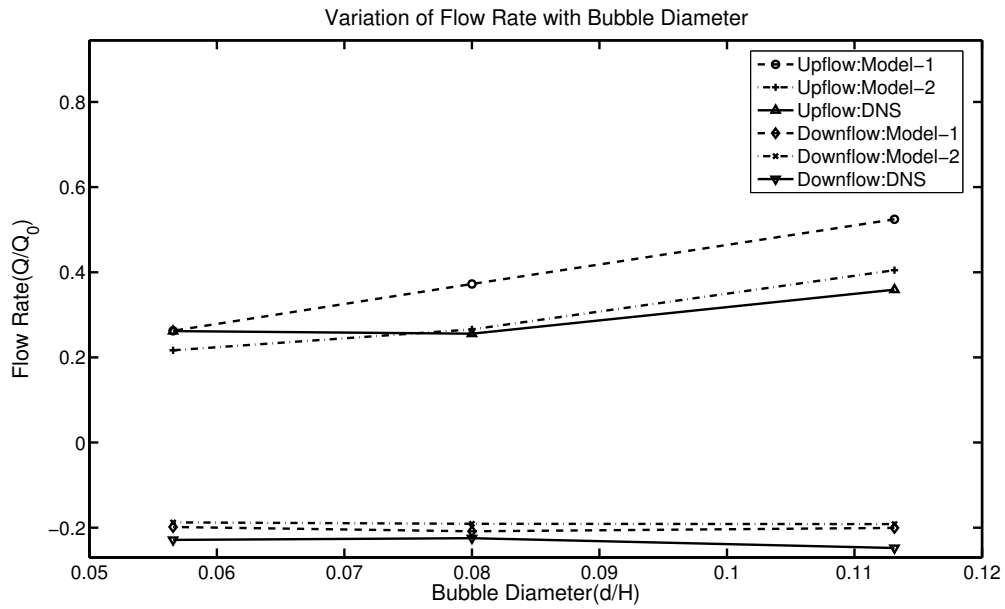


Figure 3.12 Total flow rate for different bubbles sizes, but the same void fraction as predicted by the full simulations and a two-fluid model with two sets of model parameters.

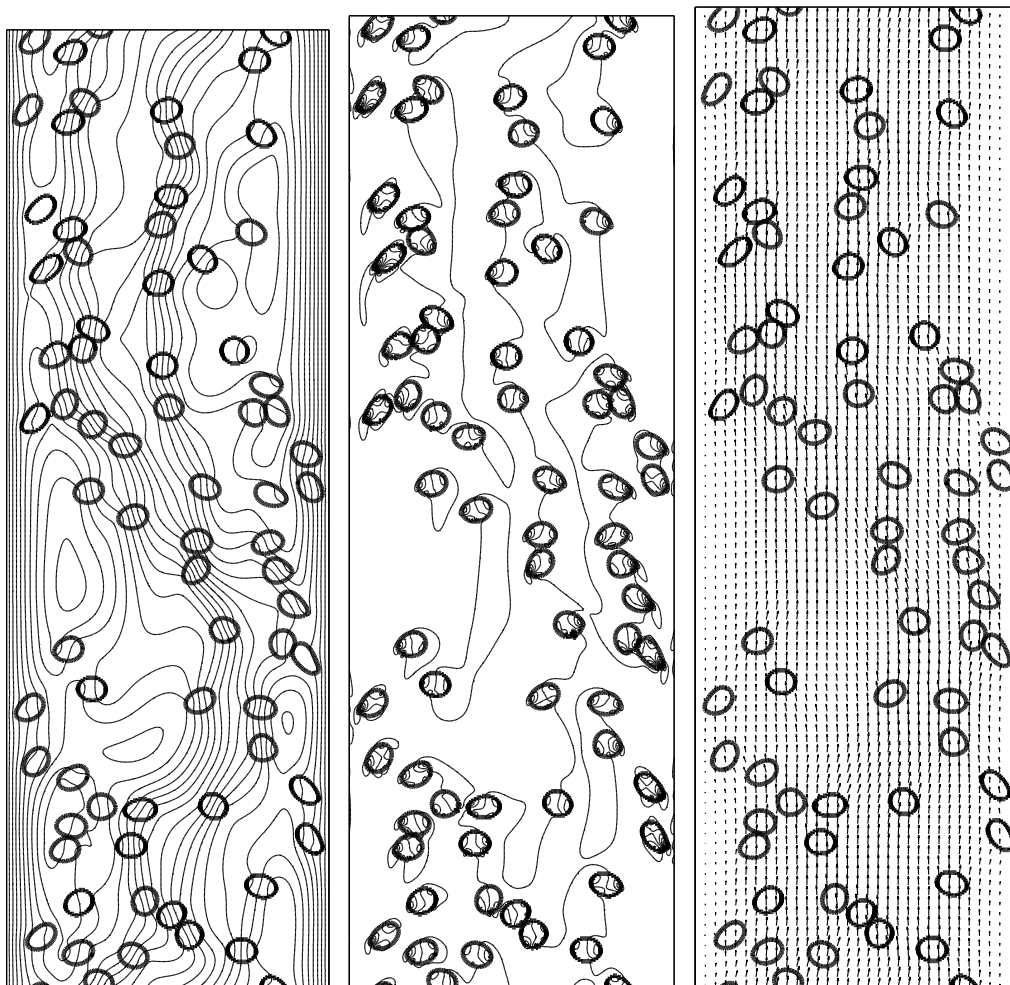


Figure 3.13 A simulation of the rise of deformable bubbles in upflow in a vertical channel. The bubbles are shown with the streamlines (left), vorticity contours (middle), and velocity field (right) in a stationary frame of reference are shown at a late time after the flow has reached a statistically steady-state.

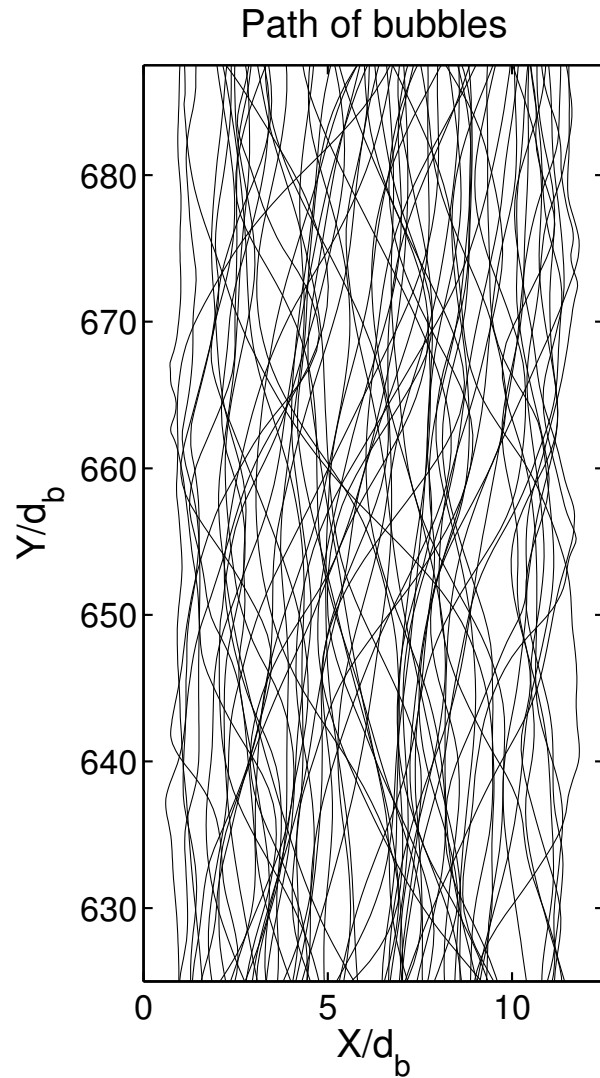
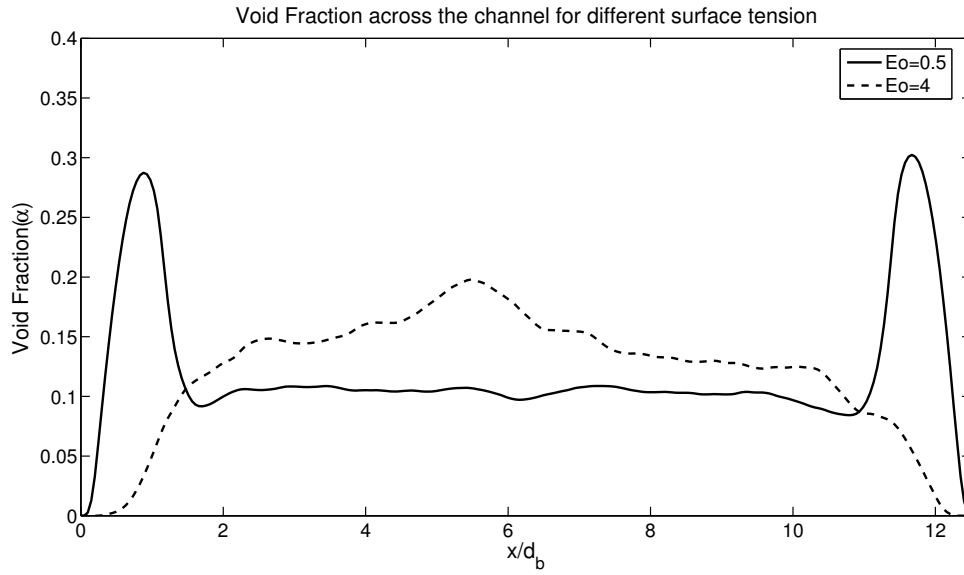
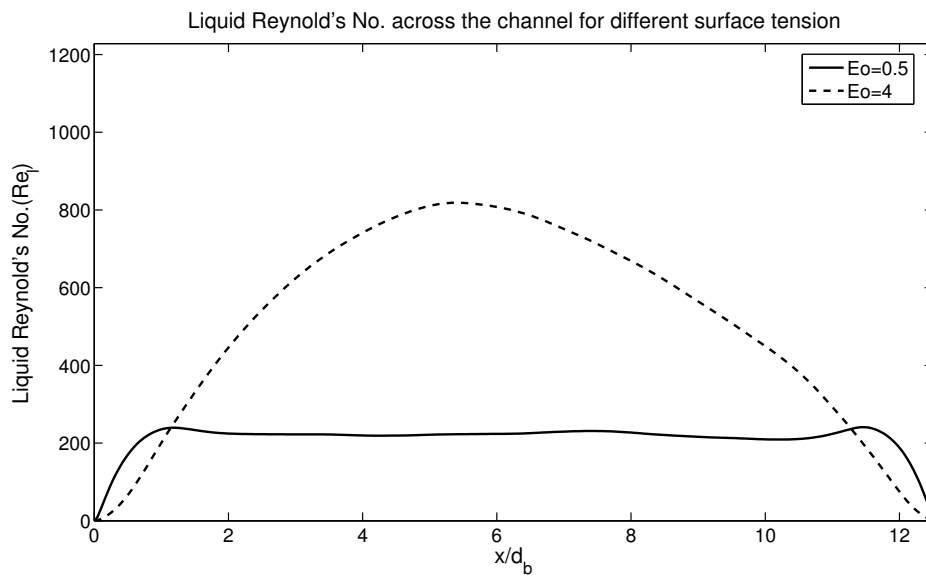


Figure 3.14 Paths of the rise of deformable bubbles in upflow in a vertical channel is shown at a late time after the flow has reached a statistically steady-state.



(a)



(b)

Figure 3.15 The averaged (a) void fraction and (b) velocity profile from the simulations for non-deformable and deformable bubbles.

CHAPTER IV

Bubbly wall-layers in a vertical channel

4.1 Introduction

Several researchers have focused on bubbly flows in vertical channels. Experimental investigations of turbulent flows include Serizawa, Kataoka and Michiyoshi (1975), Wang, Lee, Jones and Lahey (1987), Liu and Bankoff (1993), Nakoryakov and Kashinsky (1981, 1996), Liu (1997), Kashinsky, Randin, and Timkin (1999), So, Morikita, Takagi, and Matsumoto, (2002), Guet, Ooms and Oliemans (2005), and Mudde and Saito (2005), and Matos, Rosa and Franca (2004). These experiments all show that nearly spherical bubbles in upflow result in a wall-peaking of the void fraction but a bubble free wall-layer for downflow. The velocity in the core of the channel is nearly uniform in both cases. Experiments of laminar flow upflow include Song, Luo, Yang, and Wang (2001) who studied flows with both uniform and non-uniform distribution of bubble sizes and Luo, Pan, and Yang (2003) who examined the motion of light particles. Both studies were done for upflow and wall peaking was found in both cases. Modeling of bubbly flows in channels has generally treated the mixture using the two-fluid model where separate equations are written down for the motion of the liquid and the gas. Such models for turbulent flows can be found in Lopez De Bertodano, Lahey, and Jones (1987, 1994), Kuo, Pan, and Chieng (1997), Guet, Ooms and Oliemans (2005), Politano, Carrica, and Converti (2003) and Celik and Gel (2004). A two fluid model for laminar flow was developed by Antal, Lahey and Flaherty (1991) and analyzed in detail by Azpitarte and Buscaglia (2003).

In a recent paper, Lu, Biswas, and Tryggvason (2006) simulated the motion of several nearly spherical bubbles in laminar flow in a vertical channel, both for upflow and downflow, fully resolving all flow scales. The simulations showed that in both cases the flow consists of two well-defined regions: A thin wall-layer and a homogeneous core, occupying most of the channel. The formation of these regions is due to lift induced lateral motion of the bubbles. For a nearly spherical bubble rising due to buoyancy in a vertical shear, it is well known that the lift force pushes the bubble toward the side where the liquid is moving faster with respect to the bubble. Thus, in upflow a bubble near the wall is pushed toward the wall and in downflow the bubble is pushed away from the wall. In upflow the bubbles are therefore moved out of the core region, making the mixture heavier, and in downflow bubbles are added to the core, making it lighter. This process continues until the average weight of the mixture in the middle of the channel is balanced exactly by the pressure gradient. The shear is then zero and the further lateral migration of the bubbles stops. Thus for upflow, a layer rich in bubbles is produced near the wall. For downflow, a layer completely void of bubbles is formed near the wall. Lu, Biswas, and Tryggvason (2006) calculated the thickness of this layer exactly for the downflow and assumed it to be one bubble diameter thick for upflow. They also named these layers as wall-layers. It is only in these wall-layers where there is a non-zero velocity gradient. For upflow where the weight of the mixture in the core is increased by pushing bubbles to the wall and the light, bubble rich mixture in the wall-layer is driven upward by the imposed pressure gradient. For downflow, on the other hand, bubbles must be drawn away from the wall to decrease the weight of the mixture in the core and the dense bubble-free wall-layer is driven downward by its weight and the imposed pressure gradient. As discussed in Lu, Biswas, and Tryggvason (2006), the distribution is stable in the sense that if too

many bubbles end up in the wall layer for upflow, the core slows down with respect to the wall layer, thus generating a shear that will drive the bubbles out of the wall-layer. Similar if too many bubbles end up in the core for downflow, its velocity is reduced and bubbles are driven back to the wall.

For downflow, where the wall-layer is bubble free, the velocity profile is easily found by integrating the Navier-Stokes equations for steady laminar parallel flow and the flow rate can be predicted analytically, with a fair degree of accuracy. For upflow, on the other hand, the presence of the bubbles makes the situation more complex and the velocity profile is not as easily found. Biswas, Esmaeeli, and Tryggvason (2005) tried to apply the two-fluid model of Antal, Flaherty and Lahey (1991) but had significant difficulties in adjusting the model coefficients to match the simulation results for upflow. In particular, the velocity profile near the wall (wall layer) is found to be extremely sensitive to model coefficients in the wall layer. Since the velocity increase across the wall-layer determines the liquid velocity in the core of the channel, it is critical for predicting the total flow rate. For the most part the bubbles in the wall layer interact only weakly with the bubbles in the core layer and as a first approximation it seems that they can be neglected, as long as the fluid is in hydrostatic equilibrium and the shear there is zero. In this study the dynamics of a bubbly wall-layer at relatively modest Reynolds numbers is examined. The bubbles in the core region are neglected. Any shear in the core region is eliminated by applying a body force adjusted to balance the pressure gradient there. Thus the flow is completely determined by what happens in the wall-layer, which is the case for bubbly upflow. The average properties of the flow in the wall layer are examined and compared with a simple two-fluid model. The motion of many bubbles sliding along a (slightly

tilted) wall has been studied experimentally for quiescent flow by Kitagawa, Sugiyama and Murai (2004) but the authors are not aware of studies where the liquid is flowing.

4.2 Upward bubbly flow near a no-slip wall and averaged equations.

If it is assumed that the bubble layer near the wall is approximately one bubble diameter thick (which is the case except for very high void fraction flows) the void fraction profile of the flow can be analytically calculated from the phasic conservation of mass of both phases. The velocity of the liquid becomes uniform in the middle of the channel (Lu et. al. 2005). The value of this velocity depends on the dynamics of the flow in the bubble rich wall layer whose void fraction is already known. This provides the motivation for studying the flow only in the wall layer. In this study rise of a single bubble in periodic array in the wall layer is examined. Effect of governing parameters on the slip velocity of the liquid across the bubble layer is studied. Effect of more than one interacting bubbles rising near the wall is also investigated.

Figure 4.1(a) shows the schematic diagram of the problem setup. Since main interest of this study is in the mechanics of the bubble layer, the full width of the channel is not simulated. Instead a wall bounded vertical channel where the walls are only two bubble diameter apart in x direction is chosen to save the computational cost. The left wall is chosen as a no-slip wall but the right wall is chosen as a full-slip one. The computational domain is periodic in the direction of the walls and in the flow direction. The length of the domain in these directions is determined to obtain a desired void fraction in the wall layer. In the region outside the wall layer ($x > D$) a body force is applied in addition to the normal gravity to make the flow hydrostatically balanced. This ensures that there will be

no velocity gradient outside the bubble layer in steady state and the velocity boundary conditions just outside the bubble layer is identical to that of the actual channel. Flow in the bubbly wall-layer is governed by the following one-fluid momentum equation

$$\frac{\partial \rho \mathbf{V}}{\partial t} + \nabla \cdot \rho \mathbf{V} \mathbf{V} = -\nabla p + \nabla \cdot \boldsymbol{\tau} + \rho \mathbf{g} + \oint_{s^f} \sigma \kappa \mathbf{n} \delta(x - x^f) ds \quad (4.1)$$

A mathematical description of the averaged quantities of the flow can be written by volume averaging equation (4.1) along plane slices parallel to the wall. Figure 4.1(b) shows a schematic diagram of such an averaging volume. If steady-state and fully-developed flow is assumed, the resulting equation will not involve any derivative of unknown quantities in y and z direction (Figure 4.1(b)). The transient and convective terms also vanishes. Such averaging has already appeared in the literature many times over. So, a detailed derivation is not provided and the resulting equation is given below.

$$-\frac{\partial p}{\partial z} + \frac{\partial \tau_m}{\partial x} + \rho_m g_z + \frac{1}{\nabla} \int \sigma \kappa n_z \delta(x - x^f) dV = \frac{\partial \langle \rho u' w' \rangle}{\partial x} \quad (4.2)$$

Here τ_m is the combined viscous stress of the two phases. $\rho_m (= \alpha_g \rho_g + \alpha_l \rho_l)$ is the mean density and mean pressure gradient respectively. Assuming τ_m can be written in a Newtonian shear law form, using an effective viscosity $\mu_m (= \alpha_g \mu_g + \alpha_l \mu_l)$ equation (4.2) can be written as,

$$-\frac{\partial p}{\partial z} + \mu_m \frac{\partial^2 \bar{w}_m}{\partial x^2} + \rho_m g_z + \frac{1}{\nabla} \int \sigma \kappa n_z \delta(x - x^f) dV = \frac{\partial \langle \rho u' w' \rangle}{\partial x} \quad (4.3)$$

Here \bar{w}_m is the mean velocity of the combined flow of bubbles and liquid. The last term in the LHS of equation (4.3) arises due to distribution of the surface tension force across the bubble. Prosperetti and Jones (1994) have shown that total force exerted by surface tension on a close surface vanishes. Thus, if the averaging volume of the averaged

equation totally encloses the bubble then there will be no contribution of this term. But in this study the dynamics of the flow in the wall layer which is approximately one bubble diameter thick is investigated. Since the velocity gradient is high near the wall the bubble is expected to deform more than it does normally in the wall layer. So for a meaningful study averaging volume must be less than one bubble diameter and this term cannot be dropped. Hence forth this term is referred as “local surface tension force”. The term in the RHS of the equation (4.3) is known as the “Reynolds stress”.

The “local surface tension force” is a not a closed term. Currently the authors are not aware of any study that can analytically model this term. “Reynolds stress” term is also not closed. In this paper, three-dimensional DNS results are mainly used to model these terms.

The flow in this wall layer is characterized by the slip Reynolds number of the wall layer. In this study only systems with uniform bubble size are considered. Hence the bubble motion is determined by the Morton number, N . The bubble motion is also governed by the Eötvös number, Eo . The average void fraction α_{av} and the relative importance of the pressure gradient and buoyancy, $\beta/g\Delta\rho$ also governs the flow. The governing non-dimensional numbers therefore are:

$$\text{Re}_{slip} = \frac{\rho_l D U_{slip}}{\mu_l}; \quad M = \frac{g \mu_l^4}{\rho \sigma^3}; \quad Eo = \frac{\rho_l D^2 g}{\sigma}; \quad \frac{\beta}{\Delta \rho g}; \quad \alpha_{av}$$

4.3 Results

To study the problem a 3-dimensional direct numerical simulation (DNS) is performed where the motion of a single nearly spherical bubble near a no-slip wall is followed. To

save computational cost the domain is selected to be two bubble wide x direction is chosen. The left side of the domain is a no-slip wall and the right side of the domain is chosen as a full-slip wall. The computational domain is periodic in y and z direction. The length of the domain in these directions is determined to obtain a desired void fraction in the wall layer. In the region outside the wall layer ($x > D$) a body force is applied in addition to the normal gravity to make the flow hydrostatically balanced. Table 4.1 shows various parameters describing the simulation. The values of the physical quantities are given in computational units. The non-dimensional numbers governing the run are also given. Since in the present study the main interest is in the steady state behavior and the transient phase is fairly long, sometimes the simulations are started using a bubble distribution and an initial liquid velocity profile that is close to the steady state.

The velocity field of the flow is shown in figure 4.2 after the flow has reached steady state. The bubbles and the iso-contours of vertical velocity are in a stationary frame of reference. It is clear that the bubble is hugging the no-slip wall. It is also clear that, the bubble has deformed slightly. The velocity gradient is very high near the no-slip wall, but is uniform outside the wall layer.

Figure 4.3 plots the path of the bubbles in a stationary frame of reference. It is clear that the bubble gradually move towards the wall under the action of the lift force until it almost hugs the wall. After that it stays there, hugging the wall while it rises upward due to buoyancy.

To assess how well the motion has converged to a steady state, the average velocity of bubbles versus time is plotted in figure 4.4(a). Through flow normalized by the channel

flow without bubbles is also plotted with time in figure 4.4(b). The flow rate is found by integrating the vertical fluid velocity over the whole computational domain and dividing by the height of the domain. It is obvious that after $t=35$ both the quantities have reached the steady state.

A convergence study of the problem is performed. For this a special case which is computationally small and hence can be computed for very fine grids is selected. Various parameters describing this case are also listed in table 4.1. Figure 4.5 shows average velocity of bubbles versus time for three different resolutions for this case. The coarsest resolution is $31 \times 32 \times 32$. The same computation is also performed on an intermediate grid of $47 \times 48 \times 48$ and a fine grid of $63 \times 64 \times 64$. It can be concluded from this figure that all computations are essentially converged.

Figure 4.6 shows the Reynolds stress term along the x direction. In figure 4.7 the local surface tension force along the x direction is plotted. From figure 4.7 it can be seen that though the total surface tension force integrated over the whole domain vanishes, it has significant non-zero values across the bubble in the wall layer. So this term cannot be neglected while solving equation (4.3). It can be concluded from figure 4.6 and 4.7 that for this case the Reynolds stress term is negligible compared to local surface tension force and contribution of this term can be neglected.

In figure 4.8 the average liquid velocity profiles in vertical (z) direction across the channel is shown. The velocity profiles are obtained from equation (4.3) and by post-processing the results of direct numerical simulation. The local surface tension force used in equation (4.3) is calculated by post-processing the results of direct numerical

simulation. The Reynolds stress term, being small, is neglected. From this figure it is clear that when the local surface tension term appropriately closed the averaged equation gives almost same results as the fully three dimensional direct numerical simulation.

The next logical step in this investigation is to study the effect of the change in governing parameters on the flow. In section 2 the non-dimensional parameters governing the flow are discussed. In the following sections effects of changing the non-dimensional parameters on the closure terms of equation (4.3) and ultimately the slip Reynolds number of the wall layer are examined. The density and viscosity ratio are chosen to be one-tenth. In all these studies the Reynolds stress is found to be essentially zero. Then the only unclosed term that significantly affects the flow and the slip Reynolds Number is the local surface tension force. In the following sections effects of governing parameters on these two quantities are examined.

4.3.1 Effect of void fraction

To check the effect of the void fraction of the wall layer (α_w) on the flow two more cases in addition to the baseline case is studied. The void fraction varies from $\alpha_w = 0.1839$ to $\alpha_w = 0.3039$. Figure 4.9(a) shows the steady state shape of the bubbles for three different void fractions. In figure 4.9(b) the local surface tension force across the channel is plotted. From figure 4.9(a) it can be seen that bubbles are almost identically deformed for different void fractions. Hence it is logical to infer that magnitude of local surface tension term should be directly proportional to α_w , because higher void fraction just means more bubble per unit volume. From the figure 4.9(b) it is clear that this is indeed the case. This fact allows us to model this term easily for different wall void fraction. In figure 4.9(c)

the slip Reynolds number of the wall layer with void fraction obtained from the direct numerical simulation and from the averaged equation is plotted. The local surface tension for the averaged equation is modeled by post-processing the results of direct numerical simulation. It can be seen that while the difference between results while essentially small, nevertheless, increases with increasing α_w .

4.3.2 Effect of non-dimensional pressure gradient

The effect of the non-dimensional pressure gradient $\left(\frac{\beta}{\rho g}\right)$ on the flow is studied by running two more cases in addition to the baseline case so that the non-dimensional pressure gradient varies from $\frac{\beta}{\rho g} = 0.03269$ to $\frac{\beta}{\rho g} = 0.11269$. In figure 4.10(a) the

steady state shape of the bubbles for three different pressure gradients is shown. In figure 4.10(b) the local surface tension force across the channel is plotted. From the figure

4.10(b) it is clear that magnitude of this term is proportional to $\left(\frac{\beta}{\rho g}\right)^{0.33}$. This allows us

to model this term easily for different wall void fraction. Figure 4.10(c) shows the slip Reynolds number of the wall layer with non-dimensional pressure gradient obtained from the direct numerical simulation and from the averaged equation. The local surface tension for the averaged equation is modeled by post-processing the results of direct numerical simulation. It can be seen that while the difference between results while essentially small.

4.3.3 Effect of Eötvös number

To check the effect of the Eötvös Number (EO) on the flow two more cases in addition

to the baseline case is studied. The Eötvös Number varies from $Eo = 0.25$ to $Eo = 1.00$. Figure 4.11(a) shows the steady state shape of the bubbles for three different Eötvös Numbers. In figure 4.11(b) the local surface tension force across the channel is plotted. From figure 4.11(a) it can be seen that though all the bubbles look almost spherical, the bubbles with lower Eötvös Number is less deformed. But, from figure 4.11(b) it is clear that magnitude of local surface tension term increase with decreasing Eötvös Number. This is because though the deformation is lower with decreasing Eötvös Number, higher surface tension coefficient results in the increase of this term despite lower deformation. Figure 4.11(c) shows the slip Reynolds number of the wall layer obtained from the direct numerical simulation and from the averaged equation with Eötvös Number. The local surface tension for the averaged equation is modeled by post-processing the results of direct numerical simulation. It can be seen that the slip Reynolds number increases with increasing Eötvös Number.

4.3.4 Effect of Morton number

The effect of the Morton Number (M) on the flow is studied by examining two more cases in addition to the baseline case. The non-dimensional pressure gradient varies from $M = 8 \times 10^{-8}$ to $M = 2 \times 10^{-5}$. In figure 4.12(a) the steady state shape of the bubbles for three different Morton Numbers is shown. It is clear bubbles with higher Morton Number are more deformed. In figure 4.12(b) the local surface tension force across the channel is shown. It is clear that magnitude of this term decreases with increasing Morton Number. This is expected because with higher viscosity the shear near the wall decreases. In figure 4.12(c) the slip Reynolds number of the wall layer obtained from the direct numerical simulation and from the averaged equation with Morton Number is plotted. The local

surface tension for the averaged equation is modeled by post-processing the results of direct numerical simulation. It can be seen that the slip Reynolds number decreases with increasing Morton Number.

4.3.5 Effect of bubble interactions

All of the above computations are conducted with a single bubble with periodic boundary conditions in direction perpendicular to the wall and flow direction. Esmaeeli and Tryggvason (1999) have observed that in a periodic domain with many bubbles the bubbles interact with each other and form different kind of structures depending upon the governing parameters. So it is an important question whether bubbles exhibit similar behavior when they are near the wall and whether this interaction affects the average flow parameters in a significant way. To answer this question two large computations one with four bubbles and another with sixteen bubbles is studied. In both cases to save on computational time steady state velocities from the single bubble case is duplicated in both the periodic directions and used as initial velocity profile. The bubbles are then randomly placed in the domain. Figure 4.13 shows the bubbles and the iso-contours of vertical velocity in a stationary frame of reference at a late time after the flow has reached a steady state. The left frame shows the 4 bubble case while the right frame shows the 16 bubble case. As the single bubble simulation the bubbles in these 4 and 16 bubbles simulations are also hugging the wall as expected. Figure 4.14 shows the path of the bubbles in these cases. Here it can be seen that while initially the bubbles are moving in lateral directions after reaching the steady-state they are generally rising in only vertical direction. Figure 4.15(a) shows the average velocity of bubbles versus time. Figure 4.15(b) shows the through flow normalized by the channel flow without bubbles versus

time. Both of them show little variation from the single bubble result at steady-state. In figure 4.16 the slip Reynolds number of the wall layer with the number of bubbles is plotted. It can be seen that the difference between 1, 4 and 16 bubble cases are negligible. From figure 4.14, 4.15 and 4.16 it can be concluded that the effect of bubble interaction is small for the flow in the wall layer.

4.3.6 Comparison with full channel simulation

A comparison with the wall layer run with the full channel simulation of Lu, Biswas and Tryggvason (2006) with identical parameters has been done. In figure 4.17 the average liquid velocity profile from both cases inside the wall layer is plotted with x -direction. It can be seen that near the wall the liquid velocity profile is almost identical for both cases. But after some distance in x -direction the velocity profile from the full-channel simulation becomes higher than that of wall-layer simulation. It can be observed that the gradient of velocity is almost but not exactly zero at the boundary of the wall layer and the channel core. But in the wall layer simulation zero velocity gradient condition at the boundary of the wall layer has been artificially enforced by adding a body force. The difference can be due to this second order effect.

4.4 Summary

Direct numerical simulations have been used to examine the steady-state flow of buoyant bubbles near a vertical wall. The flow can be described by a one dimensional volume averaged model. The simulations show that the fundamental assumptions of the model are correct. The only major problem is that there exist no analytical description for some terms (local surface tension force term and Reynold's stress terms) of the model and

hence the model cannot be analytically closed. The next best thing that can be done is to study the effect of the governing non-dimensional parameters on these terms and hence on the slip Reynolds number of the wall layer. These studies are particularly useful for establishing simple relationships between the unclosed terms and the governing parameters, if possible. In this study, it is already shown that the Reynold's stress term is negligible compared to local surface tension term in the vicinity of the wall.

The Reynolds stress terms are negligible in our cases and the local surface tension force is modeled from the computational studies. The only assumption in the averaged model is the constitutive relation of viscous shear stress with strain rate using an effective viscosity. If this assumption is correct the solution of the model must match with DNS results for the averaged quantities like slip Reynolds number. Figure 4.8 shows that this is indeed true.

From figure 4.9(b) it can also be concluded that, within our parameter range, if all other parameters remain same, the local surface tension force is proportional to void fraction. From figure 4.10(b) it can similarly be concluded that if all other parameter remains

same, the local surface tension force is proportional to $\left(\frac{\beta}{\rho g}\right)^{0.33}$. These observations are

very important since it allows for modeling the local surface tension force with varying void fractions. From figure 4.15 and 4.16 it is clear that flow around multiple bubbles in the vicinity of the wall are almost identically equal to that of a single bubble in periodic domain. This indicates that the effect of bubble interaction is negligible in these flows.

From figure 4.17 it is clear that the results from the wall-layer simulations don't agree identically with the full-channel simulation. The reason for this disagreement is discussed

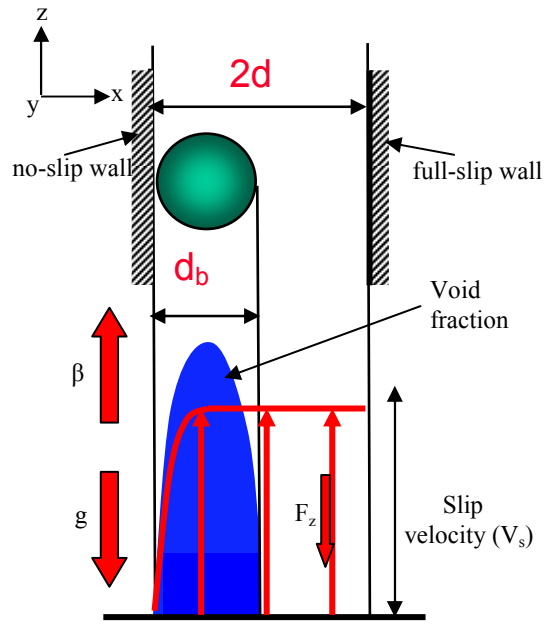
in section 4.6.

The model says nothing about the relative motion of the bubbles with respect to the liquid phase near the wall. From initial observation, it seems the rise velocity of the bubble near the wall is much less than the results for homogeneous flows, such as those provided by Esmaeeli and Tryggvason (1998, 1999) and Bunner and Tryggvason (2002 a, b). The authors hope to report on studies of that problem in a future paper.

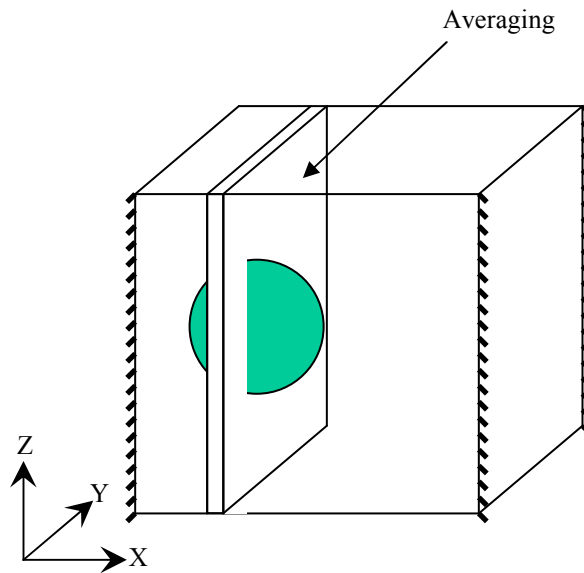
In this study, the flow around a bubble near a vertical fixed wall, have been examined. It has been found that though the bubbles are nearly spherical in the wall layer, they are not completely spherical. It has been observed that this small deformation of the bubbles has a significant effect on the flow field. The dependence of the slip Reynolds number on other non-dimensional numbers governing the flow is also studied using DNS. An averaged model of the flow has been derived by volume averaging the Navier-Stokes equation. Though this model is not closed, the non-closed terms can be estimated by post-processing the results of the DNS simulation. The effect of the governing non-dimensional parameters on these non-closed terms has been studied and some exciting correlations has been found. In real systems, of course, there are several complications. The primary one is the non-uniform size distribution of the bubbles. Currently there are no way of predicting the size distribution of bubbles in the wall layer in a poly-disperse flow. But it is evident that the non-closed terms of the model (local surface tension force) will depend critically on such a size distribution of the bubbles. So if the bubble size distribution changes so will this term and hence the slip Reynolds number. This gives rise to a very interesting question. Whether the steady-state slip Reynolds number and hence flow rate in such complex situations will be inherently unstable? Clearly more

investigations are needed answer these questions.

The results presented here should be helpful for further development of models for multiphase flows. The two-fluid model of Antal et al. (1991) predicts the hydrostatic balance in the core, as was pointed out by Azpitarte and Buscaglia (2003), but the location of the wall-peak is determined in the model by the relative magnitude of the lift force and the wall-repulsion force. The total through flow is sensitive to the thickness of the wall peak and small changes in the lift force can change the results significantly. Lu, Biswas and Tryggvason (2005) found that for homogenous upflow the steady state is independent of the lift force. The bubbles in the wall-layer hug the wall and the wall-peak is always one bubble radius away from the wall. In this study an attempt has been made to understand the dependency of the velocity increase across the wall-layer on the governing parameters. It is, however, important to note that the situation considered here, laminar flow of equal size bubbles, is a limiting case. In practical situations the bubbles are unlikely to be of the same size, they may coalesce and break, they will be contaminated, and the flow is likely to be turbulent. However, in the spirit of the study of Antal et al. (1991), the authors believe that well understood limiting cases must provide the foundation for the modeling of more complex situations.



(a)



(b)

Figure 4.1. (a)The problem setup. Rise of a single bubble near the wall. The width of the channel is $2D$, where D is the bubble diameter. Gravity acts in the negative z direction and the pressure gradient is acts in the positive z direction. The wall is no slip at $x=0$ and full slip at $x=2D$. In the region $x > D$ a body force is added to make the flow hydrostatically balanced. (b) Averaging volume for average equations

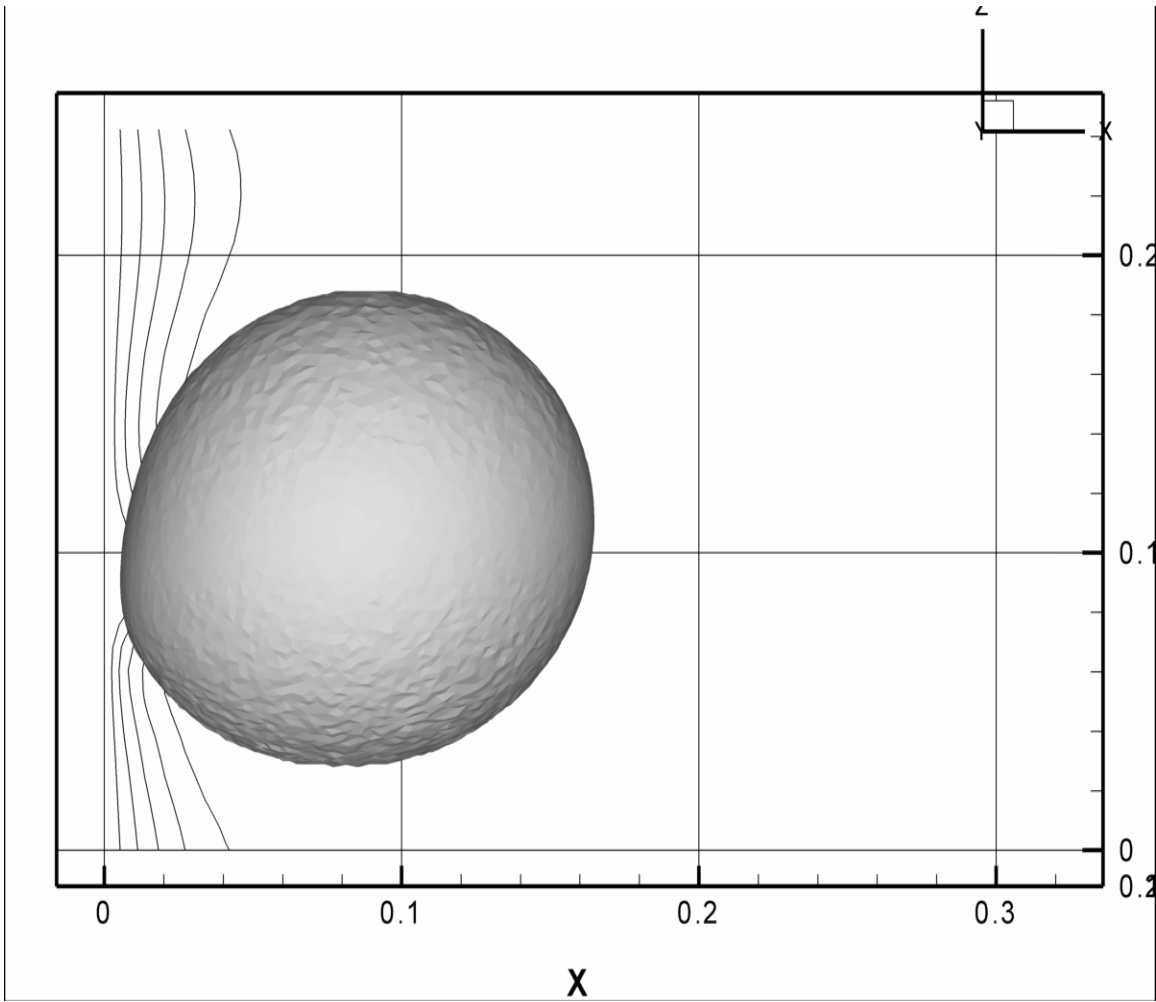
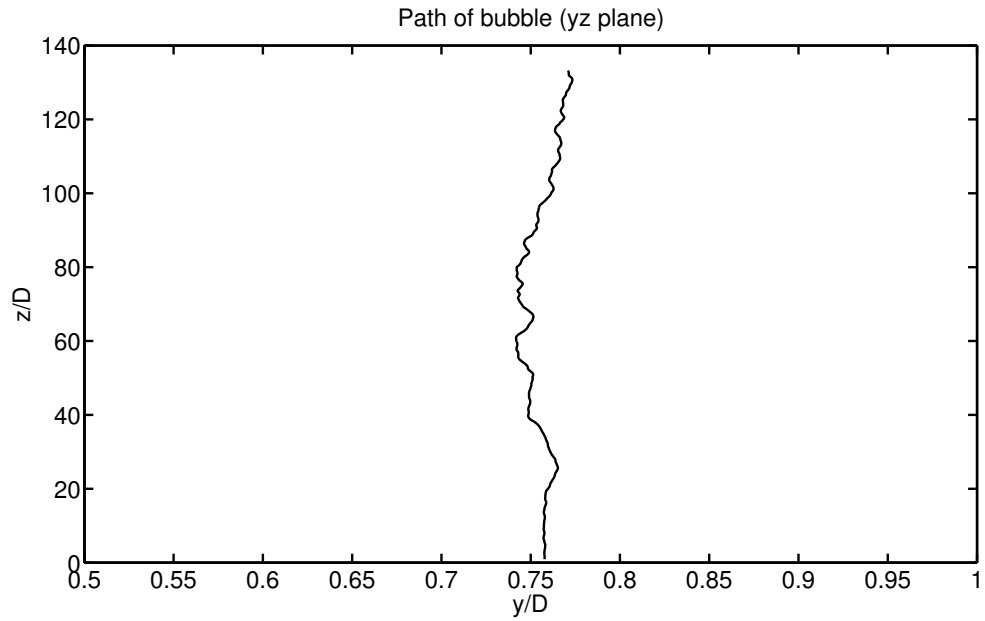
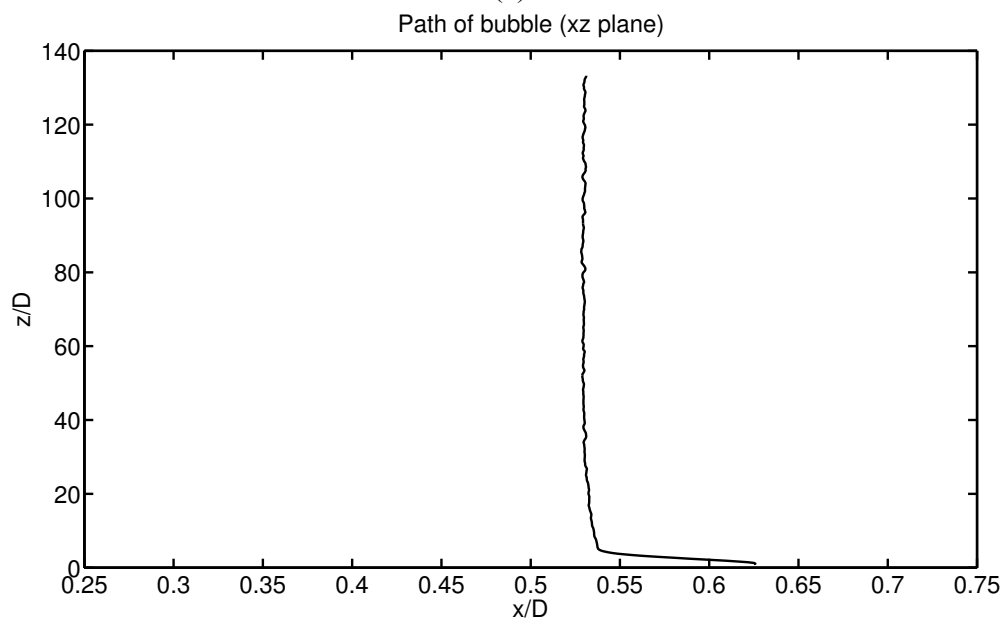


Figure 4.2. Three-dimensional direct simulation of the rise of a single bubble in upflow near the no-slip wall in a vertical channel. The bubble and the iso-contours of vertical velocity in a x - z plane are in a stationary frame of reference at a late time after the flow has reached a steady state.

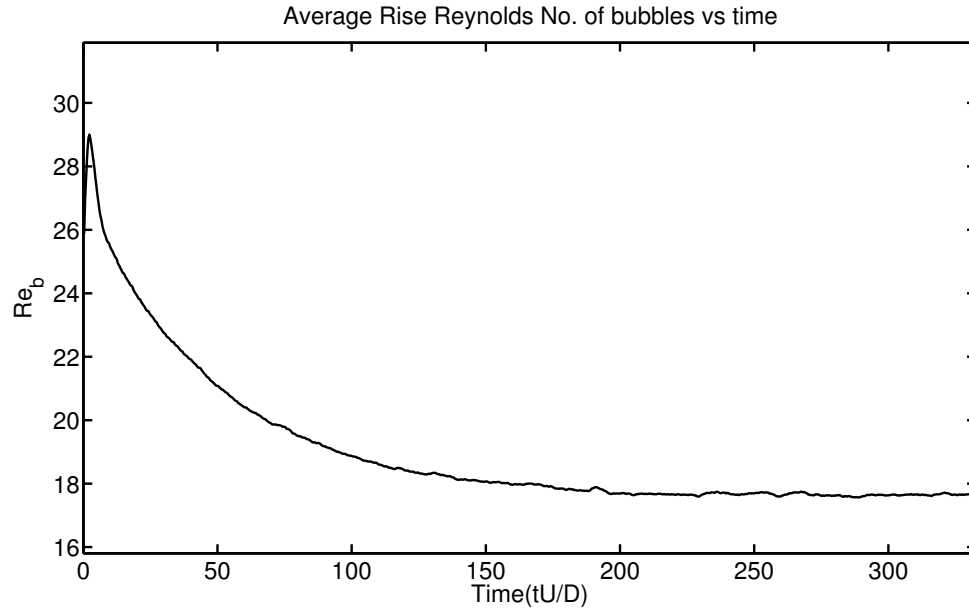


(a)

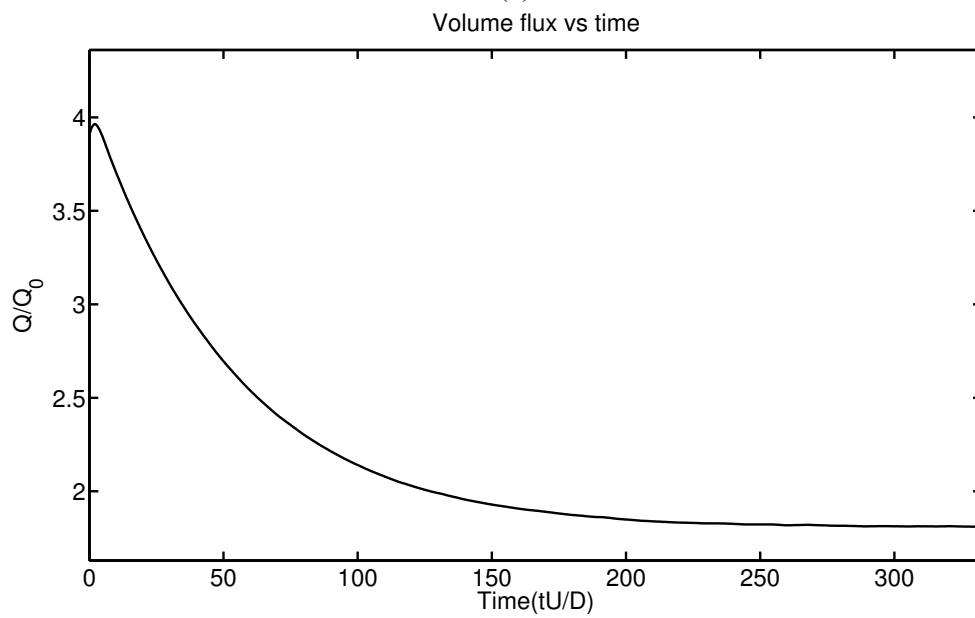


(b)

Figure 4.3. Three-dimensional direct numerical simulation of the rise of a single bubble in upflow in a vertical channel. Path of the bubble is shown in a stationary frame of reference.



(a)



(b)

Figure 4.4 (a) The average velocity of bubbles and (b) the through flow normalized by the channel flow without bubbles.

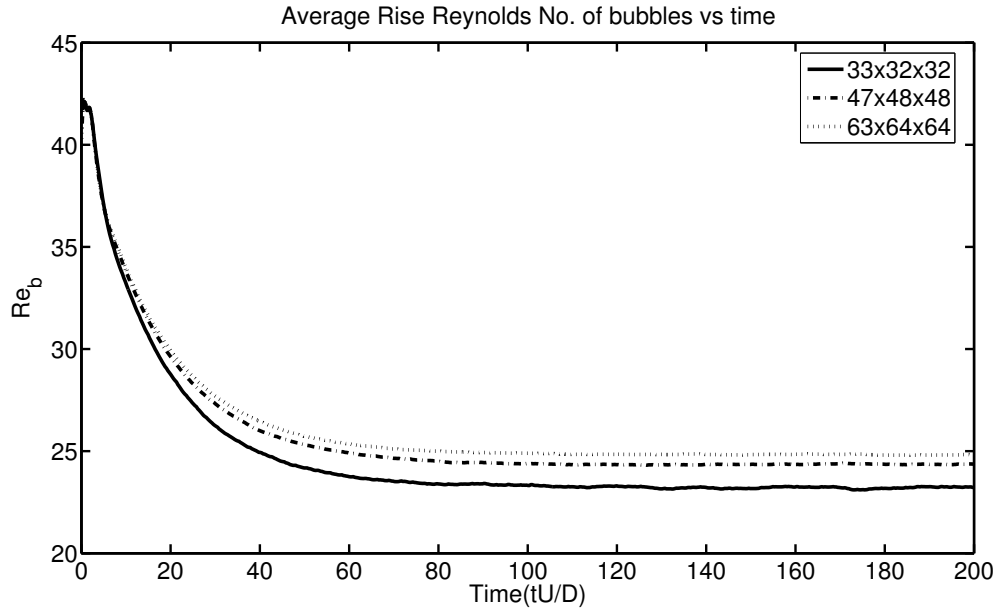


Figure 4.5. Results of the convergence study. The average velocity of bubbles. The density and viscosity ratio is chosen as 1/10 in this case.

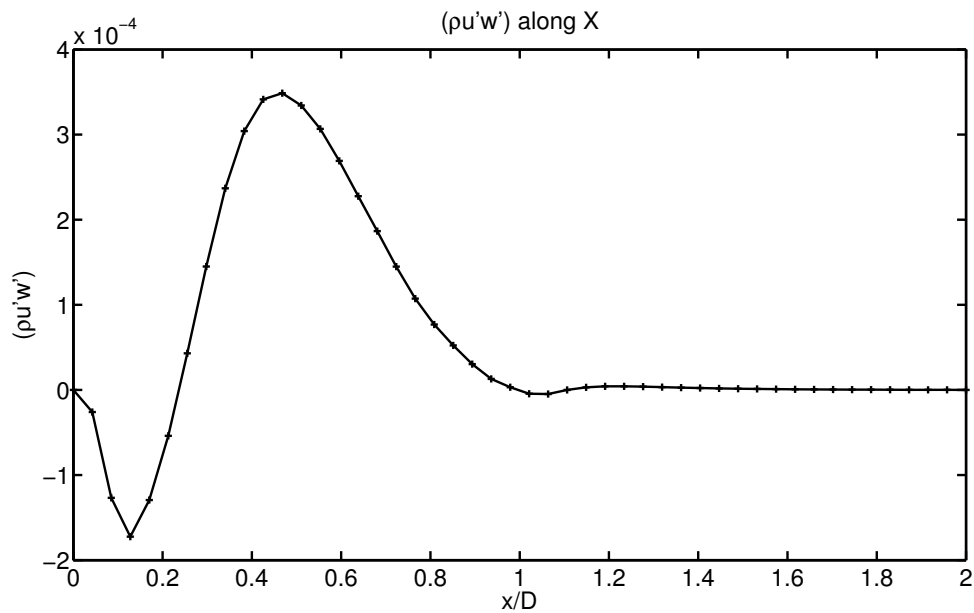


Figure 4.6. The distribution of the Reynolds stresses in x direction.

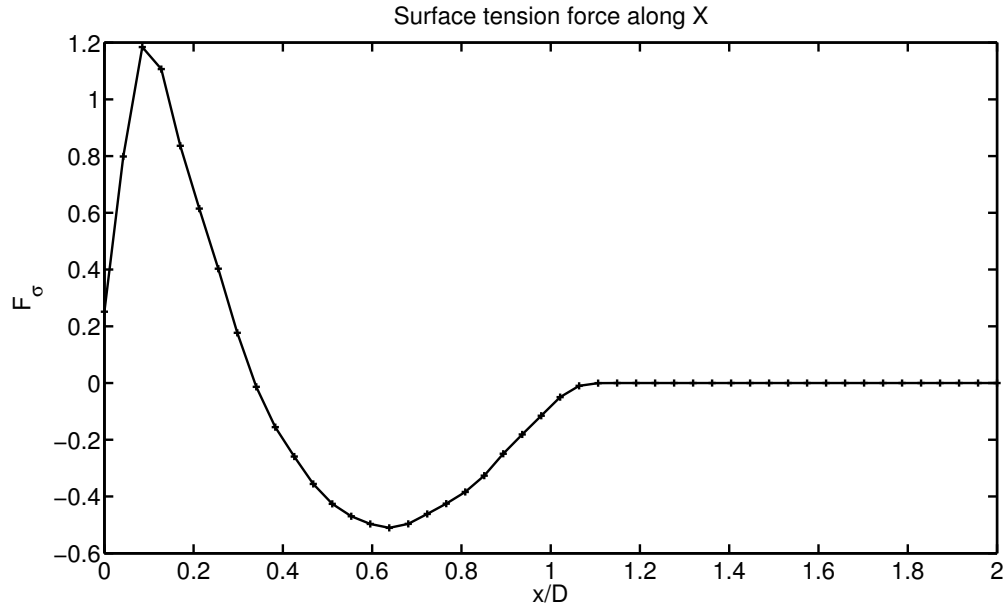


Figure 4.7. Local surface tension force along x direction

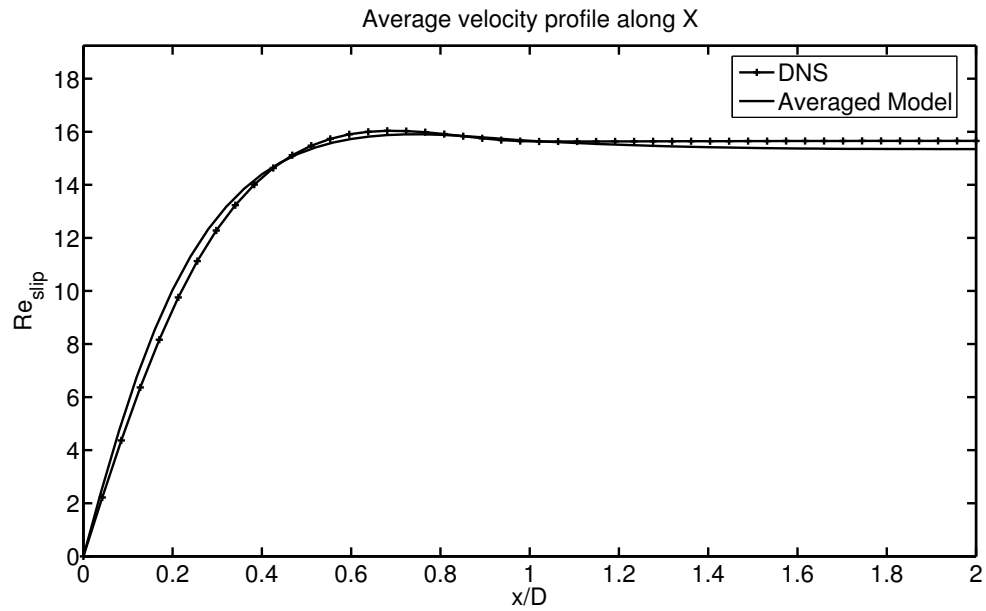
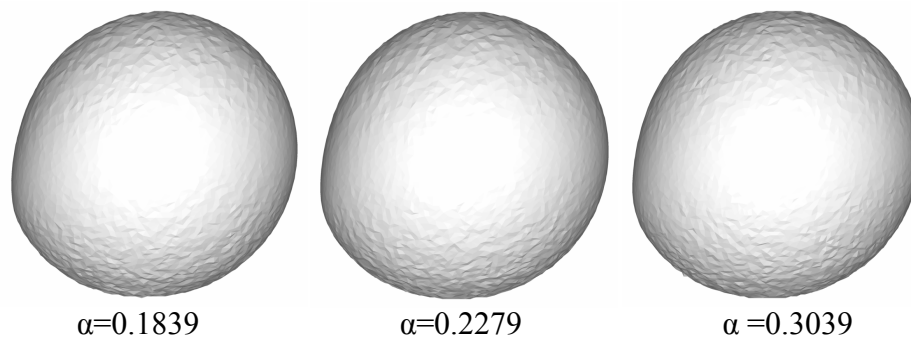


Figure 4.8. Comparison between liquid velocity profile in the wall layer obtained by two fluid model and direct numerical simulation.



$\alpha=0.1839$

$\alpha=0.2279$

$\alpha=0.3039$

(a)

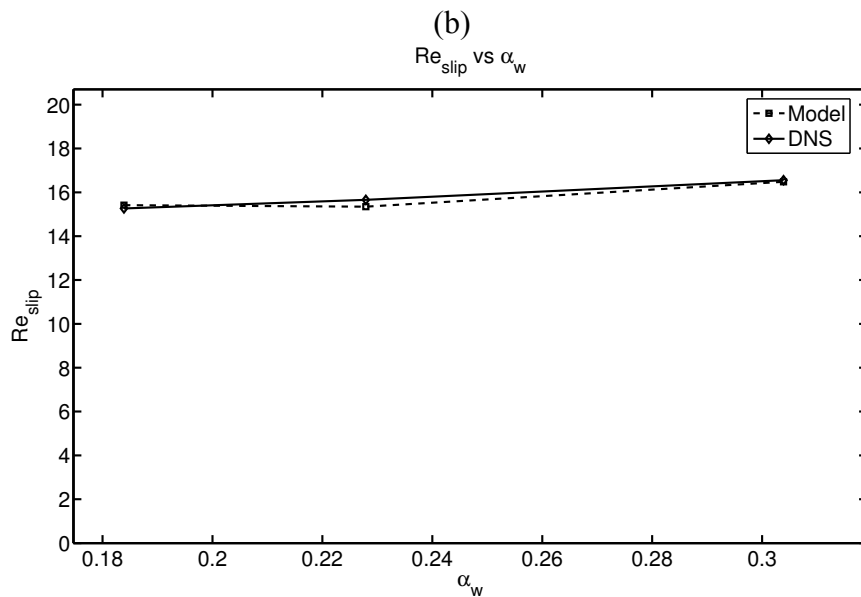
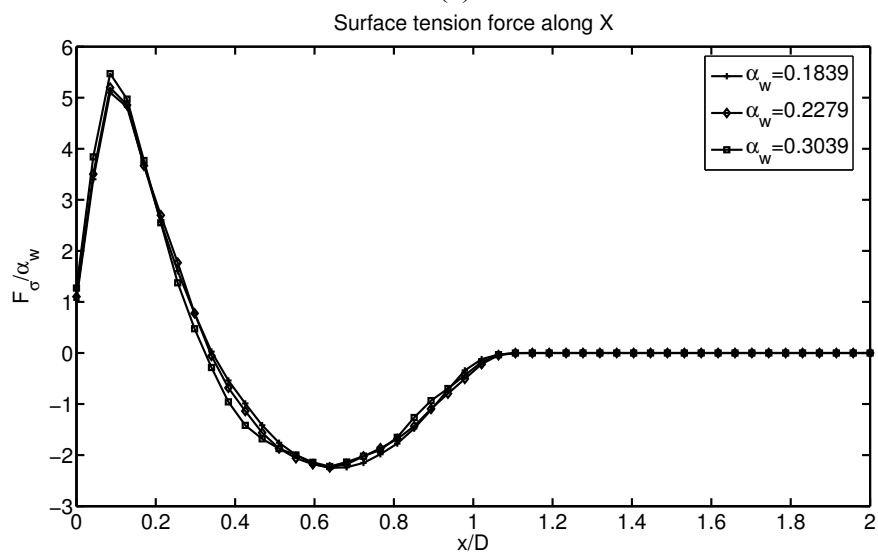
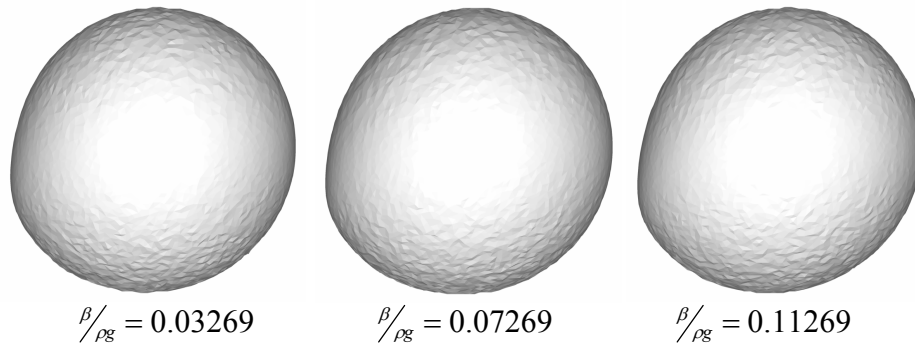
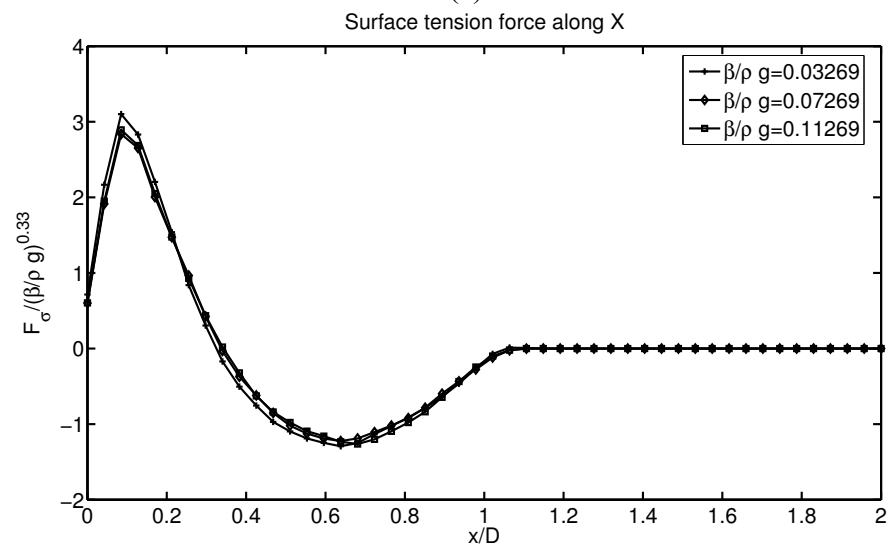


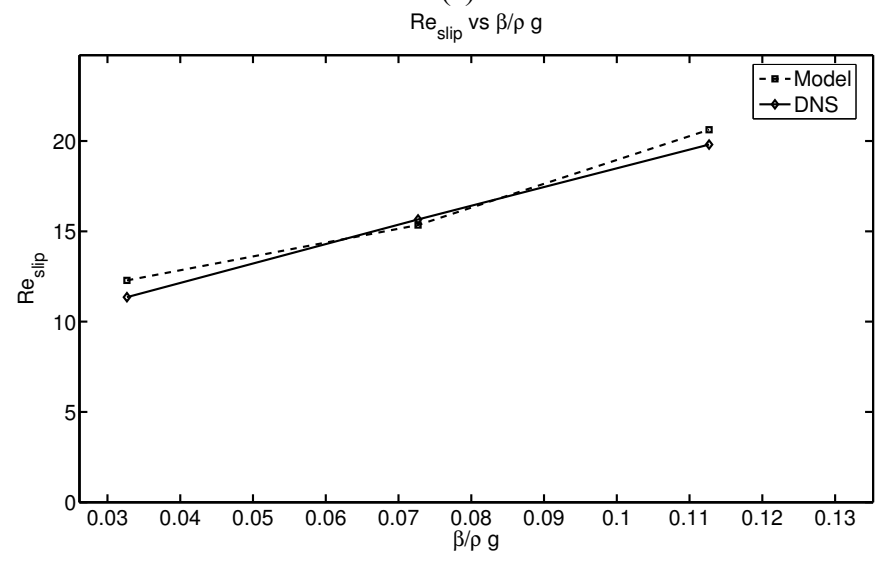
Figure 4.9. Effect of changing the void fraction (α) on the (a) shape of the bubble, (b) local surface tension force, (c) slip Reynolds number



(a)

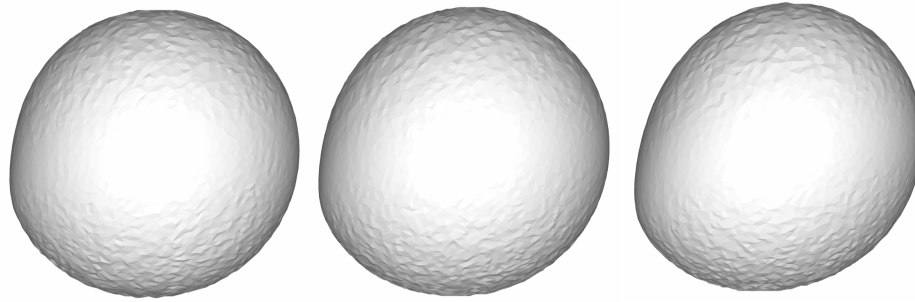


(a)



(b)

Figure 4.10. Effect of changing the pressure gradient ($\frac{\beta}{\rho g}$) on the (a) shape of the bubble, (b) local surface tension force, (c) slip Reynolds number

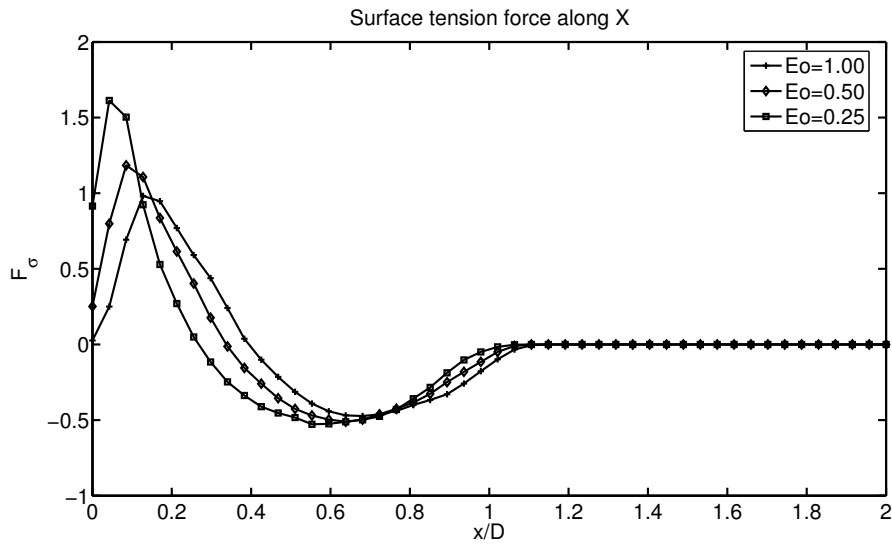


Eo=1.00

Eo=0.50

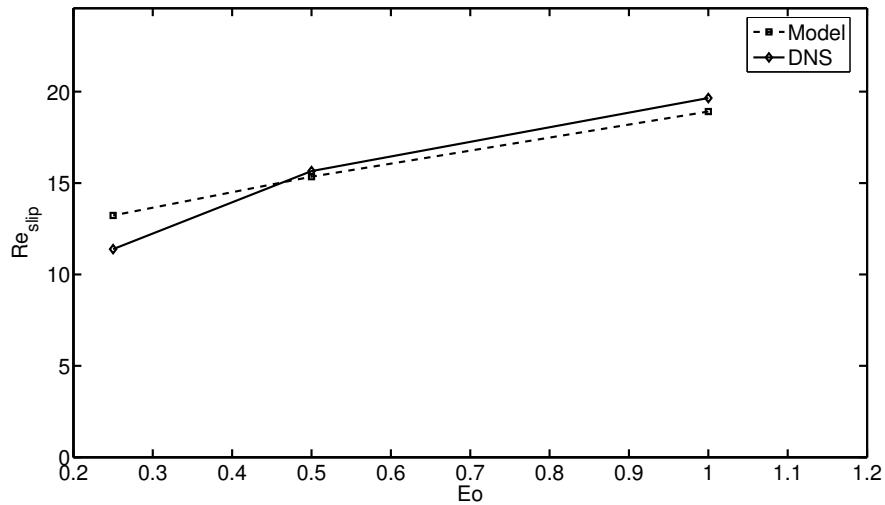
Eo=0.25

(a)



(b)

Re_{slip} vs Eo



(c)

Figure 4.11. Effect of changing the Eötvös No. (Eo) on the (a) shape of the bubble, (b) local surface tension force, (c) slip Reynolds number

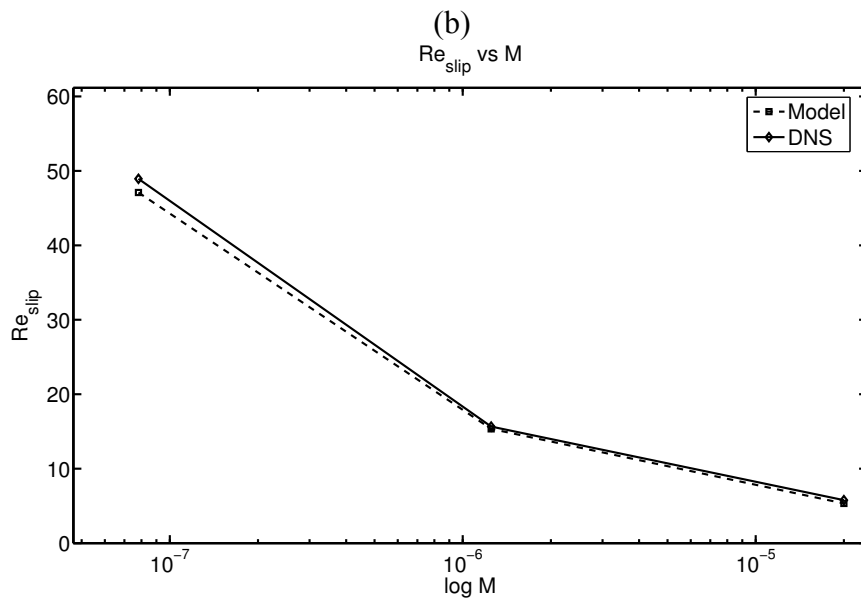
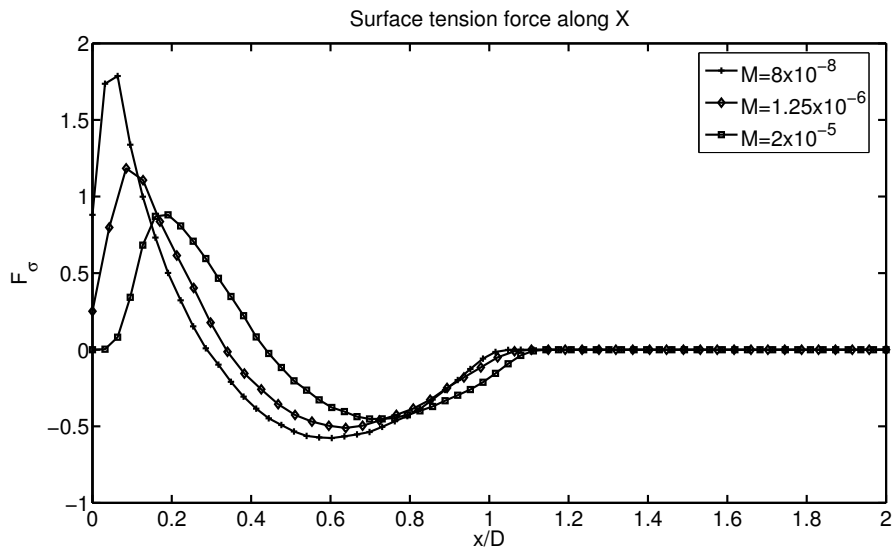
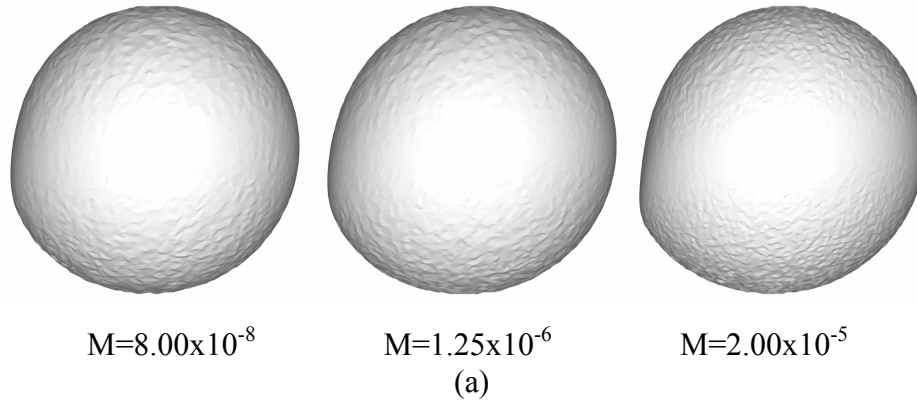
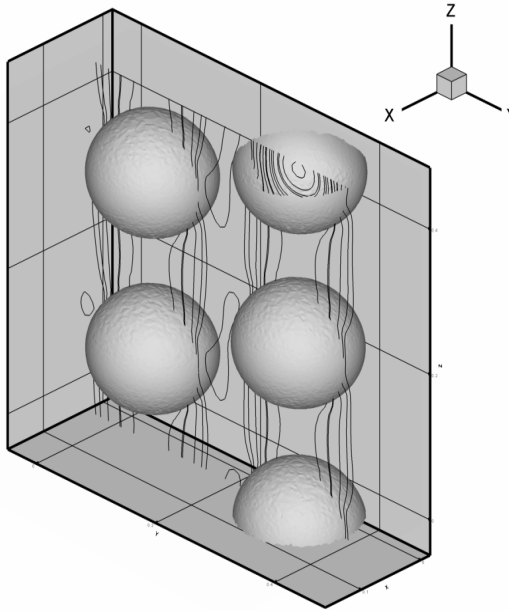
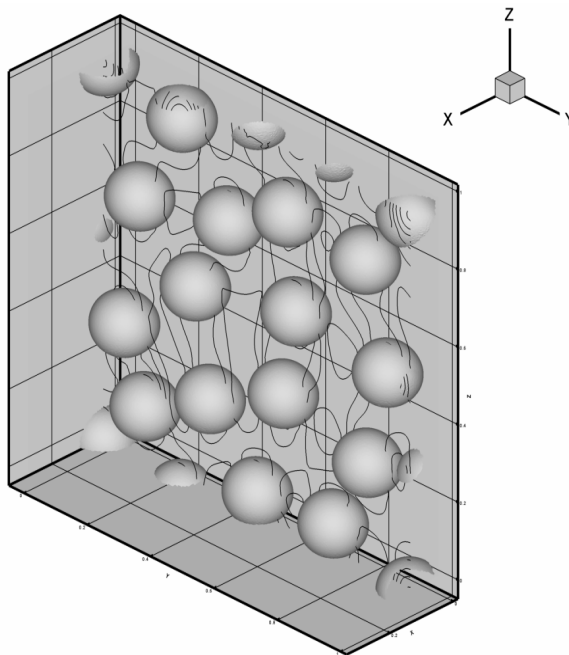


Figure 4.12. Effect of changing the Morton No. (M) on the (a) shape of the bubble, (b) local surface tension force, (c) slip Reynolds number

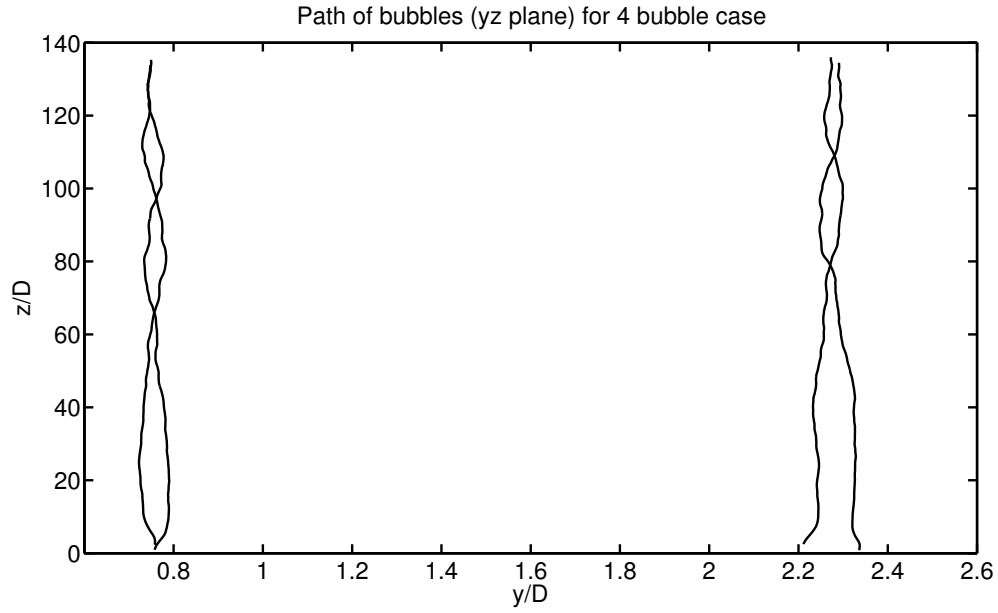


(a) time (tU/D) = 300

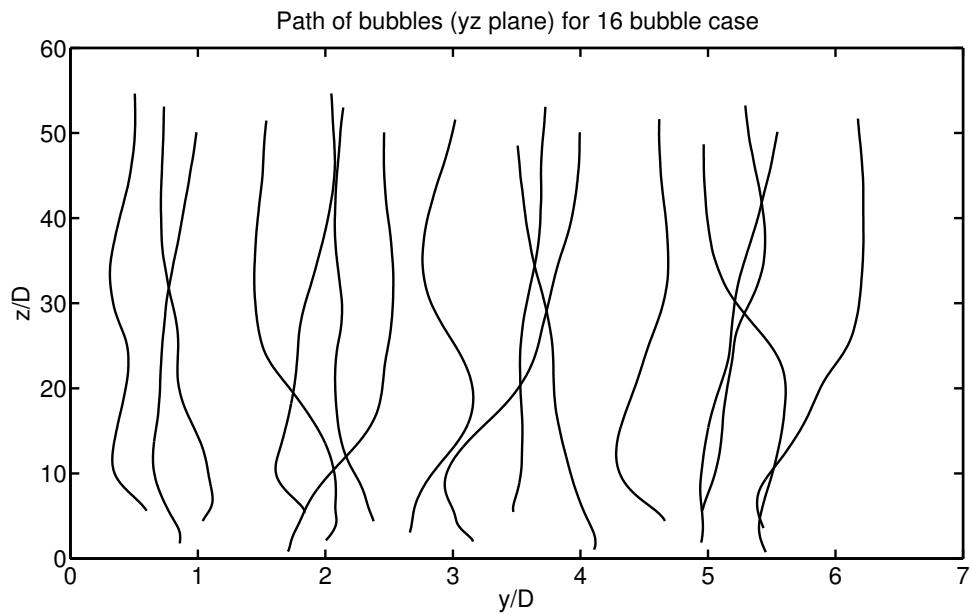


(b) time (tU/D) = 100

Figure 4.13. Three-dimensional direct simulation of the rise of (a) 4 bubbles and (b) 16 bubbles in upflow near the no-slip wall in a vertical channel. The bubbles and the isocontours of the vertical velocity in a plane are shown in a stationary frame of reference at a late time after the flow has reached a steady state.

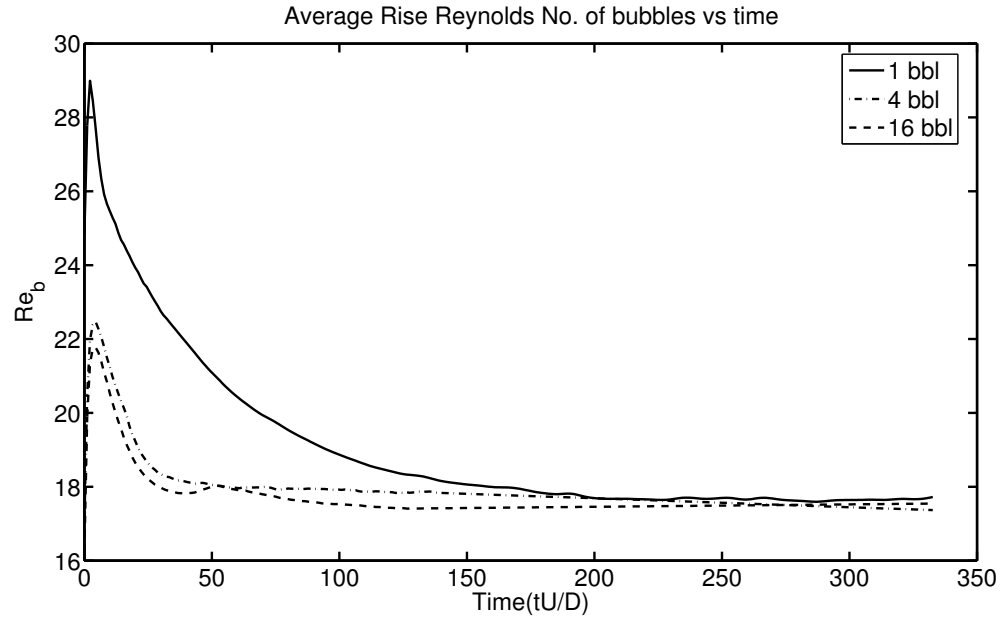


(a)

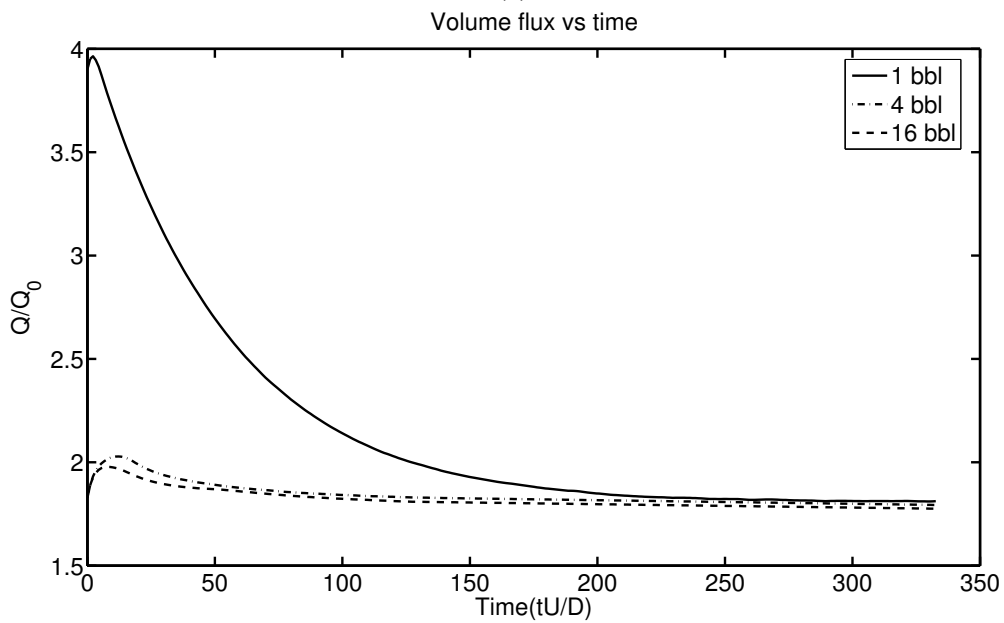


(b)

Figure 4.14. Three-dimensional direct simulation of the rise of (a) four bubbles and (b) sixteen bubbles in upflow in a vertical channel. Path of the bubbles are shown in a stationary frame of reference at a late time after the flow has reached a steady state.



(a)



(b)

Figure 4.15. Comparison between Single, Four, Sixteen bubble Simulations (a) The average velocity of bubbles and (b) the through flow normalized by the channel flow without bubbles.

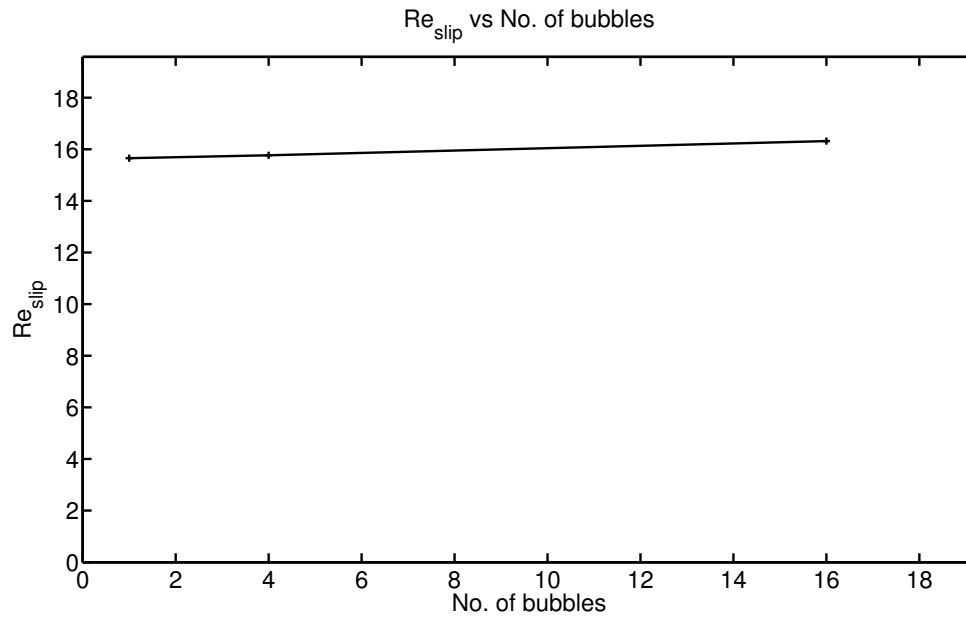


Figure 4.16. Effect of number of bubbles on the slip velocity

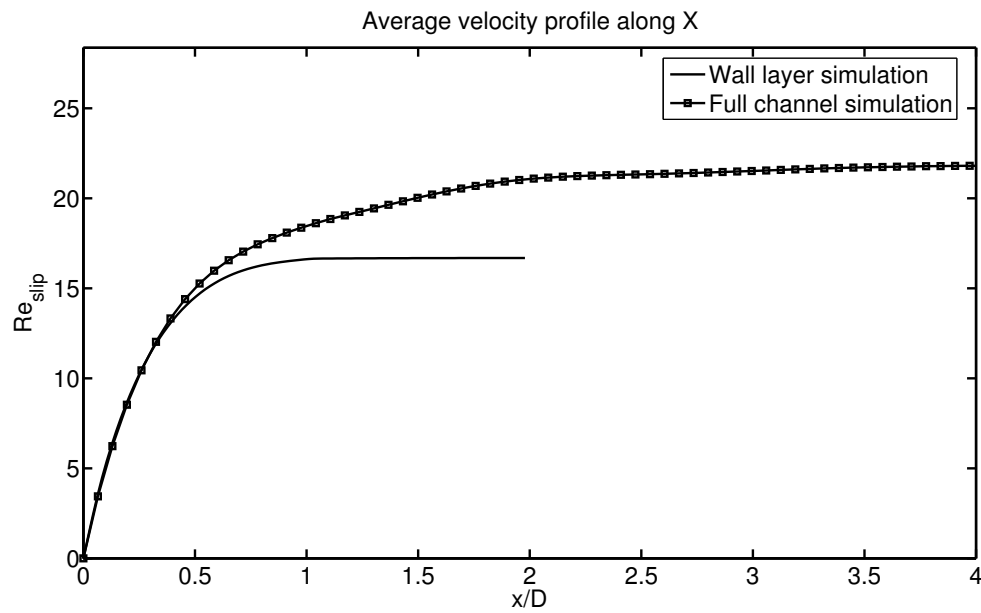


Figure 4.17. Comparison of liquid velocity profile in the wall layer with full wall simulation of J. Lu, S. Biswas, and G. Tryggvason. The simulation in wall layer is done unto two bubble diameters only.

Table 4.1. Parameters for baseline case and convergence study

Case	BASELINE CASE	CONVERGENCE STUDY
Domain size	0.32x0.2425x0.2425	0.21x0.21x0.21
Density of fluids/bubbles	2.5/0.25	2.5/0.25
Viscosity of fluids/bubbles	0.00899746/0.000899746	0.00899746/0.000899746
Pressure gradient	-0.1817	-0.5211
Gravity	1.00	1.00
Diameter of bubbles	0.16	0.16
Surface tension co-efficient	0.128	0.128
Wall void fraction	0.2279	0.3039
Eötvös number	0.50	0.50
Morton Number	2.00×10^{-6}	2.00×10^{-6}

CHAPTER V

Transient buoyancy driven motion of bubbles across a two-dimensional domain

5.1 Introduction

In this study a very simple model problem where a cloud of buoyant bubbles moves across a horizontal channel is examined. To model the evolution of the void fraction profile, first, simulations of homogeneous bubbly flows are performed. Data from these homogeneous bubbly is used to provide a relation for the dependency of the bubble slip velocity on the void fraction. The key questions are how well the model, derived using small bubbles and a dilute flow, performs in situations that are easily simulated (large bubbles and dense flow), and how many ensembles needs to be simulated to get a well converged average flow behavior. To allow for easily computing several cases (with slightly different initial conditions) for a relatively large system, it is assumed that the motion is two-dimensional. Initially the study is limited to only mono-dispersed bubbles and quiescent domain. Afterwards the effect of imposed shear on the system and the effect of poly-disperse bubbles are investigated.

5.2 Mono-dispersed bubbles

5.2.1 Problem setup

The transient migration of bubbles in a horizontal channel is examined, with gravity acting downward, normal to the top and bottom walls. See figure 5.1, where the vertical coordinate is defined as y and the horizontal coordinate is defined as x . The bubbles rise

upwards due to gravity. There is no pressure gradient in either the x or the y direction and the liquid is initially at rest. The flow is assumed to be homogeneous on the average in the x direction ($\partial/\partial x = 0$). Here the study is limited to systems with bubbles of only one size, so the rise of the bubbles is determined by the Morton number, M , and the Eötvös number, Eu . In addition, either the distribution of the bubbles or the void fraction distribution, α , as function of vertical distance, as well as the size of the domain needs to be specified. The governing non-dimensional numbers therefore are:

$$Eu = \frac{\rho_l d_b^2 g}{\sigma}; \quad M = \frac{g \mu_l^4}{\rho_l \sigma^3}; \quad \alpha(y^*); \quad \frac{H}{d_b}$$

Here H is the height of the channel, ρ_l and μ_l are the liquid density and viscosity, respectively, σ is the surface tension, g is the gravity acceleration, and d_b is diameter of the (un-deformed) bubbles. When presenting the results, length is non-dimensionalized by the channel height H , time by $\tau = (\sqrt{H/g})$, kinetic energy by $u^{*2} = (Hg)$, dissipation by $\varepsilon^* = \sqrt{H/g^3}$ and velocities are given as Reynolds numbers $Re = \frac{\rho_l V d_b}{\mu_l}$.

5.2.2 The two-fluid model

The two-fluid model for multiphase flow is based on writing separate conservation equations for mass and momentum for each phase. In the problem studied here, there is no net flow. Hence, the model simplifies considerably. In particular, it is not necessary to consider the momentum equation in the liquid, since the liquid flow is determined completely by the bubble slip velocity. The conservation equation for the void fraction, $\alpha = \alpha_g = 1 - \alpha_l$, is given by

$$\frac{\partial \alpha}{\partial t} + \frac{\partial}{\partial y} (\alpha v_g) = 0 \quad (5.1)$$

where v_g is the gas velocity in the y direction. For the liquid α_g is replaced by α_l and v_g by v_l (the liquid velocity). Adding the conservation equation for the gas and the liquid, the following equation is obtained

$$\frac{\partial}{\partial y} [\alpha v_g + (1 - \alpha)v_l] = 0 \quad (5.2)$$

Using the boundary conditions that the velocity in y direction at the top and bottom walls is zero for both phases,

$$\alpha v_g + (1 - \alpha)v_l = 0 \quad (5.3)$$

The average bubble slip velocity in the y direction is $v_s (= v_g - v_l)$, so

$$v_g = (1 - \alpha)v_s, \quad v_l = -\alpha v_s \quad (5.4)$$

In general the motion of the bubbles is unsteady and even when the bubbles achieve their steady-state slip velocity, there is a short transient before they do so. This transient is, however, often short and it is assumed that on the average the bubble slip velocity can be taken to depend only on the local void fraction (α). Thus, any dependency on the void fraction gradient is ignored as well as any transient adjustment period associated with a change in the local void fraction. Thus, if v_s is known as a function of α , the void fraction can be found as a function of time by solving equation (5.1), using (5.4).

5.2.3 Results

The goal here is to investigate how realistic it is to use data from DNS of relatively simple systems to model the evolution of more complex flows. For finding the unsteady evolution of the average void fraction for the situation sketched in figure 5.1, using equation (5.1), bubble slip velocity is needed as a function of the void fraction. Simulations of homogeneous flows are used in this study to generate that data. In doing

so two assumptions are made: First of all it is assumed that the bubble velocity depends on the void fraction in the same way it does in homogeneous flows and, in particular, that the velocity depends only on the void fraction and not the gradient of the void fraction. It is also assumed that any transient phase of the bubble motion is sufficiently short, compared to the characteristic bubble rise time, so that the instantaneous bubble velocity is well approximated by the steady state velocity at the corresponding local void fraction. Although Esmaeeli and Tryggvason (1999) have reported data for the void fraction dependency of the average slip velocity for homogeneous two-dimensional bubbly flow, the governing parameters selected here are slightly different so the data is regenerated for our situation by following the motion of 25 bubbles in fully periodic domains until they had reached a statistically steady state, for several values of α . $Eo = 0.2813$ and $M = 4.88 \times 10^{-8}$, are chosen and the void fraction was varied by changing the size of the domain. Figure 5.2 shows the average slip velocity of the bubbles versus the void fraction obtained in this way, along with the bubble distribution at one time, for one void fraction.

Once the bubble slip velocity is obtained as a function of the void fraction for homogeneous flows, it can be applied to more complex situations. To study the system sketched in figure 5.1, the motion of 81 bubbles is followed as they rise in an initially quiescent liquid. The diameter of the initially circular bubbles is 0.03 times the height of the domain and Eo and M are the same as used for the data shown in figure 5.2. The width of the domain is equal to its height and periodic boundary conditions are imposed in the horizontal direction. The domain is resolved by a 769 by 768 grid. For computational convenience the bubble density and viscosity are taken to be one tenth of the liquid. As discussed by Esmaeeli and Tryggvason (1999), reducing the density and

viscosity of the bubbles has essentially no impact on the results. Figure 5.3 shows the bubble distribution and the stream lines at different times for one particular simulation. The velocity is initially zero everywhere and the bubbles are located near the bottom wall at the start of the simulation (frame a). The vertical location of the bubbles is determined using a Gaussian distribution of random numbers, but the horizontal location is set “by hand” to ensure that the bubbles do not overlap. As they rise, their motion induces a non-zero velocity in the liquid and the bubbles spread out. A careful examination of the bubble distribution shows that the bubbles in front and back move faster than the bubbles in the middle, leading to an asymmetric distribution of the bubbles. In the front, the fast moving bubbles race ahead, leaving the more crowded bubbles behind, but in the back the fast moving bubbles catch up with the bulk of the bubbles, increasing the local void fraction. Eventually (frame d) the bubbles have spread out sufficiently so that the local void fraction has been reduced essentially everywhere beyond its initial value. Figure 5.4 and 5.5 shows the vorticity contours and velocity field respectively at different times for the same simulation as of figure 5.3. As expected the initial vorticity is zero everywhere. But as time progress strong vorticity can be noticed inside the bubbles and their wakes at early times. Far away from the bubbles the vorticity is relative low. However as the bubbles rise further presence of vorticity can be noticed far way from the bubbles (frame d) indicating presence of large eddies in the flow.

In addition to the case shown in figure 5.3, four other simulations with similar, but slightly different, initial conditions are performed. Although the detailed evolution of each case differed from the others, the overall evolution was similar. In figure 5.6(a) the average bubble rise velocity, versus non-dimensional time for the five realizations is

shown. All cases behave in the same way. The bubbles first accelerate rapidly, overshooting a little (as usually seen for simulations of a homogeneous distribution of bubbles in periodic domains, see Esmaeeli and Tryggvason, 1999). The average bubble velocity then increases gradually, as the average void fraction decreases, until at non-dimensional time 4 or so, when some of the bubbles have hit the top wall. The relatively rapid convergence of the results, when ensemble averaged over a number of run is consistent with the results of Esmaeeli and Tryggvason (1999), where a similarly rapid convergence was found for homogeneous two-dimensional flows. Bunner and Tryggvason (2002) observed similar behavior for fully three-dimensional bubbly flows. In figure 5.6(b) the path of the rising bubbles are plotted for a single case. It can be seen that the overall motion for most of the bubbles is vertical with very little lateral migration.

In Figure 5.7 the void fraction profile obtained by averaging the result from five simulations (solid line) and those from the two-fluid model are plotted. The results are shown at four times, starting with the initial conditions. The model void fraction profile is then evolved solving equation (5.1). To solve the one dimensional advection equation for the void fraction, the domain is discretized using 501 grid points. This is more than enough to give fully converged results for the parameters examined here. As initial conditions a smooth void fraction profile calculated from the ensemble average of the initial conditions for our numerical simulations is used. Since the slip velocity, v_s , as a function of the void fraction, α , is already known, the time evolution of α is calculated by marching in time. To account for the gathering of bubbles at the top wall, the model described by equation (5.1) is modified in such a way that any void fraction flowing

through a point one bubble diameter from the wall is simply allowed to accumulate at the wall.

Since the velocity used to advect the void fraction profile increases with decreasing void fraction, the front part of the profile spreads out but the back side becomes steeper (frame b). The front side continues to spread (frames c and d), until the non-zero void fraction region hits the top wall where the bubbles accumulate (frame d). Although the results in figure 5.7 show that simply making the bubble slip velocity depend on the void fraction captures many aspect of the evolution reasonably well, it is also clear that some aspects are not modeled accurately. This is particularly evident when the maximum void fraction and the shape of the profile in the back are examined carefully. In the back the increase in bubble velocity with the void fraction leads to a “shock”. But in the simulations the sharp change in the void fraction profile is smeared out and the maximum void fraction is reduced. Figure 5.3, where the instantaneous streamlines are plotted, suggests that the reason for the difference is the absence of dispersion in the model. The rising bubbles stir up the liquid and the liquid velocity perturbs the motion of the bubbles. The simplest assumption is therefore that the dispersion of the bubbles is directly related to the turbulent kinetic energy. To model the dispersion, it is necessary to examine the turbulent kinetic energy generated by the passage of the bubbles. In figure 5.8(a) the averaged turbulent kinetic energy versus the vertical coordinate at different times is plotted. It is clear that the intensity of the turbulent kinetic energy increases over time and the stirred region both migrates upwards and spreads. To examine how closely the stirred region follows the location of the bubbles (as figure 5.3 suggests it does,) both the turbulent

kinetic energy and the void fraction at a given time ($t/\tau = 3.0$) versus the vertical coordinate is shown in figure 5.8(b). Obviously, both profiles have a very similar shape.

To check if the turbulent kinetic energy and the void fraction always remain similar, the correlation coefficient between these two is computed.

$$r_{k\alpha} = \frac{\int_A (k - k_{av})(\alpha - \alpha_{av}) dy}{\sqrt{\int_A (k - k_{av})^2 dy} \sqrt{\int_A (\alpha - \alpha_{av})^2 dy}}$$

In figure 5.9 the correlation coefficient versus non-dimensional time is plotted for one particular simulation. Obviously, the kinetic energy and the void fraction profiles are very well correlated. Notice that both the kinetic energy and the void fraction profiles have been normalized by their average values. Thus, the correlation coefficient measures the similarities of their shapes at every given time, but says nothing about how the relative magnitudes may change with time.

The bubble-induced kinetic energy in the liquid is often modeled by assuming that the flow around each bubble is a potential flow. This gives $k \sim \alpha v_s^2$ where v_s is the average slip velocity between the bubbles and the liquid. Since v_s increases with decreasing void fraction, the total kinetic energy will increase as the bubbles disperse. This is easily seen as follows: If v_s is constant in a region of length Δ , then the total kinetic energy is $K_1 = \alpha v_s^2 \Delta$ (taking the proportionality coefficient to be unity). If the bubbles spread out over a length 2Δ , then the void fraction is $\alpha/2$. If the velocity increases by a factor of two (say), then the new total kinetic energy is $K_2 = (\alpha/2)(2v_s)^2(2\Delta) = 4K_1$. In figure 5.10 the total kinetic energy, integrated over the whole domain, is plotted versus non-dimensional time. The kinetic energy increases with time, nearly linearly, until the

bubbles start to accumulate at the top wall (around non-dimensional time 4). By comparing the total kinetic energy at two times, and using the results in figure 5.7 for the average void fraction and the size of the stirred zone, it can be inferred, that the increase is not inconsistent with the estimate given above.

In principle the diffusion coefficient should also depend on the average size of the flow eddies in the stirred region in addition to the turbulent kinetic energy. In turbulence modeling the average dissipation is usually used to indicate the length scales of the velocity fluctuations and since a large eddy (small dissipation) is likely to move the bubbles more than a small eddy (high dissipation), the diffusion coefficient must be inversely proportional to the dissipation. On dimensional grounds

$$D \sim k^2 / \varepsilon .$$

To study the relationship between bubble induced turbulent kinetic energy and dissipation, both the dissipation and the turbulent kinetic energy at a given time ($t/\tau = 3.0$) is plotted versus the vertical coordinate in figure 5.11(a). Obviously, both profiles have a very similar shape.

To check if the dissipation and the turbulent kinetic energy always remain similar, the correlation coefficient,

$$r_{k\varepsilon} = \frac{\int_A (k - k_{av})(\varepsilon - \varepsilon_{av}) dy}{\sqrt{\int_A (k - k_{av})^2 dy} \sqrt{\int_A (\varepsilon - \varepsilon_{av})^2 dy}}$$

is computed. In figure 5.11(b) the correlation coefficient is plotted versus non-dimensional time for one particular simulation. Obviously, the dissipation and the kinetic energy are very well correlated. Both the dissipation and the kinetic energy have been normalized by their average values. Thus, the correlation coefficient measures the

similarities of their shapes at every given time, but says nothing about how the relative magnitudes may change with time. Obviously, from figure 5.11(a) and 5.11(b) it can be concluded that the dissipation is proportional to the kinetic energy. Then the diffusion coefficient will also be proportional to the kinetic energy. Our model therefore becomes

$$\frac{\partial \alpha}{\partial t} + \frac{\partial}{\partial y} (\alpha v_g) = \frac{\partial}{\partial x} \left(D(\alpha, v_g) \frac{\partial \alpha}{\partial y} \right) \quad (5)$$

with

$$D = C \alpha v_r^2 = \frac{C \alpha v_g^2}{(1 - \alpha)^2} \quad (6)$$

Here, C is a dimensional constant and compared the void fraction profile predicted by the model is compared to the simulated results, using several different values for the constant C . In figure 5.12 the comparison for $C=2.0$, at several different times are plotted, in the same way as in figure 5.7. Overall the agreement is much better, showing that even the relatively simple model proposed above captures well what is going on. Since the void fraction profile from the simulations is not smooth (even after averaging it over five different realizations), finding the absolutely best C is not attempted. While the results obviously depend on C , but once the value of C is in the right range, changing C somewhat does not change the agreement in major ways. In figure 5.13 the void fraction at non-dimensional time 4 is shown, along with model results for $C=1, 2$, and 3. The main difference between the model and the DNS results is at the back end of the profile, where the model under predicts the dispersion of the bubbles. This is likely to be a result of ignoring the unsteady fluid motion behind the bubbles. As figure 5.3 shows, there is some unsteady residual motion left below the bubbles but the model relates the fluid turbulence directly to the non-zero void fraction.

5.3 Effect of imposed shear

5.3.1 Problem setup

In this study, the effect of a weak horizontal shear on the system is examined described in 5.2.1. See figure 5.14, where the vertical coordinate is defined as y and the horizontal coordinate is defined as x . The bubbles rise upwards due to gravity but also move with the flow in horizontal direction. The horizontal walls at the top and at the bottom move with different speeds to impose the shear. The flow is assumed to be homogeneous on the average in the x direction ($\partial/\partial x = 0$). This study is limited to systems with bubbles of only one size. So in addition to the Morton number, M , the Eötvös number, Eo , void fraction distribution, α , as function of vertical distance, the size of the domain, the rise of the bubbles is also determined by the non-dimensional shear rate, G^* . In addition, either the distribution of the bubbles or the void fraction distribution also needs to be specified. The governing non-dimensional numbers therefore are:

$$Eo = \frac{\rho_l d_b^2 g}{\sigma}; M = \frac{g \mu_l^4}{\rho_l \sigma^3}; \alpha(y^*); \frac{H}{d_b}; G^* = \frac{\Delta U_{wall}}{\sqrt{gH}}$$

The results are non-dimensionalized in the same way as described in section 5.2.1

5.3.2 Results

To study the effect of imposed shear on the system, one on the cases described in section 5.2 is simulated under two different shear rates. The only difference from the system described in section 5.2 is that the horizontal walls are moving at different speed as shown in figure 5.14. Initially the velocity inside the domain is set such that the velocity increases linearly from the bottom wall to the top wall. Figure 5.15(a) shows the bubble distribution and the stream lines at different times for one particular shear rate. Figure

5.15(b) shows the bubble distribution and the perturbation stream lines (stream lines based on perturbation velocity) for the same simulation. Similar to the results in the quiescent domain, the bubbles spread out as they rise. Similarly, a careful examination of the bubble distribution shows that the bubbles in front and back move faster than the bubbles in the middle, leading to an asymmetric distribution of the bubbles. In the front, the fast moving bubbles race ahead, leaving the more crowded bubbles behind, but in the back the fast moving bubbles catch up with the bulk of the bubbles, increasing the local void fraction. Eventually (frame d) the local void fraction has been reduced nearly everywhere beyond its initial value. This behavior is essentially identical to what has been observed for quiescent domain. Figure 5.16(a) shows the void fraction distribution in the vertical direction for different shear rates at a late time. It can be seen that the void fraction distribution is essentially same, on the average, for different shear rates. To verify whether this is true at all times, the correlation coefficient of void fractions between quiescent system and the system with shear is computed as,

$$r_{G\alpha} = \frac{\int_A (\alpha_G - \alpha_{G_{av}})(\alpha_0 - \alpha_{0_{av}})dy}{\sqrt{\int_A (\alpha_G - \alpha_{G_{av}})^2 dy} \sqrt{\int_A (\alpha_0 - \alpha_{0_{av}})^2 dy}}$$

Figure 5.16(b) shows the void fraction distribution for the quiescent system and system with imposed shear are very well correlated. Similarly, figure 5.17(a) shows the perturbation kinetic energy distribution in the vertical direction for different shear rates at a late time. It can be seen that the perturbation kinetic energy distribution is also essentially the same, for different shear rates. To verify whether this is true at all times, the correlation coefficient of perturbation kinetic energy between quiescent system and the system with shear is computed as

$$r_{G\kappa} = \frac{\int_A (\kappa_G - \kappa_{G_{av}})(\kappa_0 - \kappa_{0_{av}})dy}{\sqrt{\int_A (\kappa_G - \kappa_{G_{av}})^2 dy} \sqrt{\int_A (\kappa_0 - \kappa_{0_{av}})^2 dy}}$$

Figure 5.17(b) shows that the perturbation kinetic energy distribution for the quiescent system and system with imposed shear are very well correlated. Figure 5.18(a) shows the perturbation dissipation distribution in the vertical direction for different shear rates at a late time. It can be seen that the perturbation dissipation distribution is also essentially the same, for different shear rates. To verify whether this is true at all times, the correlation coefficient of perturbation dissipation between quiescent system and the system with shear is computed as

$$r_{G\varepsilon} = \frac{\int_A (\varepsilon_G - \varepsilon_{G_{av}})(\varepsilon_0 - \varepsilon_{0_{av}})dy}{\sqrt{\int_A (\varepsilon_G - \varepsilon_{G_{av}})^2 dy} \sqrt{\int_A (\varepsilon_0 - \varepsilon_{0_{av}})^2 dy}}$$

As expected, figure 5.18(b) shows the perturbation dissipation distribution for the quiescent system and system with imposed shear are very well correlated.

5.4 Effect of poly-disperse bubbles

In this study, the effect of different bubble sizes on the system described in 5.2 is examined. The only difference with the system described in section 5.2 is the bubble sizes are not identical. The bubbles present in the system can be divided in finite number of different size groups. The flow is assumed to be homogeneous on the average in the x direction ($\partial/\partial x = 0$). Initially the velocity is zero everywhere in the domain.

To study such a system, the motion of 60 bubbles as they rise in an initially quiescent liquid is followed. The bubbles can be divided in three different size groups – 25 large bubbles, 25 medium-sized bubbles and 20 small bubbles. All the bubbles are initially circular. The diameters of large, medium-sized and small bubbles are 0.03, 0.035 and

0.04 times the height of the domain respectively. The width of the domain is equal to its height and periodic boundary conditions are imposed in the horizontal direction. The domain is resolved by a 769 by 768 grid. For computational convenience the bubble density and viscosity are taken to be one tenth of the liquid. Detailed parameters for this simulation are given in table 5.1.

Figure 5.19 shows the bubble distribution and the stream lines at different times. The velocity is initially zero everywhere and the bubbles are located near the bottom wall at the start of the simulation (frame a). The vertical location of the bubbles is determined using a Gaussian distribution of random numbers, but the horizontal location is set “by hand” to ensure that the bubbles do not overlap. As they rise, their motion induces a non-zero velocity in the liquid and the bubbles spread out. A careful examination of the bubble distribution shows that the bubbles in front and back move faster than the bubbles in the middle, similar to what is observed in the mono-dispersed case. But larger bubbles also rise faster than smaller bubbles. Figure 5.19 shows the average slip velocity for different bubble sizes with time. The large bubbles ($d_b=0.16$) rise faster than other bubbles until they start hitting the top wall and slow down. Initially the medium-sized bubbles ($d_b=0.14$) rise slower than the small bubbles ($d_b=0.12$). After non-dimensional time 3.0 the medium-sized bubbles catch up and rise faster than the small bubbles. Eventually the medium-sized bubbles start slowing down after reaching the top wall. Figure 5.21 shows the percentage number density of similar sized bubbles along the vertical direction at different times. This percentage is calculated by calculating the number density of similar sized bubbles in 8 equally spaced bins along the vertical direction. Initially ($t/\tau=0.0$) (figure 5.21(a)) all the bubbles are clustered near the bottom

and have approximately same distribution along the vertical direction. At $t/\tau=3.0$ (figure 5.21(b)), it is clear that, the large bubbles ($d_b=0.16$) have risen faster and some of them have already hit the top wall while the medium-sized ($d_b=0.14$) and the smallest bubbles ($d_b=0.12$) lag behind. At $t/\tau=6.0$ (figure 5.21(c)), as expected, number density of large bubbles is more near the top wall than the medium-sized and small bubbles. But between medium-sized and small bubbles, it is difficult to identify which ones are rising faster. At $t/\tau=9.0$ (figure 5.21(d)), most of the large bubbles have reached the top wall. Finally, it is also clear that more medium-sized bubbles have reached the top wall than the smallest bubbles.

5.5 Summary

Although the simulations presented here have been confined to two-dimensional systems, it is shown, that data obtained from homogeneous systems can be used in more complex situations, at least as a first approximation. The inclusion of a void fraction dependent rise velocity in the void fraction advection equation was sufficient to capture the spreading out of the bubbles in the front (where the void fraction is decreasing in the flow direction) and the clumping in the back (where void fraction is increasing). The simulations did, however, also show that the dispersion of the bubbles due to the unsteady flow generated by the bubbles must be included. Here a phenomenological approach is followed and a gradient type dispersion is assumed, directly linked to the pseudo-turbulence induced by the bubble motion. The results showed that the kinetic energy of the liquid and dissipation was well predicted by the void fraction distribution, suggesting that traditional modeling assumptions for the pseudo-turbulence hold reasonably well, at least for the parameters used here. Therefore the dispersion can be

related to the void fraction. This did, however, require an adjustable constant that is unlikely to be universal and the exact dependency of the dispersion on the void fraction distribution and the physical properties of the system (the Morton and Eötvös numbers) remains a topic for future investigation. A simple gradient diffusion model for the void fraction, with a diffusion coefficient proportional to the kinetic energy, allowed us to bring the model results and the DNS results into reasonable agreement. It has been also found that under mild imposed shear, the behavior of the system essentially remains identical. The data shows that the void fraction distribution, kinetic energy of the liquid and the dissipation is extremely well correlated between the quiescent system and the system under imposed shear. For poly-dispersed system it has been found that generally the larger bubbles rise faster than smaller bubbles and eventually this effect dominates. But if the size difference is not big enough, smaller bubbles can also rise faster than slightly larger bubbles initially. Modeling of such systems is beyond the scope of this present work and can be pursued in future studies.

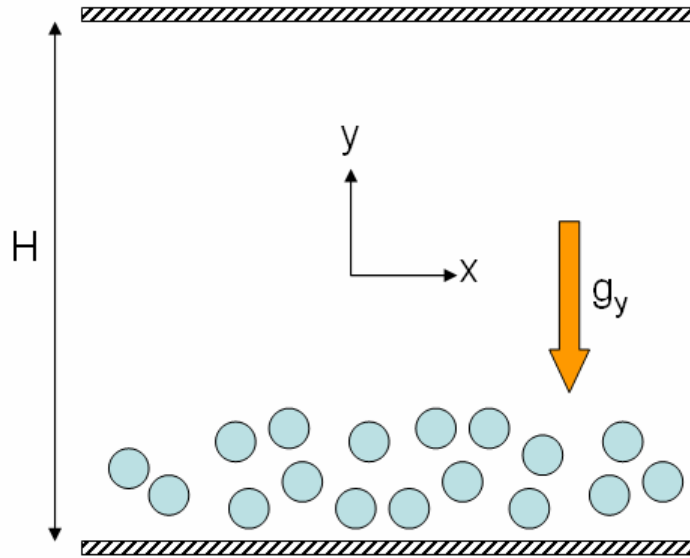


Figure 5.1. The problem setup. The horizontal channel is bounded by walls in the y -direction and is periodic in the x -direction. The height of the channel is H and gravity acts in the negative y direction. The bubbles are released from near the bottom of the channel and rises upwards until they hit the top wall.

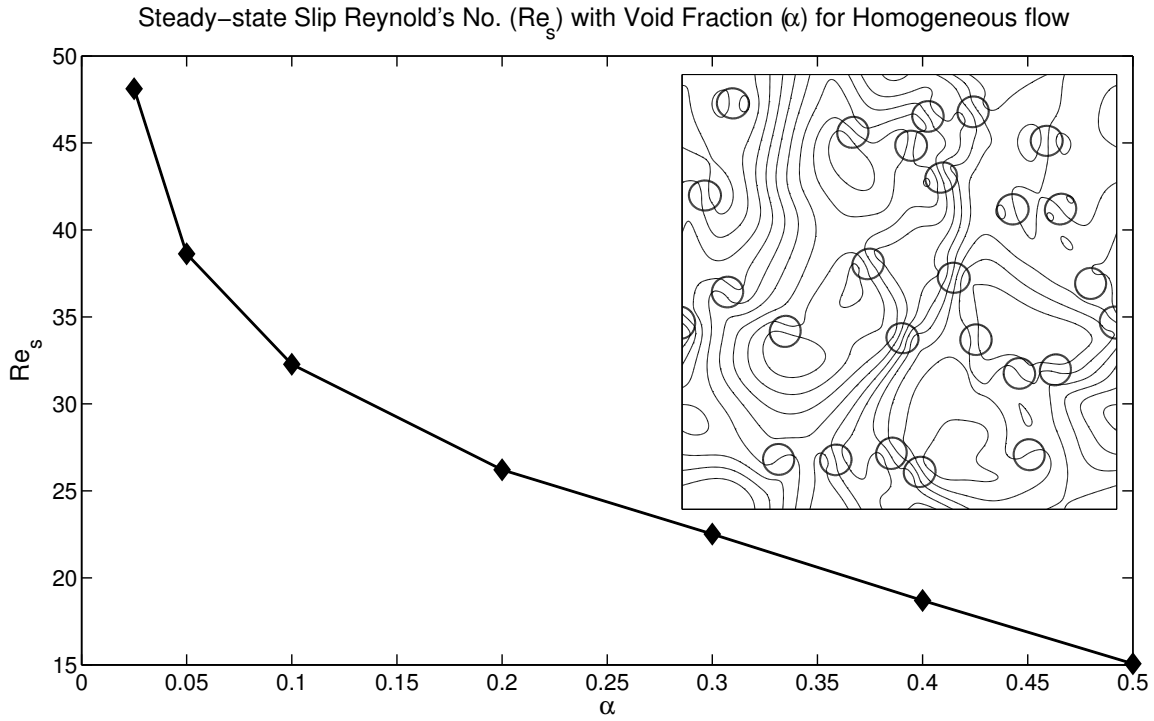


Figure 5.2. The steady-state slip Reynolds number for bubbles in homogeneous flow versus the void fraction. The results are obtained by numerical simulations of the motion of 25 bubbles in a fully periodic domain. One frame, showing the bubble distribution at one time is inserted.

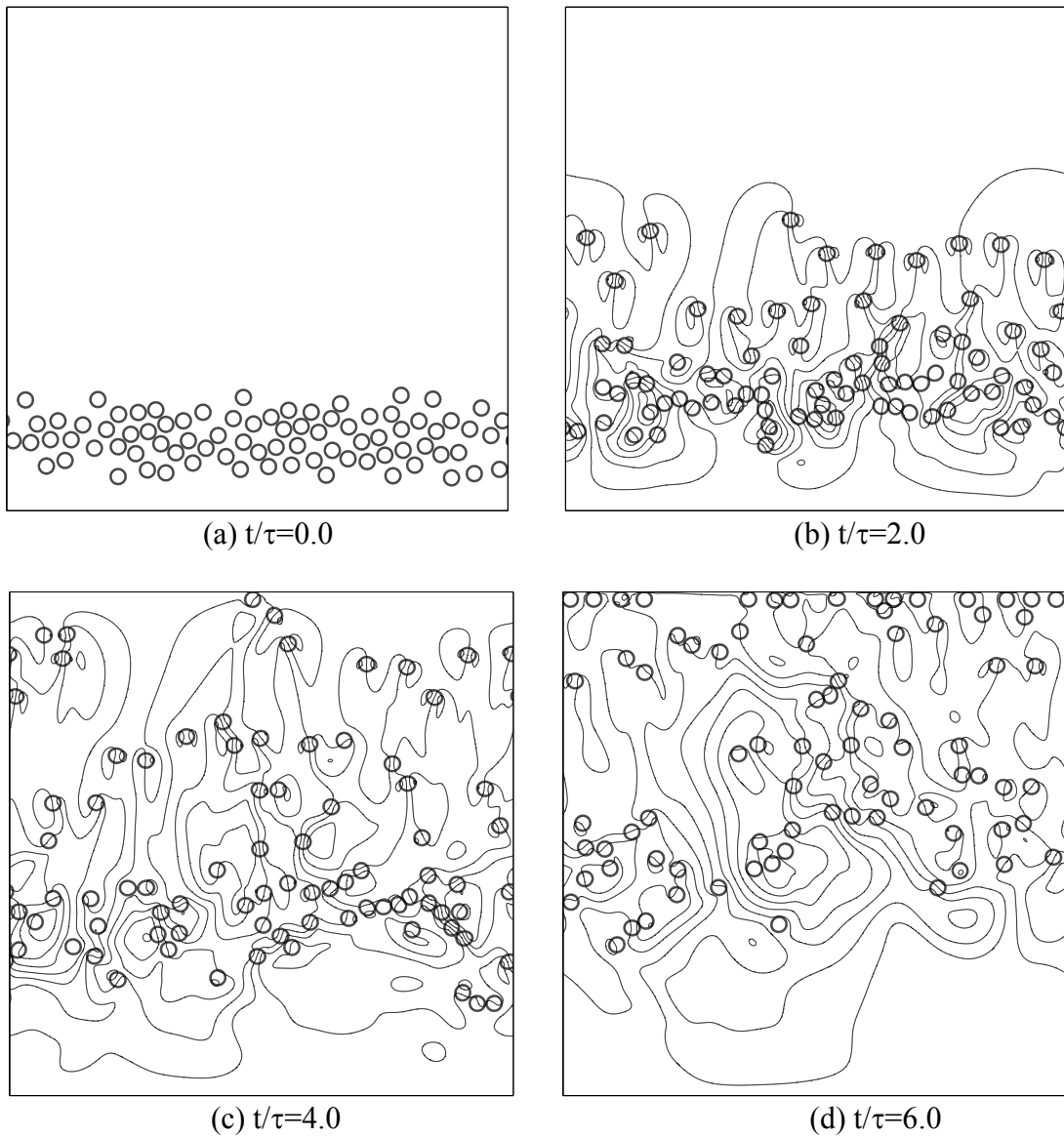


Figure 5.3. Simulations of the rise of bubbles in a horizontal channel. The bubbles and the streamlines in a stationary frame of reference are shown at four different times, starting with the initial conditions. In the last frame, some of the bubbles have hit the top wall.

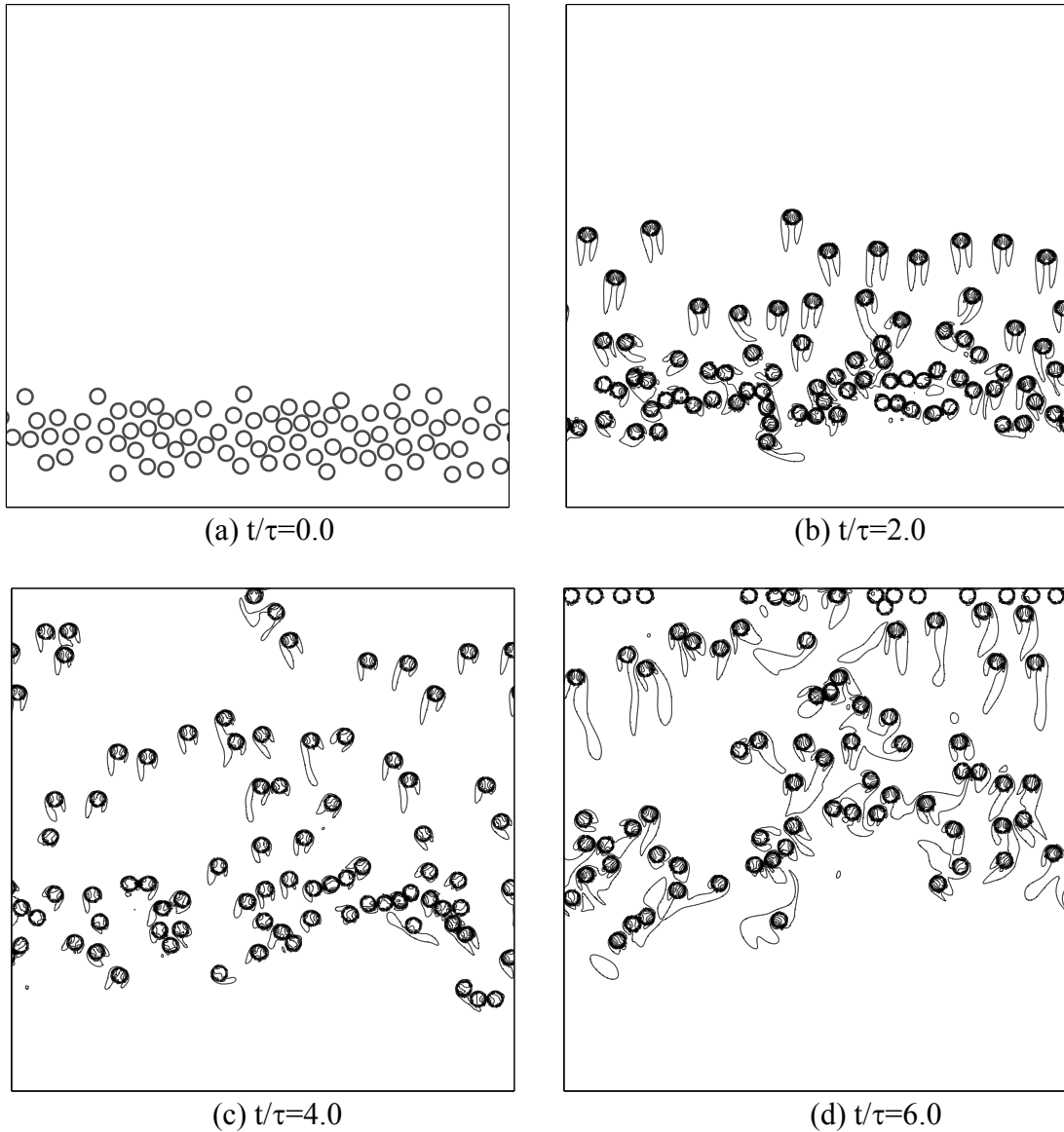


Figure 5.4. Simulations of the rise of bubbles in a horizontal channel. The bubbles and the vorticity contours in a stationary frame of reference are shown at four different times, starting with the initial conditions. In the last frame, some of the bubbles have hit the top wall.

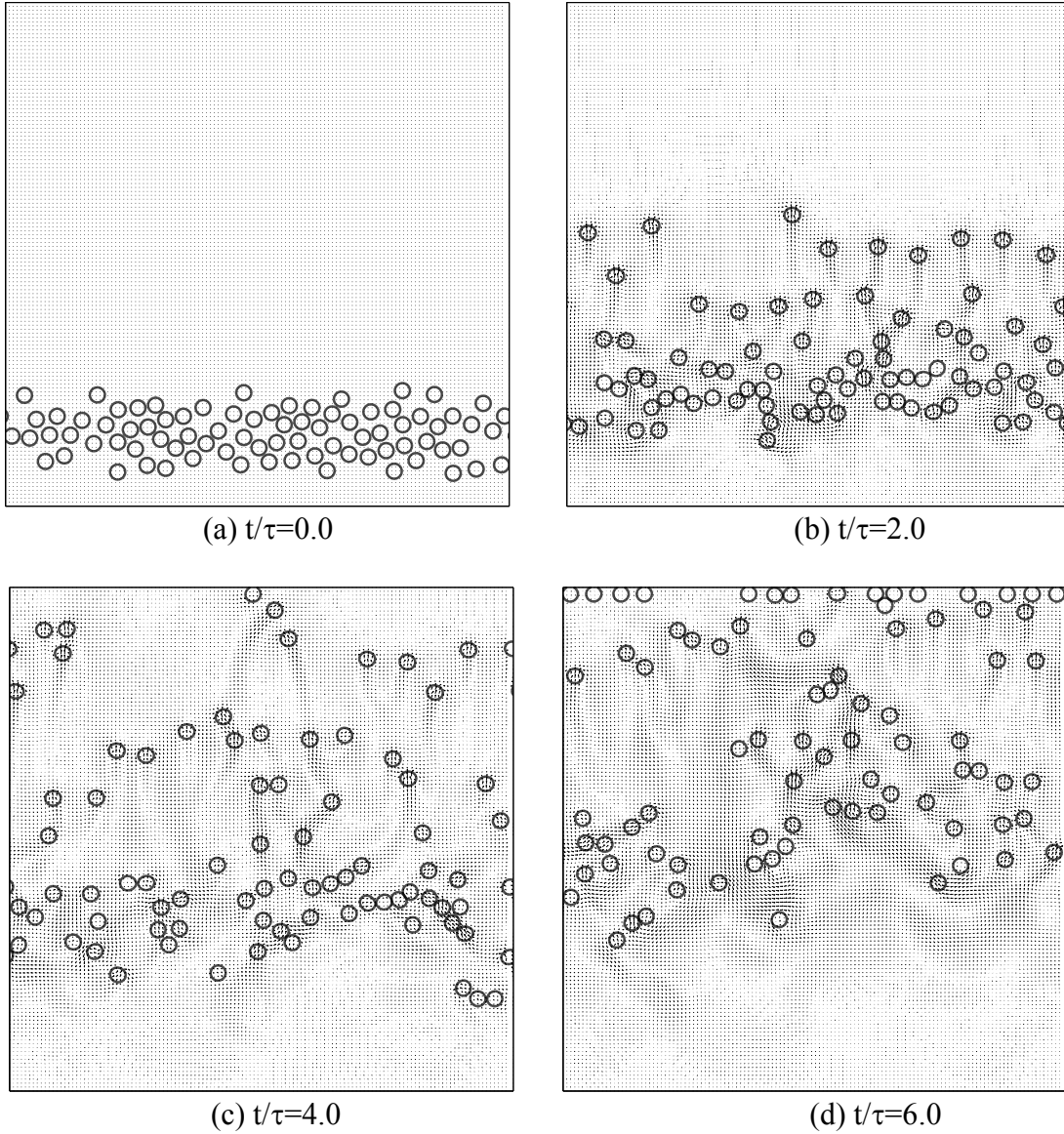
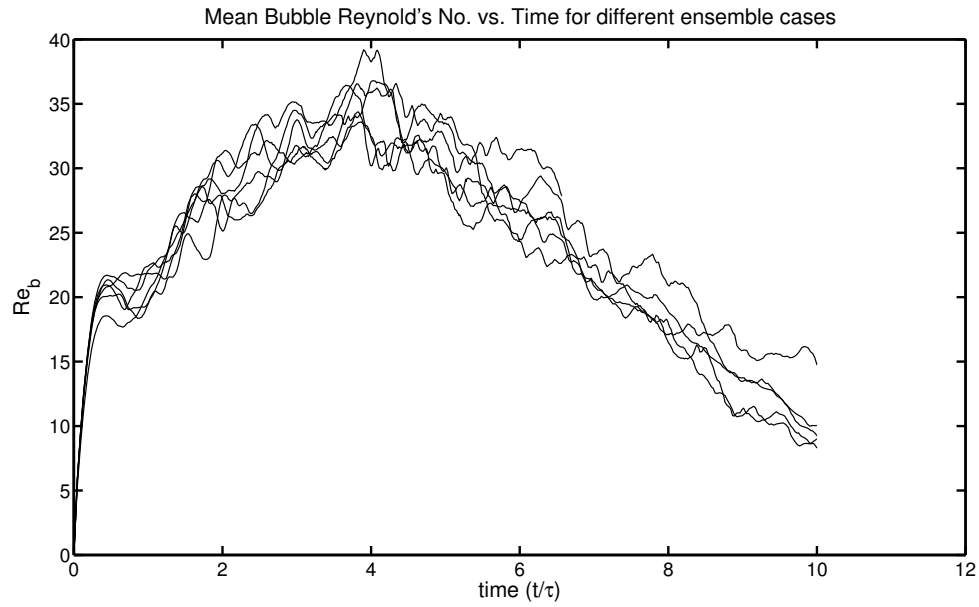
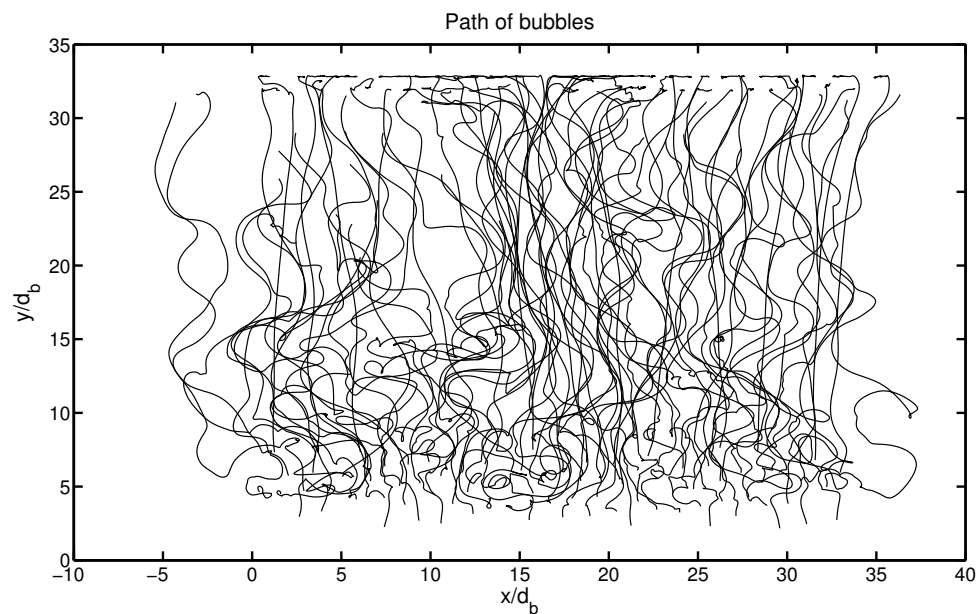


Figure 5.5. Simulations of the rise of bubbles in a horizontal channel. The bubbles and the velocity field in a stationary frame of reference are shown at four different times, starting with the initial conditions. In the last frame, some of the bubbles have hit the top wall.

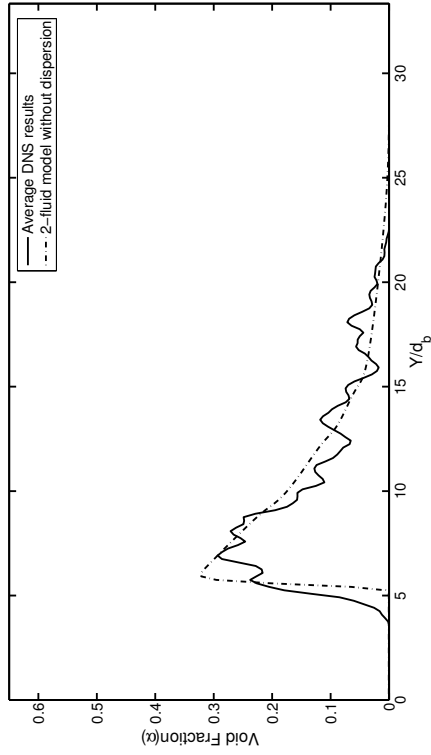


(a)

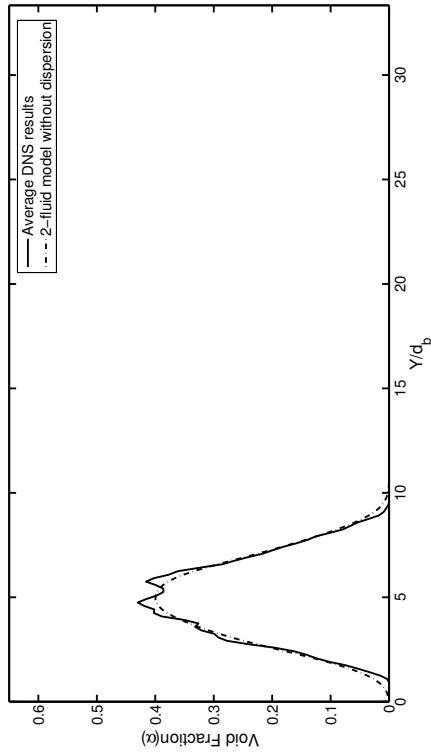


(b)

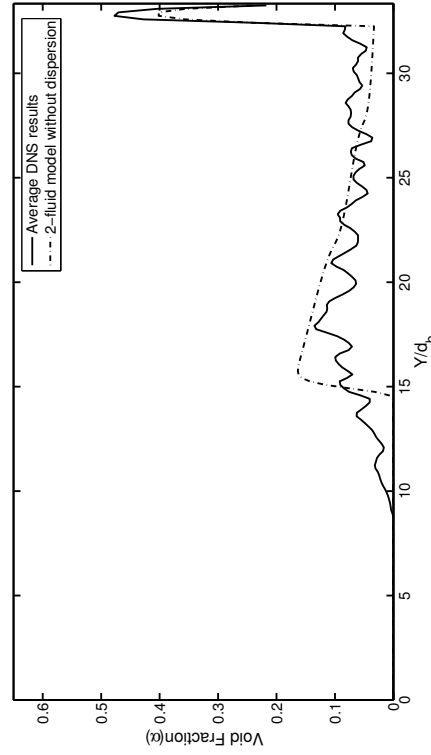
Figure 5.6. (a) The average bubble rise Reynolds number versus time for five different initial conditions. Initially the bubble velocity increases as the bubbles spread out and the void fraction decreases. After about time 4, some of the bubbles have hit the top wall and the average velocity decreases. (b) Path of the bubbles for a single case.



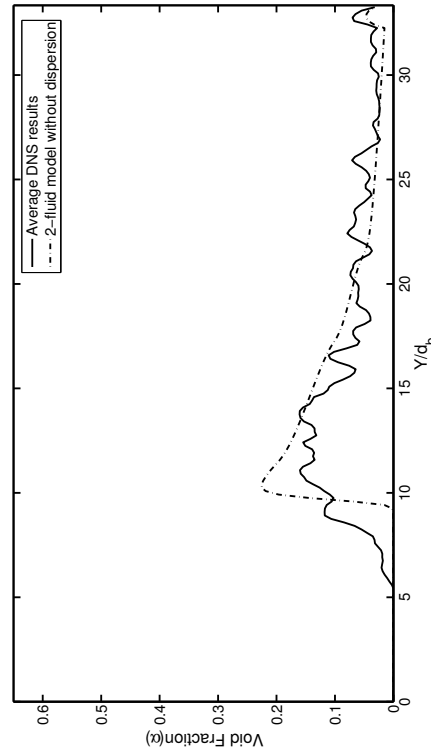
(a) $t/\tau=0.0$



(b) $t/\tau=2.0$



(c) $t/\tau=4.0$



(d) $t/\tau=6.0$

Figure 5.7. The averaged void fraction profile at four different times. The solid line is the simulation results, averaged over five cases. The dashed line is the prediction of the two-fluid model.

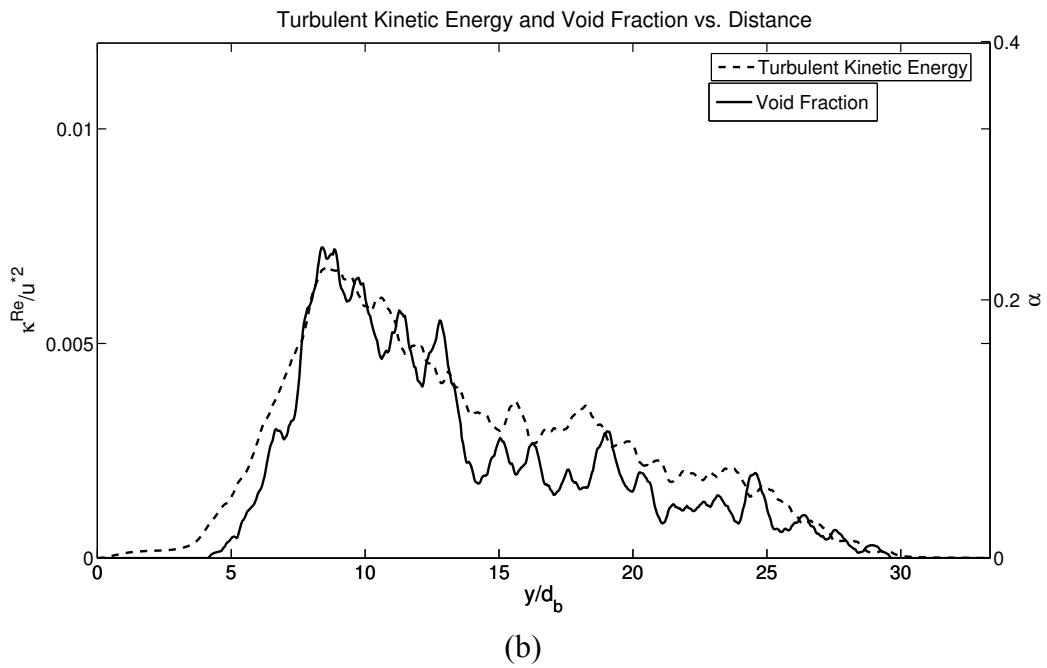
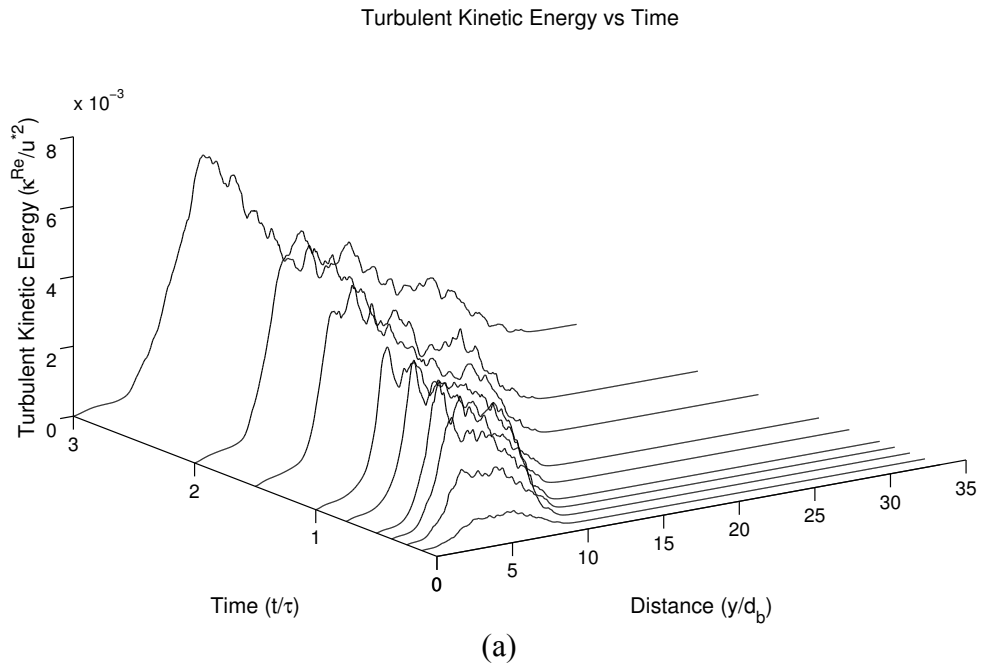


Figure 5.8. (a) The average turbulent kinetic energy profile for one case, shown at seven times. (b) The void fraction and the turbulent kinetic energy versus y at $t/\tau=3.0$.

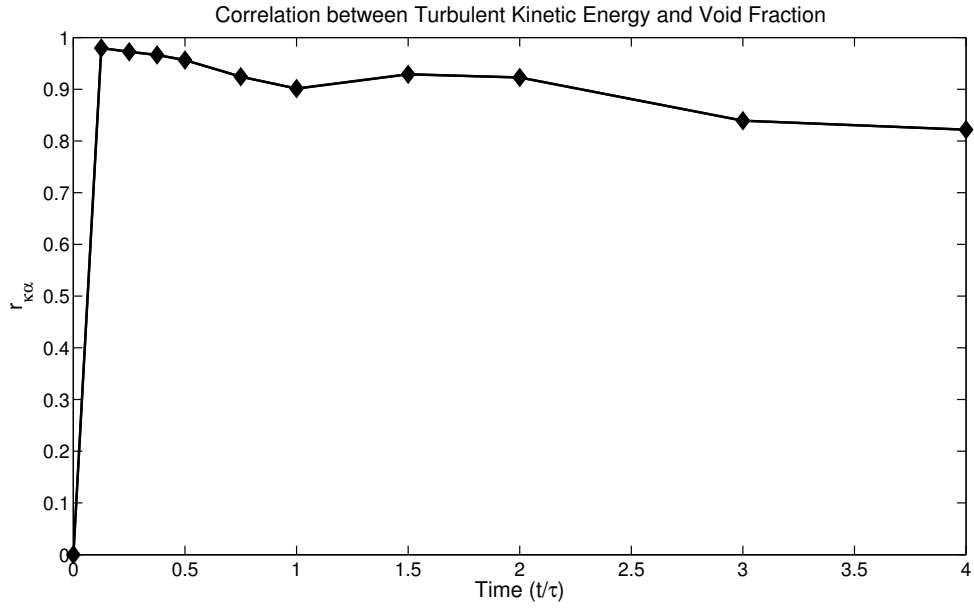


Figure 5.9. The correlation coefficient (as defined in the text) between the turbulent kinetic energy and the void fraction versus time, for one case.

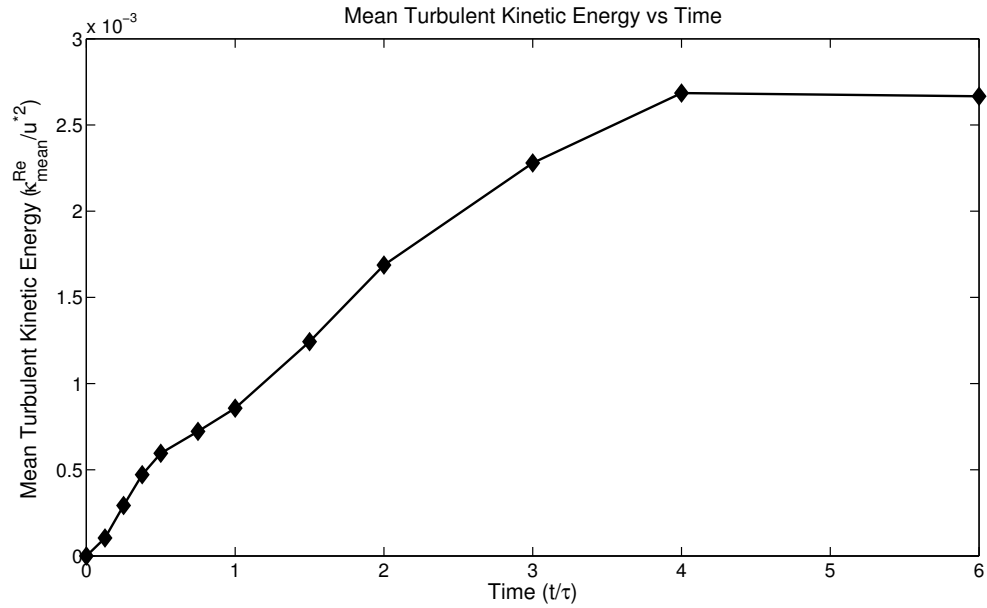
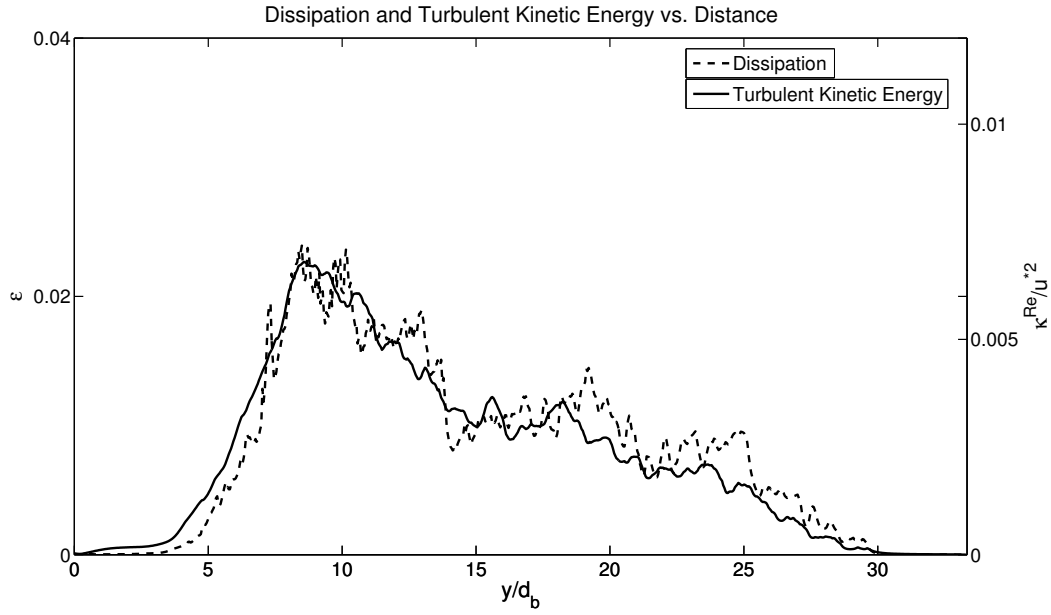
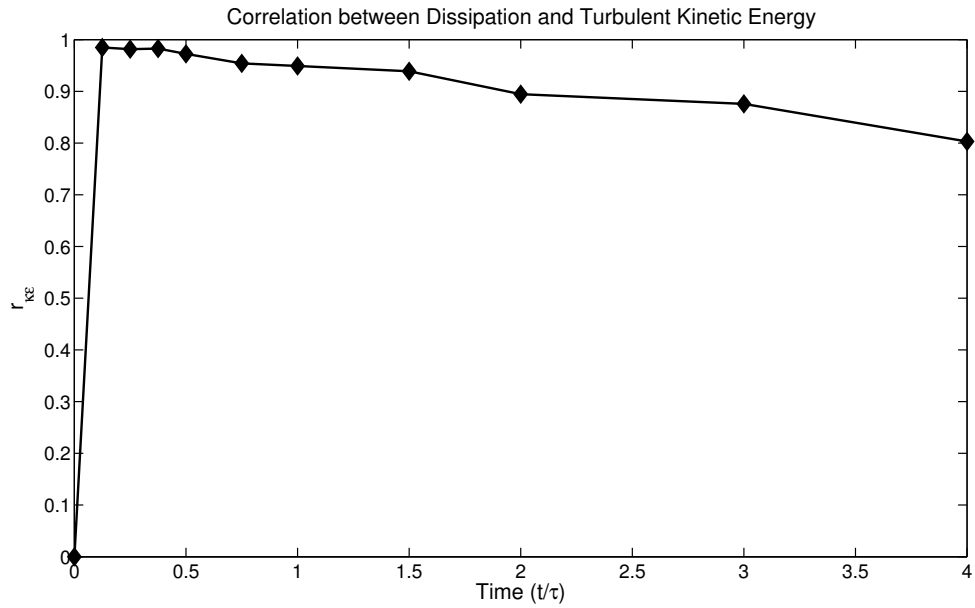


Figure 5.10. The mean turbulent kinetic energy for one case versus time.

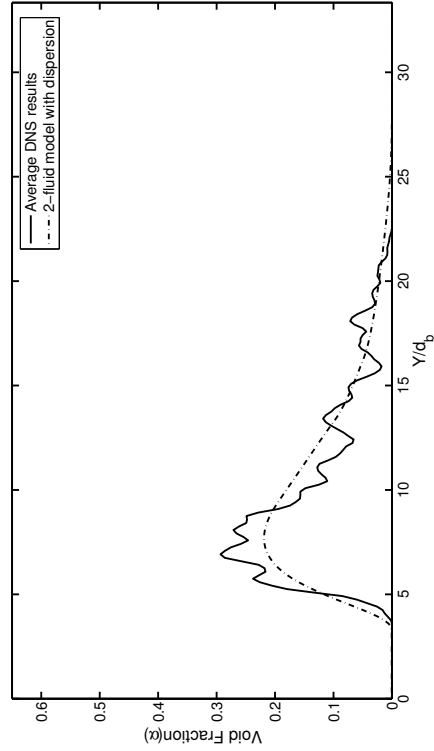


(a)

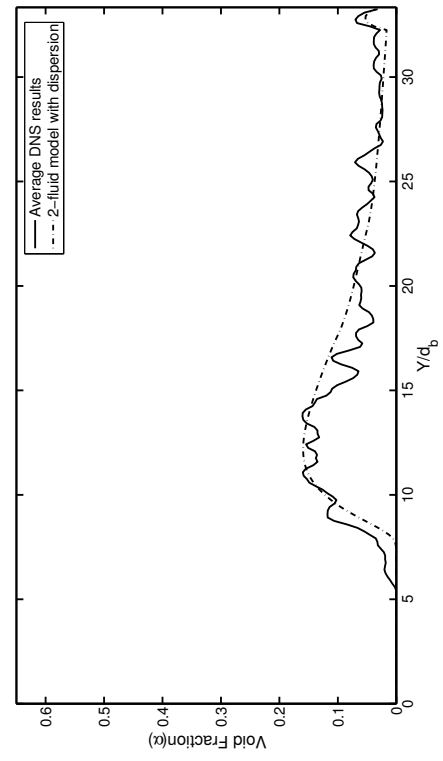


(b)

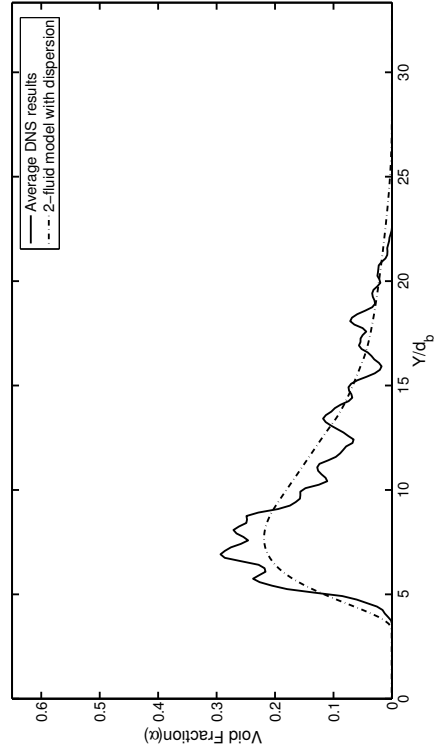
Figure 5.11. (a) The dissipation and the turbulent kinetic energy versus y at $t/\tau=3.0$. (b) The correlation coefficient (as defined in the text) between the dissipation and the turbulent kinetic energy for one case.



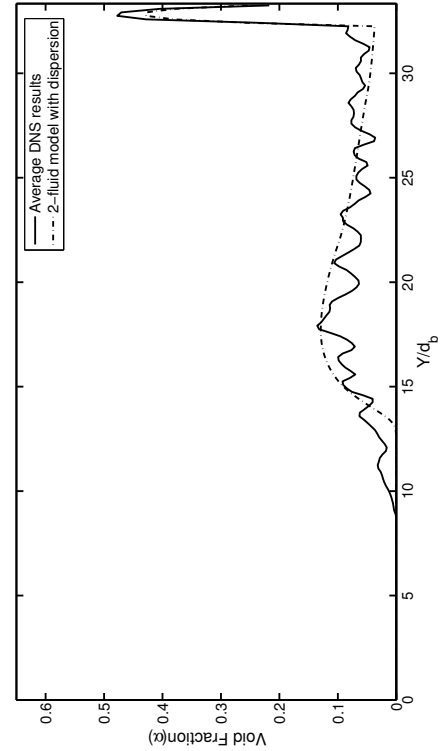
(a) $t/\tau=0.0$



(c) $t/\tau=4.0$



(b) $t/\tau=2.0$



(d) $t/\tau=6.0$

Figure 5.12. The averaged void fraction profile from the simulations and as predicted by the two fluid model at different times. Here $C=2.0$ (see Equation 5.6).

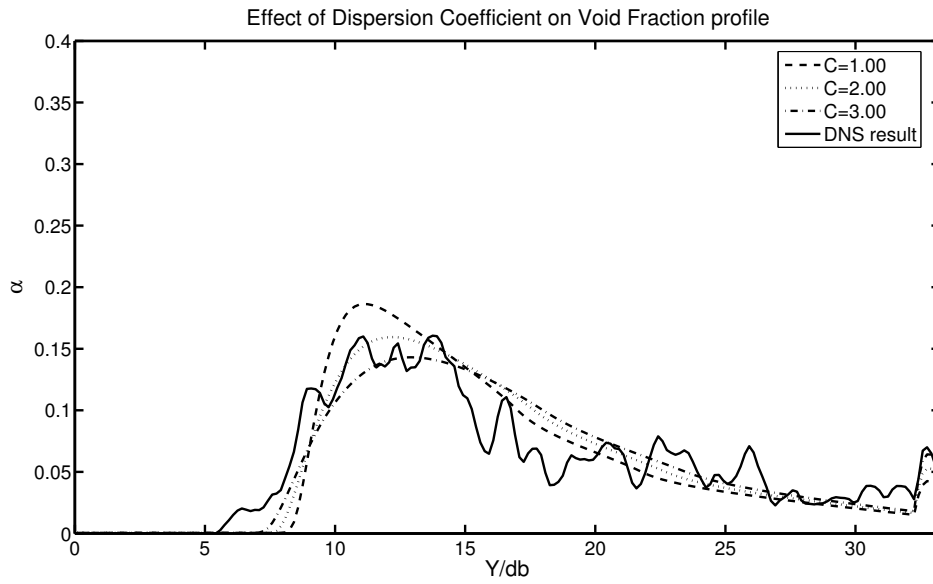


Figure 5.13. The effect of the dispersion coefficient on the predicted void fraction profile at time $t/\tau=4.0$. The average profile from the simulations is also plotted.

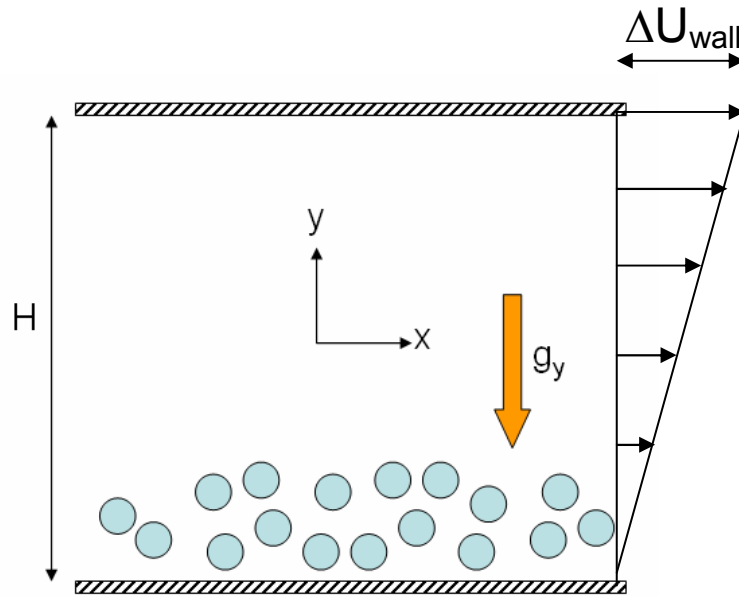
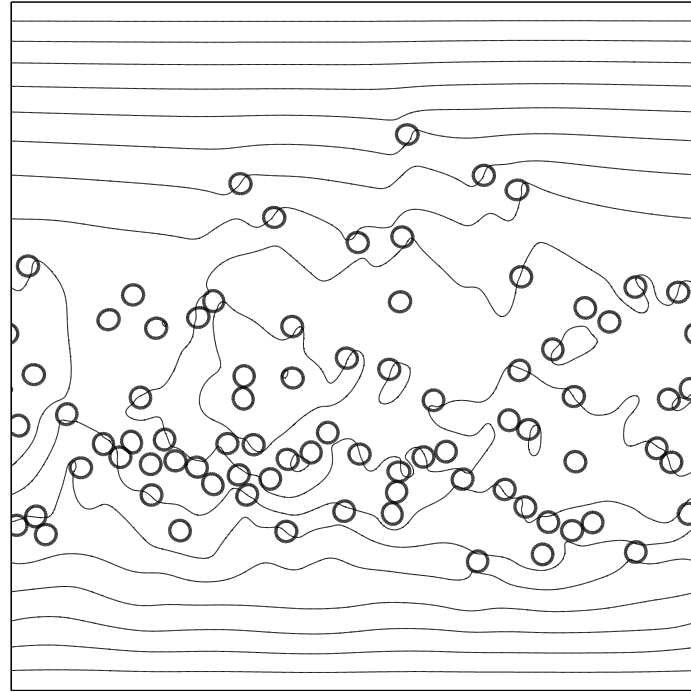


Figure 5.14. The problem setup for the shear flow. The horizontal channel is bounded by walls in the y -direction and is periodic in the x -direction. The height of the channel is H and gravity acts in the negative y direction. The bubbles are released from near the bottom of the channel and rises upwards until they hit the top wall. ΔU_{wall} is the relative velocity between two walls



(a)

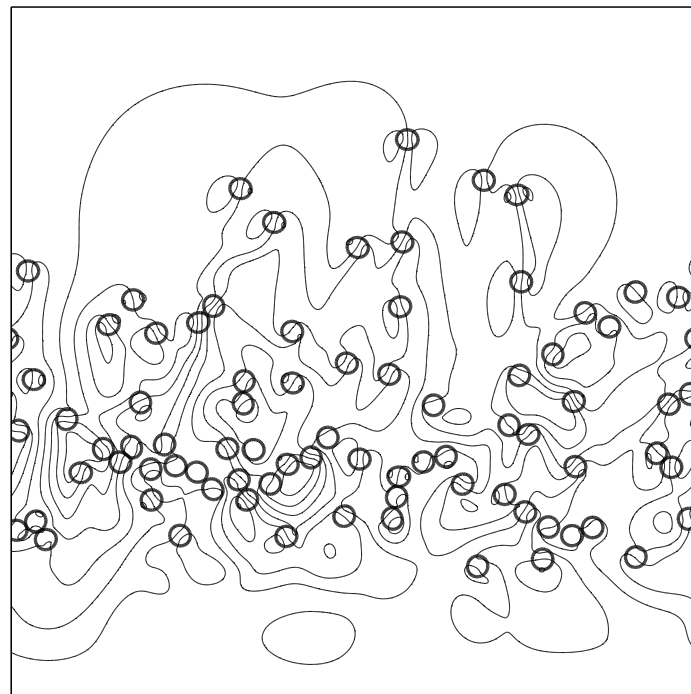
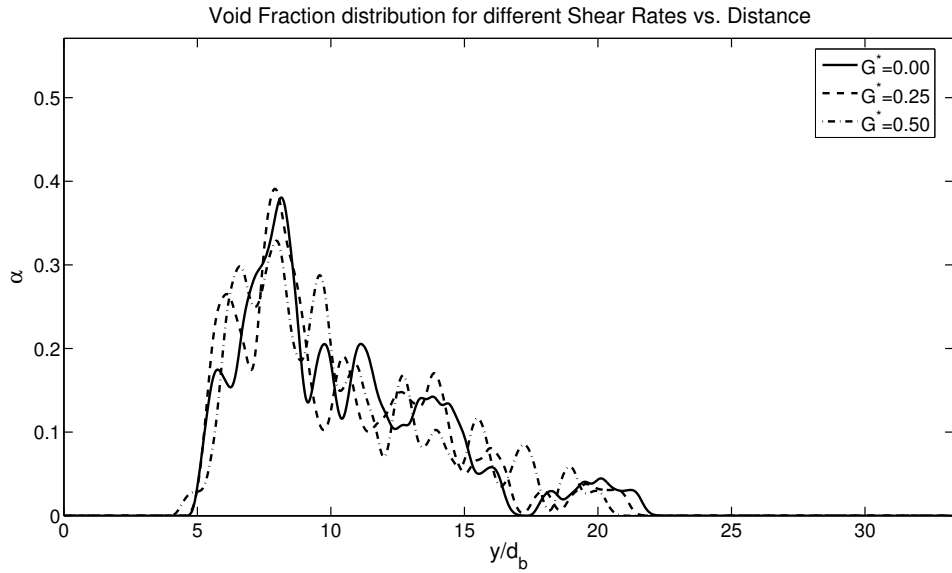
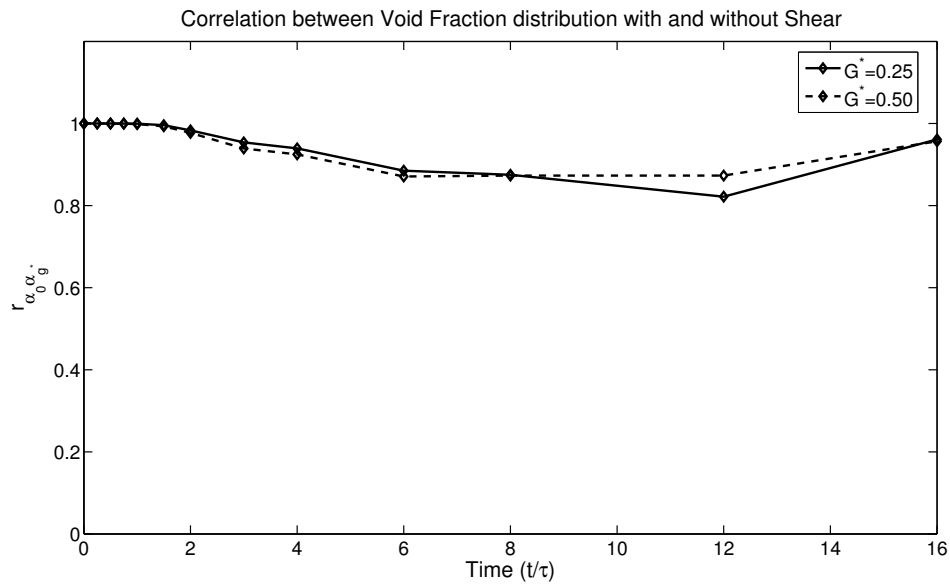


Figure 5.15. Simulations of the rise of bubbles in a horizontal channel. The bubbles and the streamlines in a stationary frame of reference are shown at a single time ($t/\tau=3.0$). (a) Streamlines are computed from total velocity. (b) Streamlines are computed from perturbation velocity.

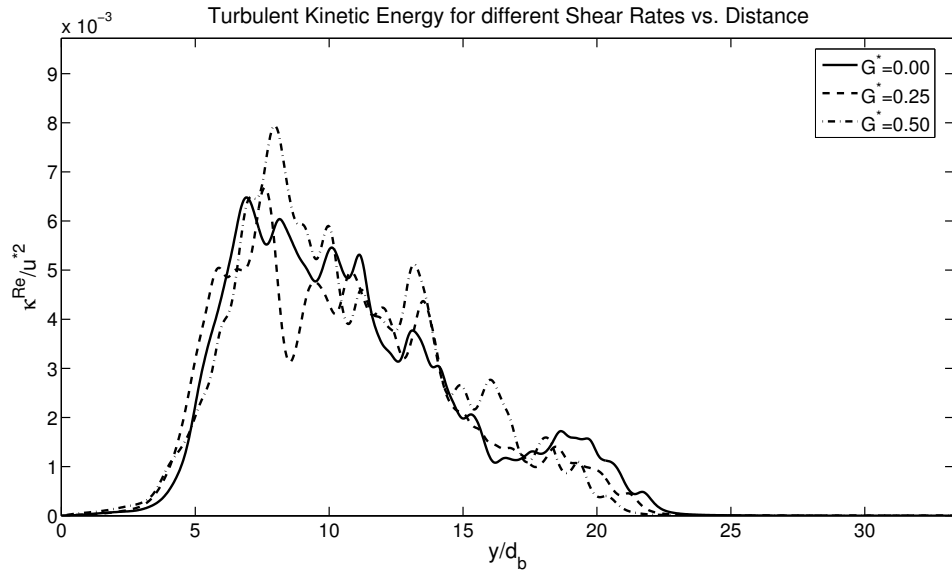


(a)

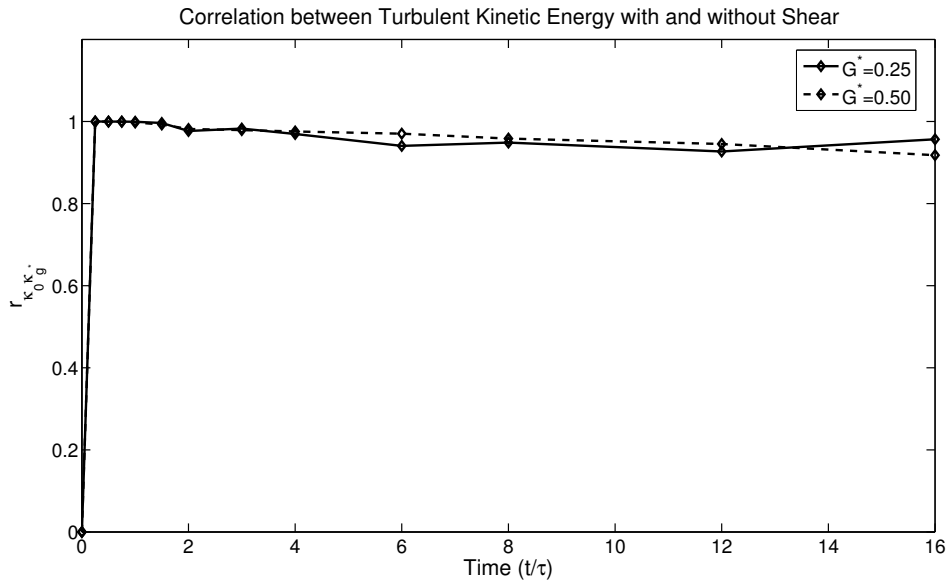


(b)

Figure 5.16. (a) The void fraction distribution for different shear rates versus y at $t/\tau=3.0$. (b) The correlation coefficient (as defined in the text) between the void fraction distributions with no shear and with shear.

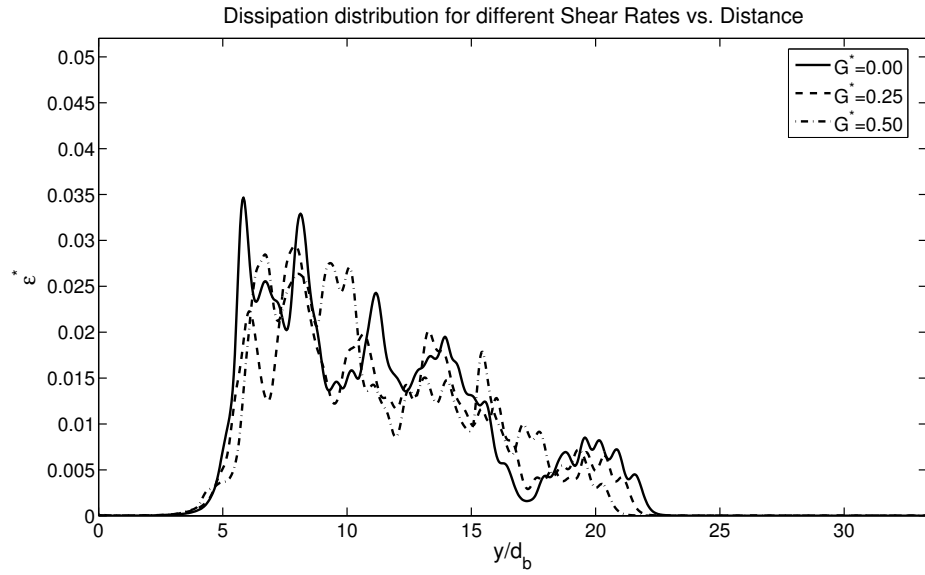


(a)

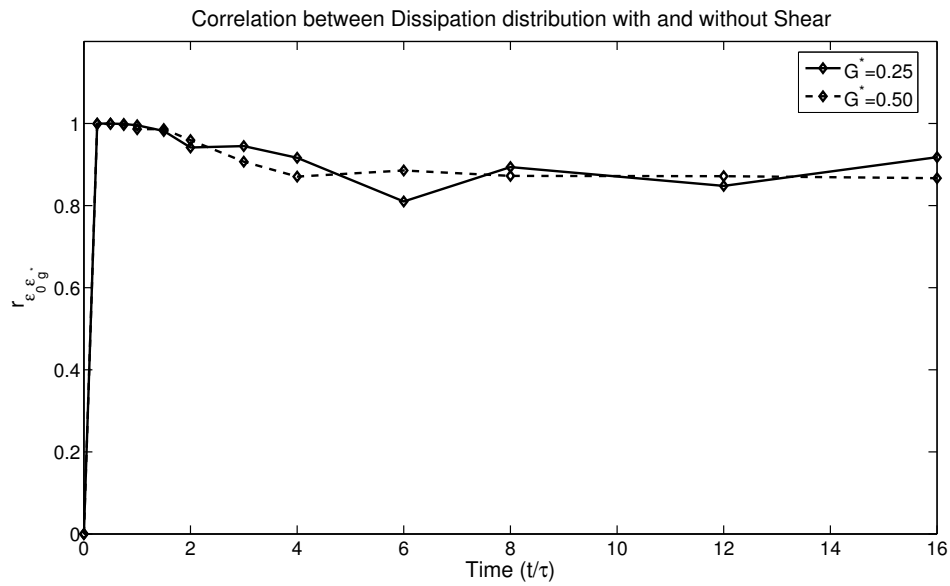


(b)

Figure 5.17. (a) The turbulent kinetic energy distribution for different shear rates versus y at $t/\tau=3.0$. (b) The correlation coefficient (as defined in the text) between the turbulent kinetic energy distributions with no shear and with shear.



(a)



(b)

Figure 5.18. (a) The dissipation distribution for different shear rates versus y at $t/\tau=3.0$. (b) The correlation coefficient (as defined in the text) between the dissipation distributions with no shear and with shear.

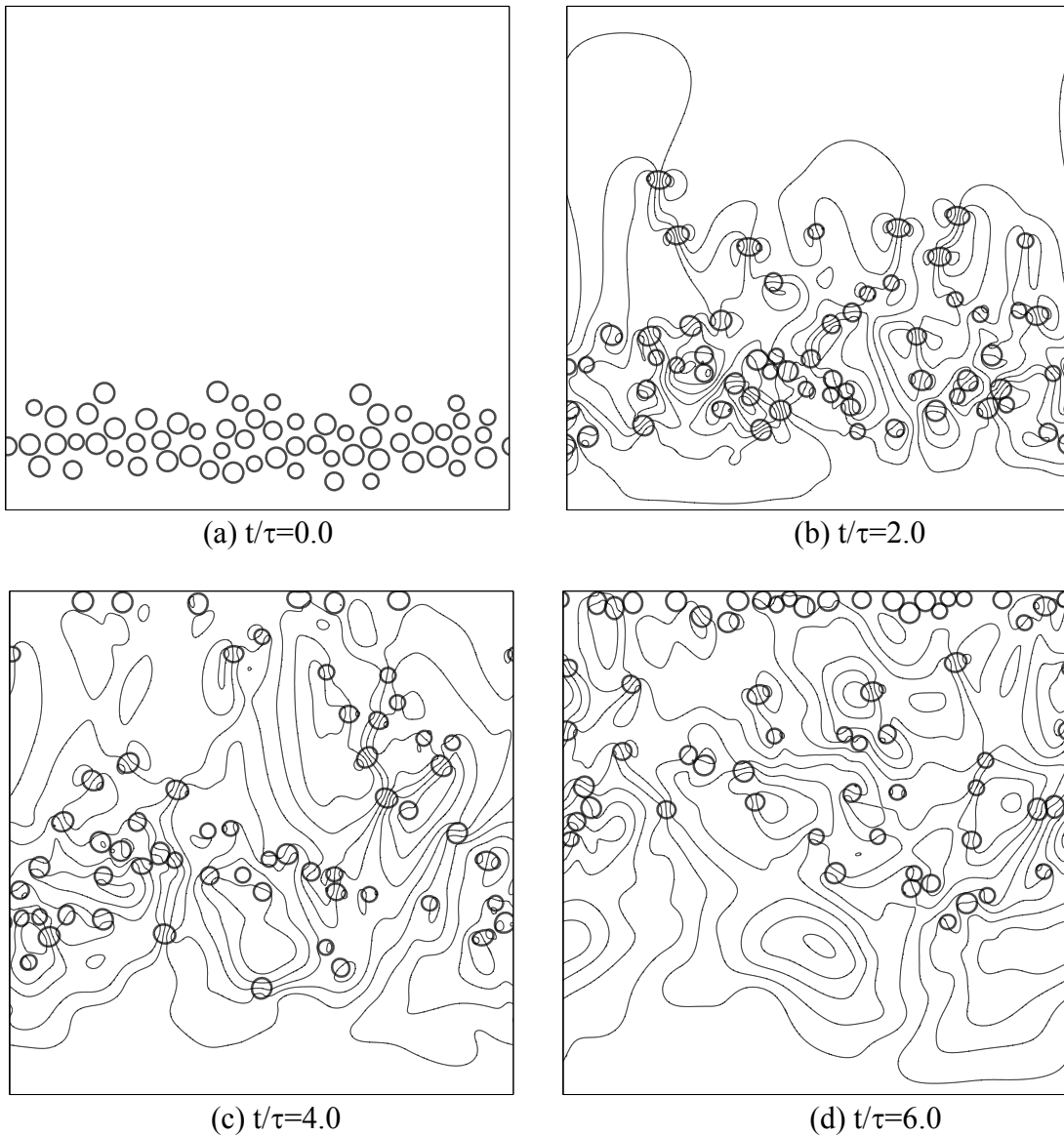


Figure 5.19. Simulations of the rise of poly-dispersed bubbles in a horizontal channel. The bubbles and the streamlines in a stationary frame of reference are shown at four different times, starting with the initial conditions. In the last frame, most of the larger bubbles have hit the top wall.

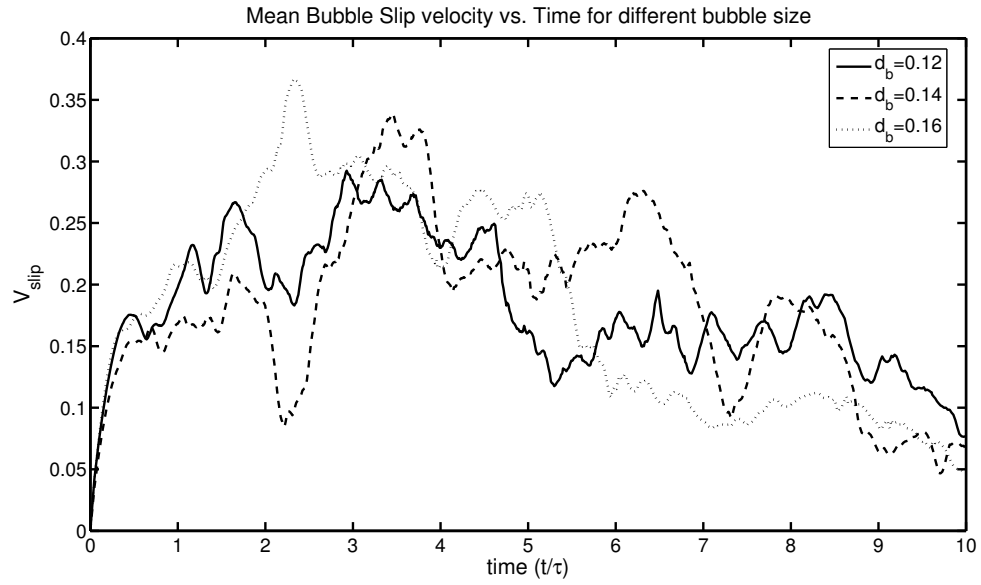


Figure 5.20. The average slip velocity for different bubble sizes with time. The large bubbles ($d=0.16$) rise faster than other bubbles until they start hitting the top wall and slow down.

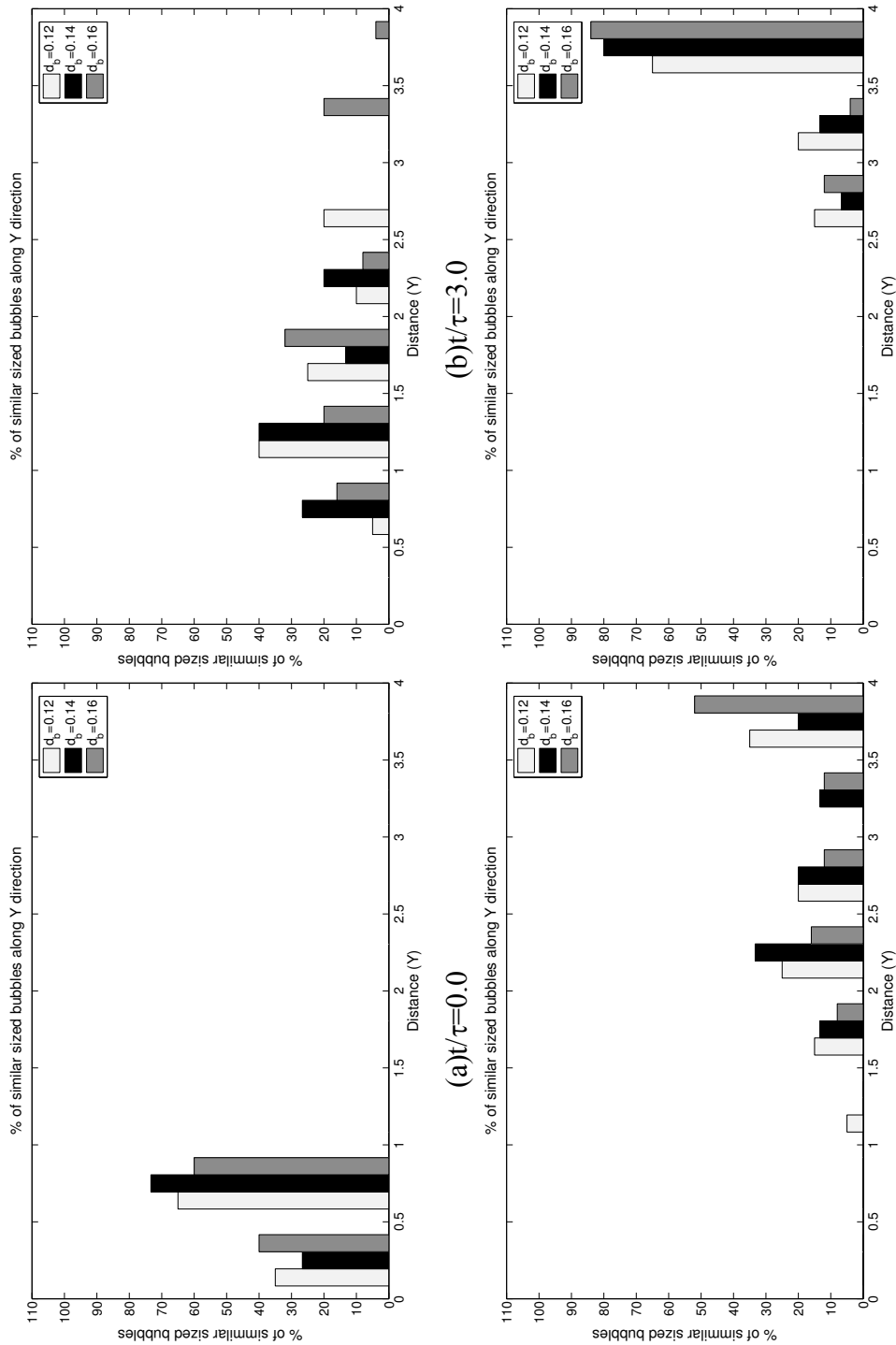


Figure 5.21. % number density of similar sized bubbles are shown at four different times. The data is plotted at 8 equally spaced bins along the vertical direction.

Table 5.2. Parameters for migration poly-disperse bubbles

Domain size	4.0x4.0		
Resolution	768x769		
Density of liquid/bubbles	2.5/0.25		
Viscosity of liquid/bubbles	0.002249365/0.0002249365		
Gravity	1.00		
Surface tension co-efficient	0.128		
Morton Number	4.88x10 ⁻⁶		
Bubble size	LARGE	MEDIUM-SIZE	SMALL
Bubble diameter	0.16	0.14	0.12
Number of bubbles	25	20	15
Eötvös number	0.2813	0.3828	0.5000

Chapter VI

Conclusions

6.1 Conclusions

In the present study several problems related to two-phase bubbly flows in vertical and horizontal channels were studied using direct numerical simulation. Efforts were also made to adapt and apply conventional two-fluid model equations for these special cases. In chapter 3 the motion of non-deformable two-dimensional bubbles in a vertical channel is investigated. A study of the bubble distribution shows that, at steady-state, average mixture density in the middle of the channel is such that it completely balances the applied pressure gradient. The liquid velocity profile is also found to be flat in the middle of the channel. While two-fluid modeling of the setup yielded reasonable results, inadequacy of certain aspects of the model also became clear. Particularly, for the upflow, the flow with bubbles near the wall is extremely sensitive to model coefficients. This suggests that the flow with bubbles near a no-slip wall is very complex and need to be studied in detail. In chapter 4 the flow around a bubble near a vertical fixed wall were examined. It has been found that, under imposed shear, though the bubbles are nearly spherical in the wall layer, they are not completely spherical. It has been observed that this small deformation of the bubbles has a significant effect on the flow field. Surprisingly, this effect increases with increasing surface tension i.e. less deformable the bubbles are, the stronger the effect. This is a significant new result. It has also been found that bubble-bubble interaction is very small in this wall layer and its effects on the average quantities of the flow are virtually non-existent. A parametric study of the flow is

also performed by the carrying out simulations with different non-dimensional parameters. In chapter 5 the transient migration of mono-disperse bubbles in a quiescent horizontal channel is examined. It has been found that the rise velocity of the bubbles is dependent on the local void fraction of the bubbles. A two-fluid model of the flow has been developed which agrees reasonably well with the results from direct numerical simulations. Simulations were also performed to examine the effect of imposed horizontal shear on the flow. Results show that the imposition of a weak horizontal shear does not affect the flow significantly. Simulations of polydisperse bubbles in a quiescent domain show that the rise velocity of the bubbles strongly depends on their size.

The main contribution of the current study has been to address two major questions related to practical multiphase bubbly flows. First of all, considerable progress has been made in gaining new insight about flow-structure of bubbly flows near a no-slip wall. It has been found that surface tension effects are very important in bubbly flows near the wall. This should assist in future efforts of developing an improved bubble-wall interaction model. Another major contribution of this study is to confirm that small scale behavior of homogeneous bubbly flows are universal and is applicable to more complex transient flows. This is an important observation which considerably aids in averaged modeling of complex transient bubbly flows.

6.2 Future Work

In future emphasis will be on two broad areas. Since most of the results for multiple bubbles are two-dimensional in this study, one natural extension of this work is to extend the study in three-dimension. Simulation of larger and more complex systems, including the effects of poly-dispersion and interface contamination and models for coalescence

and breakup also need to be performed in more detail. Practical flows typically include a wide spectrum of bubble sizes. Simulations of polydisperse systems will give insight into the interaction mechanisms of bubbles of different sizes. Another important issue is coalescence and breakup, which to a large extent determine the size distribution of the bubbles. While the numerical method does not allow us to simulate the scales at which coalescence and breakup occur, the results of direct numerical simulations can be used to help formulate sub-grid models for coalescence and breakup. Another direction for future work is the development of more complicated average models. For example, models considered in this study are based on mono-disperse bubbles. Investigations to extend these models for poly-disperse cases, coalescing and breaking bubbles needs to be done in future.

BIBLIOGRAPHY

- Adams, J. 1989 MUDPACK: Multigrid FORTRAN software for the efficient solution of linear elliptic partial differential equations. *Appl. Maths Comput.* 34, 113–146.
- Antal, S. P., Lahey, R. T. Jr. & Flaherty, J. E. 1991 Analysis of Phase Distribution in Fully Developed Laminar Bubbly Two-Phase Flow. *Int'l. J. Multiphase Flow* 17, 635-652.
- Azpitarte, O. E. & Buscaglia, G. C. 2003 Analytical and numerical evaluation of two-fluid model solutions for laminar fully developed bubbly two-phase flows. *Chemical Engineering Science* 58, 3765-3776.
- Biswas, S., Esmaceli, A. & Tryggvason, G. 2005 Comparison of results from DNS of bubbly flows with a two-fluid model for two-dimensional laminar flows. *Int. J. Multiphase Flow* 31, 1036-1048.
- Brücker, C. 1996 3-D scanning-particle-image-velocimetry: Technique and application to a spherical cap wake flow. *Applied Scientific Research* 56, 157–179.
- Bunner, B. & Tryggvason, G. 2002 Dynamics of homogeneous bubbly flows. Part 1: Rise velocity and microstructure of the bubbles. *J. Fluid Mech.* 466, 17-52.
- Bunner, B. & Tryggvason, G. 2002 Dynamics of homogeneous bubbly flows. Part 2: Velocity fluctuations. *J. Fluid Mech.* 466, 53-84.
- Bunner, B. & Tryggvason, G. 2003 Effects of bubble deformation on properties of bubbly flows. *J. Fluid Mech.* 495, 77-118.
- Celik, I., Gel, A. 2002 A new approach in modeling phase distribution in fully developed bubbly pipe flow. *Flow, Turbulence and Combustion* 68, 289-311
- Crowe, C., Sommerfeld, M. & Tsuji, Y. 1998 *Multiphase Flows with Droplets and Particles*. CRC Press
- De Bertodano, M. L., Lahey, R. T. Jr. & Jones, O. C. 1994 Phase distribution in bubbly two-phase flows in vertical ducts *Int. J. Multiphase Flow* 20, 805-818.
- De Bertodano, M. L., Lahey, R. T., Jr. & Jones, O. C. 1987 Phase distribution in bubbly two-phase flows in vertical ducts *Int. J. Multiphase Flow* 13, 327-343
- De Bertodano, M. L., Lahey, R. T., Jr. & Jones, O. C. 1987 Development of a k- ϵ model for bubbly two-phase flow. *J. Fluids Engineering* 13, 327-343

- Drew D. A. & Passman, S. L. 1999 Theory of Multicomponent Fluids. Springer
- Ervin, E.A. & Tryggvason, G. 1997 The rise of bubbles in a vertical shear flow. *J. Fluid Engg.* 119, 443-449.
- Esmaeeli, A. & Tryggvason, G. 1996 An inverse energy cascade in two-dimensional, low Reynolds number bubbly flows. *J. Fluid Mech.* 314, 315-330.
- Esmaeeli, A. & Tryggvason, G. 1998 Direct numerical simulations of bubbly flows. Part I—Low Reynolds number arrays. *J. Fluid Mech.* 377, 313-345.
- Esmaeeli, A., & Tryggvason, G. 1999 Direct Numerical Simulations of bubbly Flows. Part II—Moderate Reynolds Number Arrays. *J. Fluid Mech.* 385, 325-358.
- Esmaeeli, A., & Tryggvason, G. 2005 A direct numerical simulation study of the buoyant rise of bubbles at $O(100)$ Reynolds number. *Phys. Fluids* 17, 93303-1-19.
- Guet, S., Ooms, G. & Oliemans, R. V. A. 2005 Simplified two-fluid model for gas-lift efficiency predictions *AIChE Journal*, 51, 1885-1896
- Hetsroni, G. 1982 Handbook of multiphase systems. McGraw Hill.
- Jan, Y. J. 1994 Computational Studies of Bubble Dynamics. Ph.D. Thesis, The University of Michigan.
- Kashinsky O. N., Randin, V. V. & Timkin, L. S. 1999 Downward bubbly gas-liquid flow in a vertical pipe *Int. J. Multiphase Flow* 25, 109-138
- Kitagawa, A., Sugiyama, K. & Murai, Y. 2004 Experimental detection of bubble–bubble interactions in a wall-sliding bubble swarm. *Int. J. Multiphase Flow* 30, 1213-1234
- Kuo, T. C., Pan, C., Chieng, C. C. & Yang, A. S. 1997 Eulerian-Lagrangian computations on phase distribution of two-phase bubbly flows *Int. J. for Numerical methods in Fluids* 30, 579-593
- Lafaurie, B. , Nardone, C., Scardovelli, R. , Zaleski, S. & Zanetti, G. 1994 Modelling, merging and fragmentation in multiphase flows with SURFER. *J. Comp. Phys.* 113, 134–147.
- Liu, T. J. & Bankoff, S. G. 1993 Structure of air-water bubbly flow in vertical pipe. Part II *Int. J. Heat Mass Transfer* 36, 1049-1060
- Liu, T. J. 1997 Investigation of the wall shear stress in vertical bubbly flow under different bubble size conditions, *Int. J. Multiphase Flow* 23, 1085-1109.
- Lu, J., Biswas, S. & Tryggvason, G. 2006 A DNS study of laminar bubbly flows in a vertical channel. *Int. J. Multiphase Flow* 32, 643-660.

- Luo, R., Pan, X. H. & Yang, X. Y. 2003 Laminar light particle and liquid two-phase flows in a vertical pipe. *Int. J. Multiphase Flow* 29, 603-620
- Matos, A. de, Rosa, E. S. & Franca, F. A. 2004 The phase distribution of upward co-current bubbly flows in a vertical square channel. *J. Braz. Soc. Mech. Sci. & Eng.* 26, 308-316.
- McLaughlin, J. B. 1996 Numerical simulation of bubble motion in water. *J. Colloid Interf. Sci.* 184, 614–625.
- Miyata, H. 1996 Time-marching cfd simulation for moving boundary problems. *21st symposium on naval hydrodynamics*, June 24-28, Trondheim, Norway, pp.1–21.
- Moore, D. W. 1965 The velocity of rise of distorted gas bubbles in a liquid of small viscosity. *J. Fluid Mech.* 23, 749–766.
- Mudde, R. F. & Saito, T. 2005 Hydrodynamical similarities between bubble column and bubbly pipe flow. *J. Fluid Mech.* 437, 203-228.
- Nakoryakov, V. E., Kashinsky, O.N., Randin, V.V. & Timkin, L.S. 1981 Gas liquid bubbly flows in vertical pipes *Int. J. Multiphase Flow* 7, 63-81
- Nakoryakov, V. E., Kashinsky, O.N., Randin, V.V. & Timkin, L. S. 1996 Gas-liquid bubbly flow in vertical pipes, *J. Fluids Eng.* 118, 377-382,
- Oka, H. & Ishii, K. 1999 Numerical analysis on the motion of gas bubbles using level set method. *J. Physical Soc. Japan* 68, 823–832.
- Peskin, C. S. 1977 Numerical analysis of blood flow in the heart. *J. Comput. Phys.*, 25, 220.
- Politano, M. S., Carrica, P. M. & Converti, J. 2003 A model for turbulent polydisperse two-phase flow in vertical channel *Int. J. Multiphase Flow* 29, 1153-1182
- Ryskin, G. & Leal, L. G. 1984 Numerical solution of free-boundary problems in fluid mechanics. Part 2. Buoyancy-driven motion of a gas bubble through a quiescent liquid. *J. Fluid Mech.* 148, 19–35.
- Sangani, A. S. & Didwania, A. K. 1993 Dynamic simulations of flows of bubbly liquids at large Reynolds numbers. *J. Fluid Mech.* 250, 307–337.
- Schlüter, M & Rübiger, N. 1998 Bubble swarm velocity in two-phase flows. HTD-Vol. 361 Proc. of the ASME Heat Transfer Division, vol. 5, ASME 1998.
- Serizawa, A., Kataoka, I. & Michiyoshi, I. 1975 Turbulence structure of air-water bubbly flow. II Local properties, *Int. J. Multiphase Flow* 2, 235—246

- Serizawa, A., Kataoka, I. & Michiyoshi, I. 1975 Turbulence structure of air-water bubbly flow III Transport properties. *Int. J. Multiphase Flow* 2, 247—259
- Smereka, P. 1993 On the motion of bubbles in a periodic box. *J. Fluid Mech.* 254, 79–112.
- So, S., Morikita, H., Takagi, S. & Matsumoto, Y. 2002 Laser Doppler velocimetry measurement of turbulent bubbly channel flow. *Experiments in Fluids* 33 , 135-142.
- Song, Q., Luo, R., Yang, X. Y. & Wang, Z. 2001 Phase distributions for upward laminar dilute bubbly flows with non-uniform bubble sizes in a vertical pipe. *Int. J. Multiphase Flow* 27, 379-390
- Spelt, P. D. M. & Biesheuvel, A. 1997 On the motion of gas bubbles in homogeneous isotropic turbulence. *J. Fluid Mech.* 336, 221–244.
- Stewart, C. W. 1995 Bubble interaction in low-viscosity liquids. *Int. J. Multiphase Flow* 21 (6), 1037–1046.
- Sussman, M. & Smereka, P. 1997 Axisymmetric free boundary problems. *J. Fluid Mech.* 341, 269–294.
- Takagi, S. & Matsumoto, Y. 1994 Three-dimensional deformation of a rising bubble. *Proc. German-Japanese Symp. on Multiphase Flow* KfK 5389, p. 499.
- Tryggvason, G., Bunner, B., Esmaeeli, A., Juric, D., Al-Rawahi, N., Tauber, W., Han, J., Nas, S. & Jan, Y.J. 2001 A Front Tracking Method for the Computations of Multiphase flows. *J. Comput. Physics* 169, 708–759
- Unverdi, S. O. & Tryggvason, G. 1992 A Front Tracking Method for viscous incompressible Flow. *J. Comput. Physics* 169, 708–759.
- Wang S. K., Lee S. J., Jones, O. C. Jr. & Lahey, R.T. 1987 3-D turbulence structure and phase distribution measurements in bubbly two-phase flows. *Int. J. Multiphase Flow* 13, 327-343
- Yurkovetsky, Y. & Brady, J. 1996 Statistical mechanics of bubbly liquids. *Phys. Fluids* 8, 881–895.
- Zhang, D.Z. & Prosperetti, A. 1994 Averaged equations for inviscid disperse two-phase flow. *J. Fluid Mech.* 267, 185-219.